

**2015 SUMMER RESEARCH PROGRAM FOR HIGH SCHOOL JUNIORS**

**AT THE**

**UNIVERSITY OF ROCHESTER'S**

**LABORATORY FOR LASER ENERGETICS**

**STUDENT RESEARCH REPORTS**

**PROGRAM DIRECTOR**

**Dr. R. Stephen Craxton**

**February 2017**

**Lab Report 389**

**2015 SUMMER RESEARCH PROGRAM FOR HIGH SCHOOL JUNIORS**

**AT THE**

**UNIVERSITY OF ROCHESTER'S**

**LABORATORY FOR LASER ENERGETICS**

**STUDENT RESEARCH REPORTS**

**PROGRAM DIRECTOR**

**Dr. R. Stephen Craxton**

**LABORATORY FOR LASER ENERGETICS**

University of Rochester  
250 East River Road  
Rochester, NY 14623-1299

During the summer of 2015, 12 students from Rochester-area high schools participated in the Laboratory for Laser Energetics' Summer High School Research Program. The goal of this program is to excite a group of high school students about careers in the areas of science and technology by exposing them to research in a state-of-the-art environment. Too often, students are exposed to "research" only through classroom laboratories, which have prescribed procedures and predictable results. In LLE's summer program, the students experience many of the trials, tribulations, and rewards of scientific research. By participating in research in a real

environment, the students often become more excited about careers in science and technology. In addition, LLE gains from the contributions of the many highly talented students who are attracted to the program.

The students spent most of their time working on their individual research projects with members of LLE's scientific staff. The projects were related to current research activities at LLE and covered a broad range of areas of interest including laser physics, computational modeling of implosion physics, experimental diagnostics development, liquid crystal chemistry, ultra-intense laser-matter interactions, optical design, tritium capture and storage, and interactive data analysis. The students, their high schools, their LLE supervisors, and their project titles are listed in the table. Their written reports are collected in this volume. By working through several iterations of their project reports, incorporating feedback from their supervisors and the Program Director, the students experience most of the steps involved in preparing a scientific paper for publication.

The students attended weekly seminars on technical topics associated with LLE's research. Topics this year included laser physics, fusion, holography, nonlinear optics, atomic force microscopy, scientific ethics, and attosecond science. The students also received safety training, learned how to give scientific presentations, and were introduced to LLE's resources, especially the computational facilities.

The program culminated on 26 August with the "High School Student Summer Research Symposium," at which the students presented the results of their research to an audience including parents, teachers, and LLE staff. Each student spoke for approximately ten minutes and answered questions. At the symposium LLE presented its 19th annual William D. Ryan Inspirational Teacher Award. The recipient this year was Mr. Rod Engels, a physics teacher at

Victor Senior High School. This award honors a teacher, nominated by alumni of the LLE program, who has inspired outstanding students in the areas of science, mathematics, and technology. Mr. Engels was nominated by William Franceschi and Junhong Sam Zhou, participants in the 2014 Summer Program.

A total of 340 high school students have participated in the program since it began in 1989. The students this year were selected from nearly 70 applicants. Each applicant submitted an essay describing their interests in science and technology, a copy of their transcript, and a letter of recommendation from a science or math teacher.

In the past, several participants of this program have gone on to become semifinalists and finalists in the prestigious, nationwide Intel Science Talent Search. From this year's program, Ishir Seth qualified to attend the Intel Science and Engineering Fair, where he won an award in the Physics and Astronomy category.

LLE plans to continue this program in future years. The program is strictly for students from Rochester-area high schools who have just completed their junior year. Application information is mailed to schools and placed on the LLE website in early February with an application deadline near the middle of March. For more information about the program, please contact Dr. R. Stephen Craxton at LLE.

This program was supported by the U.S. Department of Energy Office of Inertial Confinement Fusion under Cooperative Agreement No. DE-NA0001944.

### High School Students and Projects (Summer 2015)

Name	High School	Supervisor	Project Title
James Bonadonna	Honeoye Falls–Lima	K. L. Marshall	Next Generation Liquid Crystal Mixtures for OMEGA Circular Polarizer/Isolator Devices
Christopher Bosso	Penfield	P. B. Radha	Optimizing Picket-Pulse-Shape Polar-Drive Implosion Designs on the National Ignition Facility
Gabriel Evans	McQuaid	W. T. Shmayda	Measuring the Hydrogen Pressure over Palladium Hydride
Ryan Gao	Brighton	M. Barczys	Modeling Damage Propagation on the OMEGA EP Laser
Phoebe Huang	Webster Schroeder	R. S. Craxton	Analysis of Unabsorbed Light from Exploding-Pusher Targets Used for Proton Backlighting on the National Ignition Facility
Jake Kinney	Pittsford Sutherland	R. S. Craxton	Optimization of Backlighter Targets Using a Saturn Ring on the National Ignition Facility
Nathan Knauf	Harley	R. W. Kidder	A Web-Based Interface for Collaborative Multi-User Data Analysis in a Scientific Research Environment
Peter Mizes	Pittsford Sutherland	T. Z. Kosc	Modeling OMEGA Polarization
Eileen Norris	Brighton	S.-W. Bahk	Design of an Imaging Telescope with Variable Magnification and Imaging Distance
Alexander Proschel	Pittsford Sutherland	W. T. Shmayda	Isotopic Exchange over a Platinized Molecular Sieve
Ishir Seth	Brighton	J. P. Knauer	Analysis of CVD Diamonds for Neutron Detection on OMEGA
Xilin Zhou	Webster Schroeder	S. X. Hu	Radiation Reaction of Electrons at Laser Intensities up to $10^{25}$ W/cm <sup>2</sup>

***Next Generation Liquid Crystal Mixtures for OMEGA Circular  
Polarizer/Isolator Devices***

James Bonadonna

Honeoye Falls-Lima High School

Advisor: Kenneth L. Marshall

University of Rochester

Laboratory for Laser Energetics

Summer High School Research Program 2015

March 2016

## **Abstract**

Liquid crystal (LC) devices have been in use in the OMEGA laser system for over 30 years both to generate circularly polarized light in order to optimize power output and to prevent against back-reflections that could damage the laser system. New LC mixtures for use in OMEGA LC circular polarizers (LCP's) must be developed because one of the components of the current LC formulation (ZLI-1167) is no longer available commercially. A survey of commercially available LC host materials and chiral dopants was conducted, and the most viable candidates were selected and used in the preparation of test mixtures for evaluation of key device properties such as selective reflection peak width, peak wavelength tunability, and laser damage threshold. Of the three LC mixture formulations that were developed and characterized, a mixture containing 11.65% of R811 chiral dopant in the nematic host MLC 6601 showed the best thermodynamic stability over time and possessed optical properties similar to those of the LC mixtures currently in use in OMEGA LCP devices, while also achieving significantly higher laser damage thresholds.

## **1. Introduction**

In the OMEGA laser system, liquid crystal (LC) devices are used to circularly polarize near-IR light at 1054 nm in order to optimize power output as well as isolate one handedness of light, to preventing damage to laser system optics. These devices help to optimize power output when compared to linear polarizers based on the fact that all laser glass fabricated in large apertures will have minor imperfections in optical homogeneity due to stresses produced by the glass fabrication process. Consequently, linearly polarized light passing through this medium will be converted to elliptically polarized light, which results in a loss of energy of up to 30%

[1]. Circularly polarized light passing through the same medium will be unaffected by these imperfections, which allows the laser system to operate at nearly 100% efficiency. [1]

Unpolarized incident light contains two different circularly polarized components [right-handed (RH) and left-handed (LH)]; LC circular polarizers (LCP's) isolate one handedness of light from the other by allowing one handedness of light to pass through the device, while the other handedness is reflected or scattered. For LC materials, this "selective reflection" effect occurs for specific wavelengths that satisfy the equation  $\lambda_{\max} = np$ , where  $\lambda_{\max}$  is the selective reflection peak wavelength,  $n$  is the average refractive index of the mixture and  $p$  is the pitch length, which is dependent on the chiral dopant concentration, its helical twisting power, and the mixture temperature. [1] Liquid crystal polarizers are preferable to solid-state devices made from conventional optical materials such as mica or quartz due to attributes such as broad angular tolerance, better scalability to large apertures, high laser damage resistance, and substantially lower cost. An additional feature of LCP devices is their ability to prevent laser induced damage from circularly polarized light reflecting back into the laser system, as incident light undergoes a change in handedness when reflected back off the target (Fig. 1).

Liquid crystal mixtures suitable for use in LCP devices are formulated by introducing a chiral dopant (a compound that cannot be superimposed on its mirror image due to inherent asymmetry in its molecular structure) into a nematic LC host composed of a compound or mixture of compounds that are rod-like in shape and all point in roughly the same direction, represented by a vector called the director. [1] This chiral dopant imparts its twist sense to the host material, creating a chiral nematic LC mixture with a helical structure (Fig. 2).

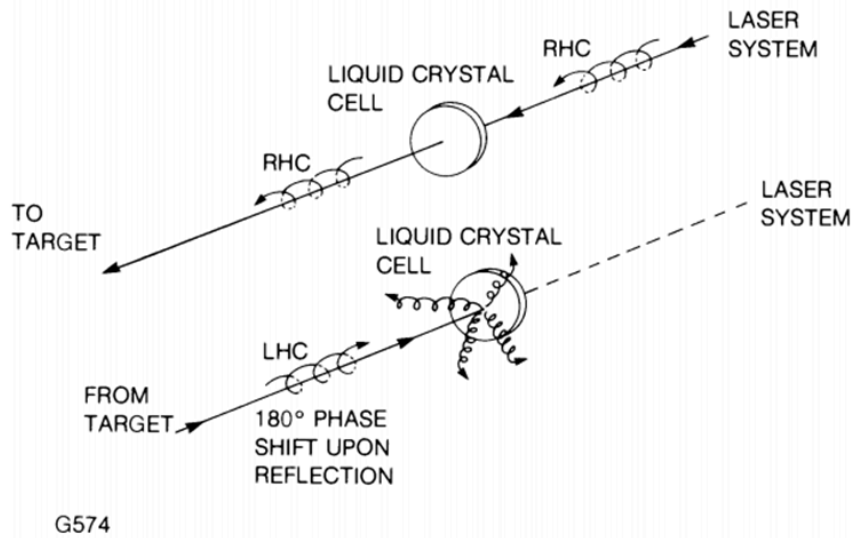


**Fig. 1:** Illustration of the use of LC polarizers to protect the laser system from back-reflected light. RHC and LHC denote the two polarizations of light.

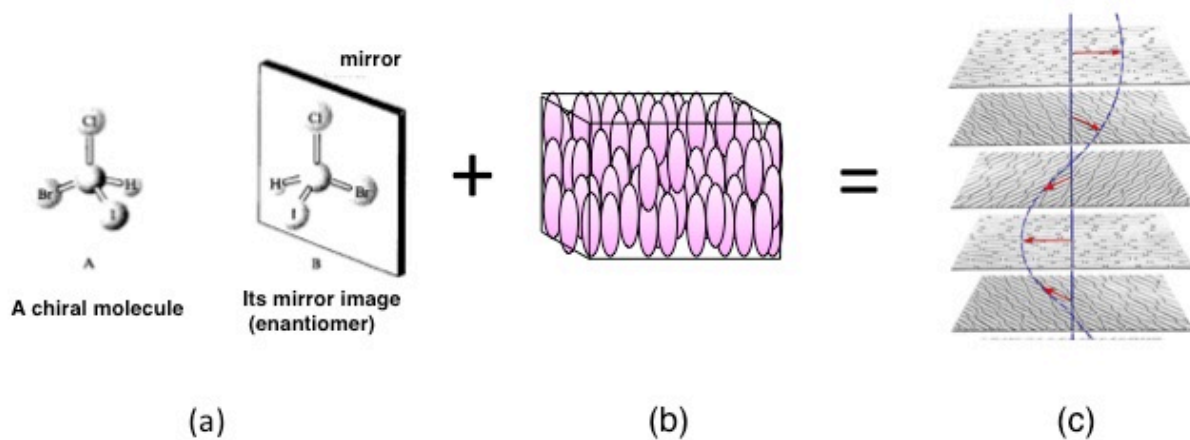


**Fig. 2:** Visual representation of the process of forming a chiral nematic LC mixture. The chiral dopant (a) is added to the nematic host (b) forming the chiral nematic helical structure (c) that has the ability to selectively reflect one handedness of circularly polarized light.

Existing RHLCP's in OMEGA employ a mixture of commercial LC materials from EM Industries, Inc. (19.44% CB15 in ZLI-1167, shown in Fig. 3). [1] Because the ZLI-1167 nematic host is no longer commercially available, a new LC mixture must be developed in order to replace any RHLCP's that have been damaged in the laser system.

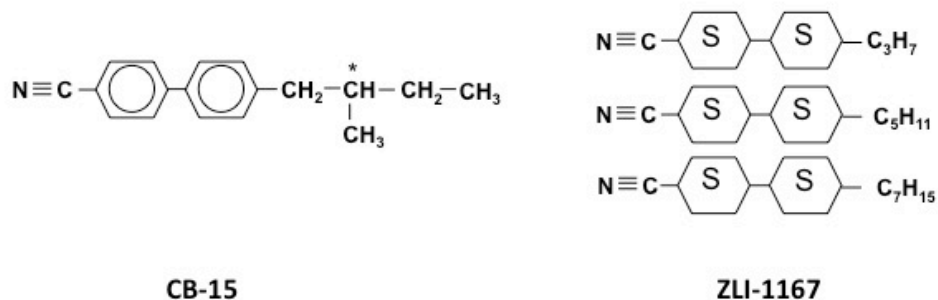


**Fig. 3:** The molecular structures of the chiral dopant (CB-15) and nematic host (ZLI-1167) used in the RHLCP devices currently deployed in OMEGA.

For this study, two commercially available nematic liquid crystal mixtures, MLC 6601 and MLC 2037, were evaluated as replacement hosts for ZLI-1167. These materials were chosen because of earlier work done at LLE that identified them as desirable candidates for LC device applications in high-peak-power UV lasers due to their high 351-nm laser damage thresholds [2]. Although no near-IR laser damage threshold data had been determined on these materials, it was expected that they would perform at least as well (and most likely better) in the near-IR due to their very low optical absorbance across the entire UV, visible, and near-IR regions. Two classes of commercially available chiral dopants were also evaluated; a right-handed cyanobiphenyl material (CB-15) and both right-handed and left-handed versions of a phenyl benzoate ester (R-811 and S-811, respectively), shown in Fig 4 below.

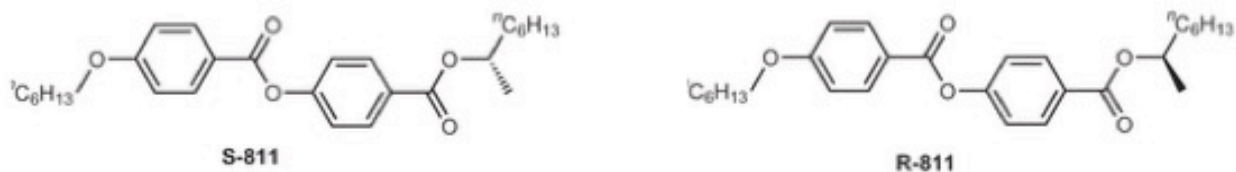


**Fig. 4:** The molecular structures of the phenylbenzoate ester chiral dopants R-811 and S-811.

## **2. Experimental**

### **2.1 LC mixture preparation**

Initial mixture compositions for testing were determined from previous compatibility studies of the chiral dopants CB-15 and S-811 in the nematic hosts MLC 2043 and MLC-6601 [3]. Preliminary experiments were conducted using the left-handed chiral dopant S-811 rather than right-handed R-811 due to the low cost and ready availability of the former and the high cost of the latter. This substitution is reasonable because the two optical isomers are essentially identical in every respect except their helical twist sense. A concentration of ~20% wt/wt of the chiral dopant in each nematic host was used as a starting point for the testing. The LC mixtures were prepared by combining the chiral dopant and nematic host in a clean beaker and heating the mixture on a hotplate with stirring until the LC material reached its isotropic phase and became completely transparent. The mixture was stirred and heated for 60 min in the isotropic phase to ensure it was completely homogeneous.

### **2.2 LC mixture optimization and test device assembly**

Test samples were prepared by placing a small amount of the LC mixture on microscope slides that had been cleaned in a Class 10,000 clean room in the Materials Laboratory using an aqueous cleaning process that consisted of the following steps: (1) scrubbing with 0.05- $\mu\text{m}$  MasterPrep® polishing suspension using a synthetic wiper, followed by rinsing with 2 megohm-cm deionized (DI) water and 18.5 megohm-cm DI water; (2) ultrasonic cleaning at 69°C in a solution of Extran detergent for 1 hr.; and (3) final rinsing with 18.5 megohm-cm DI water, followed by blow-drying with nitrogen to remove any visible moisture. Final drying was accomplished on a hotplate at 130°C for 60 minutes.

The selective reflection peak wavelength ( $\lambda_{\text{max}}$ ) of the test mixtures was determined using a Perkin Elmer Lambda 900 UV-VIS NIR spectrophotometer. The concentration of the chiral dopant was adjusted, new test samples were prepared on microscope slides, and the samples re-tested on the Lambda 900 until the  $\lambda_{\text{max}}$  of the mixture was  $\sim 1060$  nm. Once this  $\lambda_{\text{max}}$  value was achieved, the mixtures were used to construct LCP devices in the clean room area using two 25 mm dia. glass substrates that had been subjected to the same cleaning process as the microscope slides. One cleaned substrate was placed on a hotplate in the Class 100 clean hood housed within the clean room; to control the cell gap, a small amount of LC material was mixed with 14  $\mu\text{m}$  microspheres in the LC isotropic phase and droplets of the mixture were placed at  $120^\circ$  intervals around the edge of the substrate. The second substrate was lowered onto the first substrate and the substrates were offset to produce a small ledge on which to deposit the LC mixture for filling the device. After heating the empty device to  $90^\circ\text{C}$ , a small amount of LC was dispensed onto the ledge using a syringe equipped with a submicron particle filter and the LC fluid was allowed to flow into the cell gap by capillary action. The hot plate was set to cool at a rate of  $10^\circ\text{C}/\text{hr}$ ; once the device had cooled to  $20^\circ\text{C}$ , the substrates were bonded together using three small pieces of glass (“tacks”) positioned around the outside of the device at  $120^\circ$  using an epoxy adhesive. The devices were then ready for determination of the  $\lambda_{\text{max}}$  using the Lambda 900 spectrophotometer.

### **3. Results and Discussion**

Figures 5, 6, and 7 compare selective reflection scans for mixtures of the chiral dopants CB15 in MLC 6601 and MLC 2037 (Figs 5 and 6) and for S-811 in MLC 6601 (Fig 7) as functions of sample aging. The  $\lambda_{\text{max}}$  for both MLC 2037 and MLC 6601 containing 20% wt/wt of

CB15 drifted toward longer wavelengths as the samples aged over 7-9 months, while the  $\lambda_{\text{max}}$  of the mixture containing S-811 in MLC6601 remained essentially unchanged after 5 months.

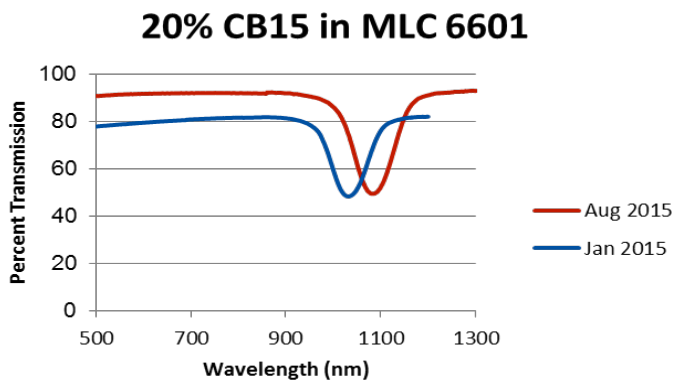


*Fig. 5:* Plot of the transmission of CB15 in MLC 6601 over time. The peak wavelength changed by 52 nm after 7 months.

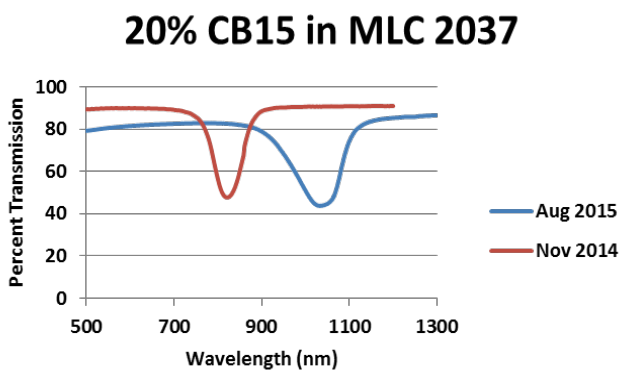


*Fig. 6:* Plot of the transmission of CB15 in MLC 2037. The peak wavelength changed by 212 nm in 9 months.

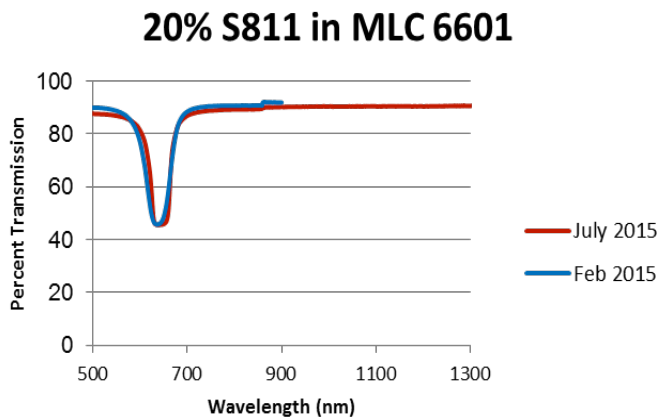


*Fig. 7:* Plot of the transmission of S811 in MLC 6601 over time. The peak wavelength changed by 4 nm in five months.

The cause for the drift in  $\lambda_{\max}$  for the samples containing CB-15 is not well understood, but may possibly be due to micro-phase separation of the chiral component from the host material. No such shift in  $\lambda_{\max}$  is observed with S-811 in MLC 6601; this chiral compound is significantly less polar than CB-15, which might reduce micro-phase separation. Further investigations centered on the S-811/MLC 6601 due to its good long-term stability.

The  $\lambda_{\max}$  for the S-811/MLC 6601 mixture was fine-tuned to the operating wavelength of OMEGA by preparing a series of >15 mixtures with varying concentrations of S-811 in MLC 6601 and constructing a plot of  $\lambda_{\max}$  vs dopant concentration using selective reflection data obtained from these mixtures (Fig. 8). [4]

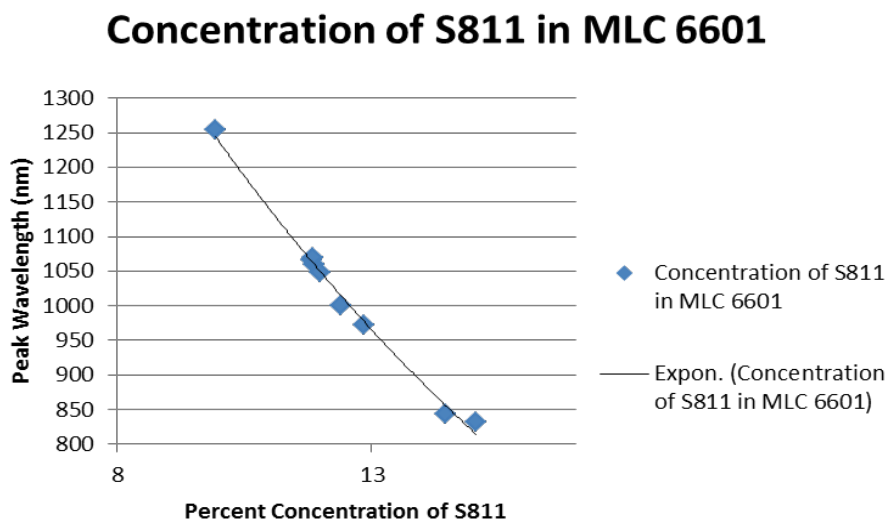


**Fig 8:** Scatter plot of the transmission peak of S811 in MLC 6601 vs. concentration. The data illustrates the wavelength tunability of the mixture. The line is an exponential fit to the data.

Because the chemical structure and physical properties of S-811 and R-811 are essentially identical except for their twist sense, the curve in Fig. 8 for S-811 in MLC 6601 was used to determine the required concentration of R811 in the same host to generate a  $\lambda_{\max}$  at 1060 nm. Preparation of the R811/MLC 6601 mixture at this chiral component concentration revealed

that the helical twisting power (HTP) of R811 in MLC 6601 was slightly greater than its left-handed analog, which required a slight reduction in R811 concentration to obtain the correct  $\lambda_{\max}$ . Figure 9 shows selective reflection curves for concentrations of R811 in MLC 6601 ranging from 11.65% to 11.85%.; the 11.65% concentration displayed a  $\lambda_{\max}$  of 1065 nm. Test LCP devices prepared with this composition showed values of  $\lambda_{\max}$  that were consistently 5-7 nm lower than those obtained for the same material measured between microscope slides, which necessitated additional fine tuning of mixture composition.

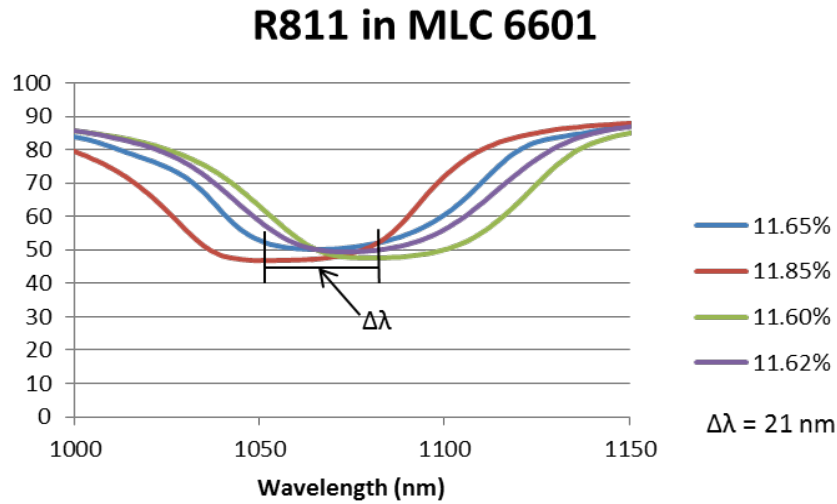


**Fig. 9:** Plot of the transmission of various concentrations of R811 in MLC 6601. An R811 concentration of 11.65% displayed a  $\lambda_{\max}$  of 1065 nm, and was used to prepare test RHLCP devices.

The optical properties of the R811/MLC6601 mixture were examined by both polarizing optical microscopy and reflectance spectroscopy to compare them to those of the CB15/ZLI 1167 mixture currently used in OMEGA RHLCP devices. Both materials showed nearly identical LC textures when viewed under crossed polarizers at 100x magnification using a Leitz Orthoplan Pol polarizing microscope in transmission. Reflectance data was also collected for the R811/MLC6601 device using the Lambda 900 spectrophotometer equipped with an integrating

sphere capable of measuring total, diffuse, and specular reflection components. Un-polarized incident light was used for these measurements. The reflectance data showed that the majority of light reflected from the device is diffuse and not specular, indicating that most of the opposite handedness of the light scatters when it hits the LC mixture. Figure 10 shows selective reflection spectra for the R811/MLC6601 device compared to that for an RHLCP device from OMEGA (CPR 4-1-65); the difference in  $\lambda_{\max}$  between the two mixtures is only  $\sim 1$  nm, and the difference in peak widths is within 5 nm.

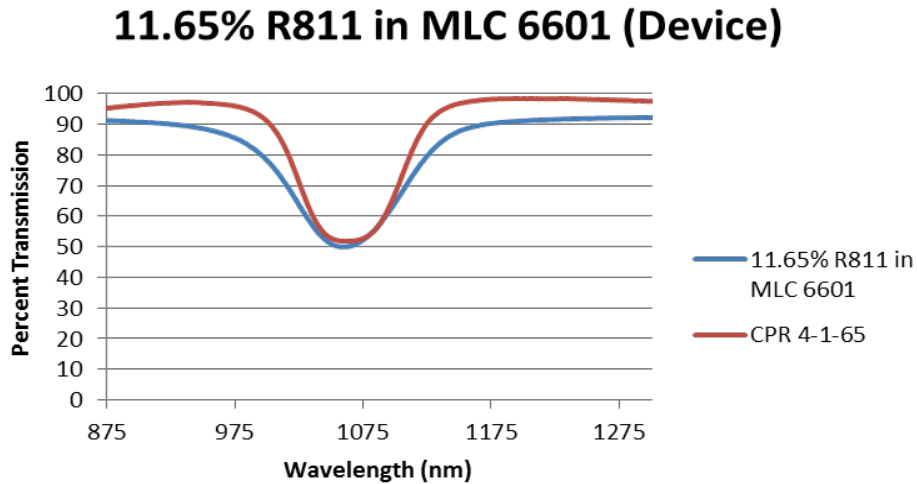


**Fig. 10:** Selective reflection spectra for 11.65% R811 in MLC 6601 and an OMEGA RHLCP device (CPR 4-1-65) containing 19.44% CB15 in ZLI-1167. The higher transmission of CPR 4-1-65 is due to both anti-reflection (AR) coatings on the external substrate surfaces and Nylon alignment coatings on the inner cell surfaces, neither of which are present in the R811/MLC6601 device.

Devices for laser damage testing were prepared in the same manner as described in Section 2.2, but instead using 60-mm-dia, 10-mm-thick fused silica damage test optics (DTO) substrates specifically intended for preparation of damage test samples. Damage testing was conducted at 1054 nm in the chiral nematic LC phase using both 1-on-1 and N-on-1 testing protocols with a 1.4 ns pulse width. In 1-on-1 testing, different sites are irradiated with a single shot, with the laser fluence increased by 15% at each location until damage is observed. In the N-

on-1 testing mode, only a single site is irradiated with increasing fluence until damage is observed. Table 1 lists the damage threshold data collected on the R811/MLC 6601 mixture at 1053 nm, along with previously obtained laser damage data on the CB15/ZLI-1167 mixture currently used in OMEGA RHLCP devices. The very high laser damage thresholds for the new R811/MLC6601 mixture represent a significant improvement over the existing formulation.

Mixture composition	Contrast ratio	$\Delta n$ (589.6 nm)	Laser damage threshold 1053 nm, (J/cm <sup>2</sup> )
19.44% CB-15 in ZLI 1167	> 200:1	0.06	~ 9.5 (N-on-1) <sup>1</sup> 1 ns
11.65% R811 in MLC 6601	TBD	TBD	37.75 ± 1.27 (1-on-1) <sup>2</sup> 42.35 ± 8.60 (N-on-1) <sup>2</sup> 1.4 ns
1. Bulk measurement in 100 $\mu\text{m}$ cell above C-I transition temperature 2. Measured in 14 $\mu\text{m}$ path length LCP device fabricated using fused silica DTO optics assembled in Materials Lab clean room			

**Table 1:** Laser damage threshold data for the new R811/MLC6601 mixture at 1053 nm. Similar data on the RHLCP mixture currently used in OMEGA RHLCP devices is included for reference. Some optical properties for the new mixture have yet to be determined.

#### 4. Conclusions

After testing several possible replacements for the current LC mixture used in the RHLCP devices in the OMEGA laser system, a mixture of 11.65% R811 in MLC 6601 was determined to be the most viable of the over 15 different mixtures that were tested. This mixture shows good thermodynamic stability, optical properties similar to the current mixture, and a significantly improved laser damage threshold (37-42 J/cm<sup>2</sup> at 1053 nm, 1.4 ns). The new materials combination also exhibits ease in selective reflection wavelength tunability and a reflection peak width essentially equivalent to the current mixture used in RHLCP devices. Further work that will be required before this material can be fully qualified for use in OMEGA includes a full characterization of all optical properties (e.g. contrast ratio transmission, scatter)

in a full-aperture (100-200 mm) RHLCP device with nylon alignment coatings and deployment of this device for full-aperture testing on OMEGA.

## **5. Acknowledgements**

I thank Dr. Stephen Craxton and the University of Rochester LLE Summer Research Program for the amazing opportunity to conduct this research. I thank my advisor, Mr. Kenneth Marshall, as well as Debra Saulnier and Katherine James for their help and guidance. I also thank Dr. Semyon Papernov of the LLE Damage Test Facility for obtaining the laser threshold data for my LC mixture. Additionally, I thank all of the Materials Lab staff and students, especially Joann Starowitz and Brendan Coli, for their help in teaching me how to use the equipment and run my experiments.

## **6. References**

- [1] K. L. Marshall, private communication.
- [2] D. Saulnier, B. Taylor, K. L. Marshall, T. J. Kessler, and S. D. Jacobs, “Liquid Crystal Chiroptical Polarization Rotators for the Near-UV Region: Theory, Materials, and Device Applications,” in *Liquid Crystals XVII*, edited by I. C. Khoo (SPIE, Bellingham, WA, 2013), Vol. 8828, Paper 882807.
- [3] K. Smith, Optical Materials Laboratory, Undergraduate interim research report, Jan 15, 2016.
- [4] T. Z. Kosc, A. Owens, A. L. Rigatti, S. D. Jacobs, and J. H. Kelly “Long-Term Performance of Liquid Crystal Optics on Large Fusion Lasers,” presented at CLEO 2013, San Jose, CA, 9–14 June 2013.

*Optimizing Picket-Pulse-Shape Polar-Drive Implosion Designs*

*on the National Ignition Facility*

**Christopher Bosso**

Penfield High School

Advisor: Radha Bahukutumbi

**Laboratory for Laser Energetics**

University of Rochester

Rochester, New York

December 2015

## **Abstract**

In polar drive, laser beams configured for indirect drive on the National Ignition Facility (NIF) are displaced toward the target equator to achieve a more uniform direct-drive implosion. A NIF target consisting of multiple layers including CH (plastic), beryllium, and silicon-doped CH has been optimized for symmetry when irradiated with a triple-picket laser pulse shape. This pulse shape includes three pickets followed by a step and main pulse. The advantage of using a picket pulse shape over just a step and main pulse is the reduction of Rayleigh-Taylor instability, which contributes to the overall stability of the implosion. A combination of beam displacements and picket energy adjustments was used to create uniform shocks during each of the three pickets. The powers in the step and the main pulse were then adjusted, resulting in a significant increase in implosion uniformity. The laser beam profiles used in this design correspond to the so-called intermediate phase plates for direct drive on the NIF which were designed for CH capsules irradiated with two pickets. The optimization of this triple-picket pulse design with a multi-layer target suggests that the intermediate phase plates are sufficiently versatile to permit nearly uniform implosions with various ablaters and laser pulse shapes.

## **I. Introduction**

In direct-drive inertial confinement fusion (ICF) [1] laser beams directly irradiate a capsule consisting of a thin plastic shell with a solid cryogenic layer of deuterium-tritium. The outer region of the target then ablates, or expands, outwards while the center of the

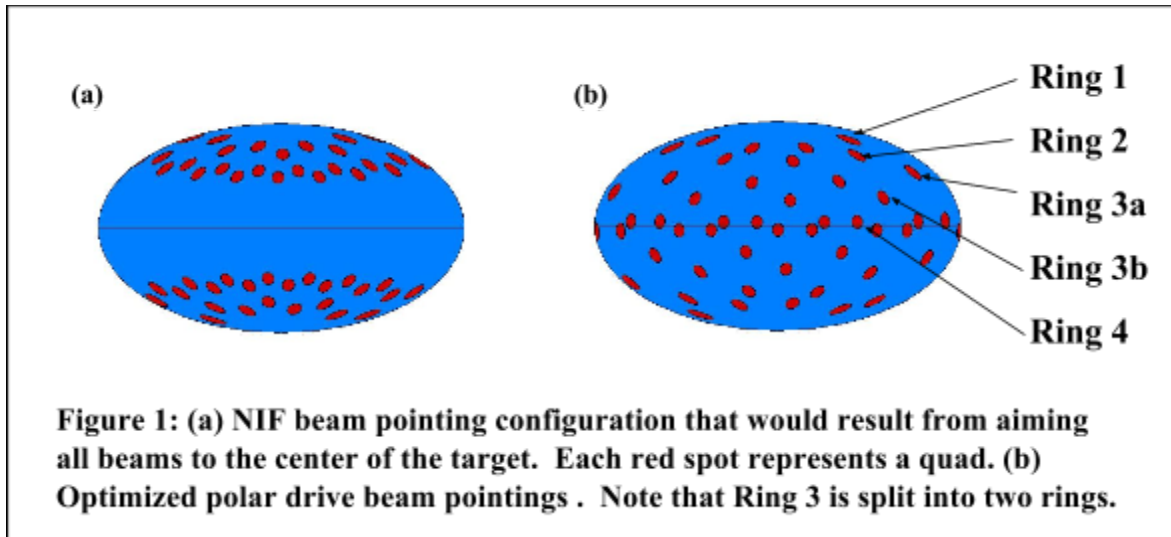
target is driven inwards in a rocket-like implosion resulting in high fuel temperatures and densities. Under these conditions, the deuterium and tritium nuclei fuse creating energetic neutrons and alpha particles. The neutrons escape the imploded capsule and can, in principle, be used to generate electricity by heating water. The alpha particles lose energy through collisions in the fuel and raise the temperature. This results in additional fusion reactions. Ignition is said to occur when more energy is released from the fusion reactions than the laser energy on-target .

Currently, there are two main techniques for irradiating the capsule. The first is direct drive (described above), where laser beams directly illuminate the target. The OMEGA Laser [2] at the University of Rochester is configured for direct drive with 60 nominally identical laser beams arranged symmetrically around the target and aimed at the center of the target. This results in a near-normal angle of incidence to the surface of the target of most of the laser energy. The second is indirect drive [3] where a target is placed inside a cylindrical container made of gold, known as a hohlraum. The hohlraum has laser entrance holes centered on the cylindrical axis through which the beams enter the hohlraum. X rays, emitted by the irradiation of the hohlraum, illuminate the target, thereby driving the implosion. The National Ignition Facility (NIF) [4] is configured for indirect drive with the beam ports at angles from  $23^\circ$  to  $50^\circ$  from the vertical axis.

While the OMEGA laser is useful in studying the physics of ICF, its maximum energy (30 kJ) is insufficient to achieve ignition. The NIF laser, with energy  $\sim 1.5$  MJ, was designed for ignition. However, the beam configuration on the NIF was designed

for indirect drive, which presents a significant challenge for direct drive. If the NIF beam configuration were used for direct drive with all beams aimed at the center of the target, it would result in an implosion whose uniformity was significantly compromised because the poles of the target would receive much more energy per unit area than the equator. A high degree of uniformity is essential for achieving the extreme levels of compression and temperature that are necessary to initiate ignition.

Improved uniformity can be obtained with polar drive [5], where beams are displaced from their original positions on the target surface. On the NIF, there are 192 beams which are grouped into 2x2 arrays called quads. These quads are arranged into four distinct rings in each hemisphere. If the beams are pointed at the center of the target, they strike the target with the pattern shown in Fig. 1a. In polar drive, these rings are displaced toward the equator or “repointed” to achieve better uniformity on the target. Ring 3 is also split into two separate rings, 3a and 3b, to further increase the uniformity of energy distribution over the surface of the target (Fig. 1b). Because the



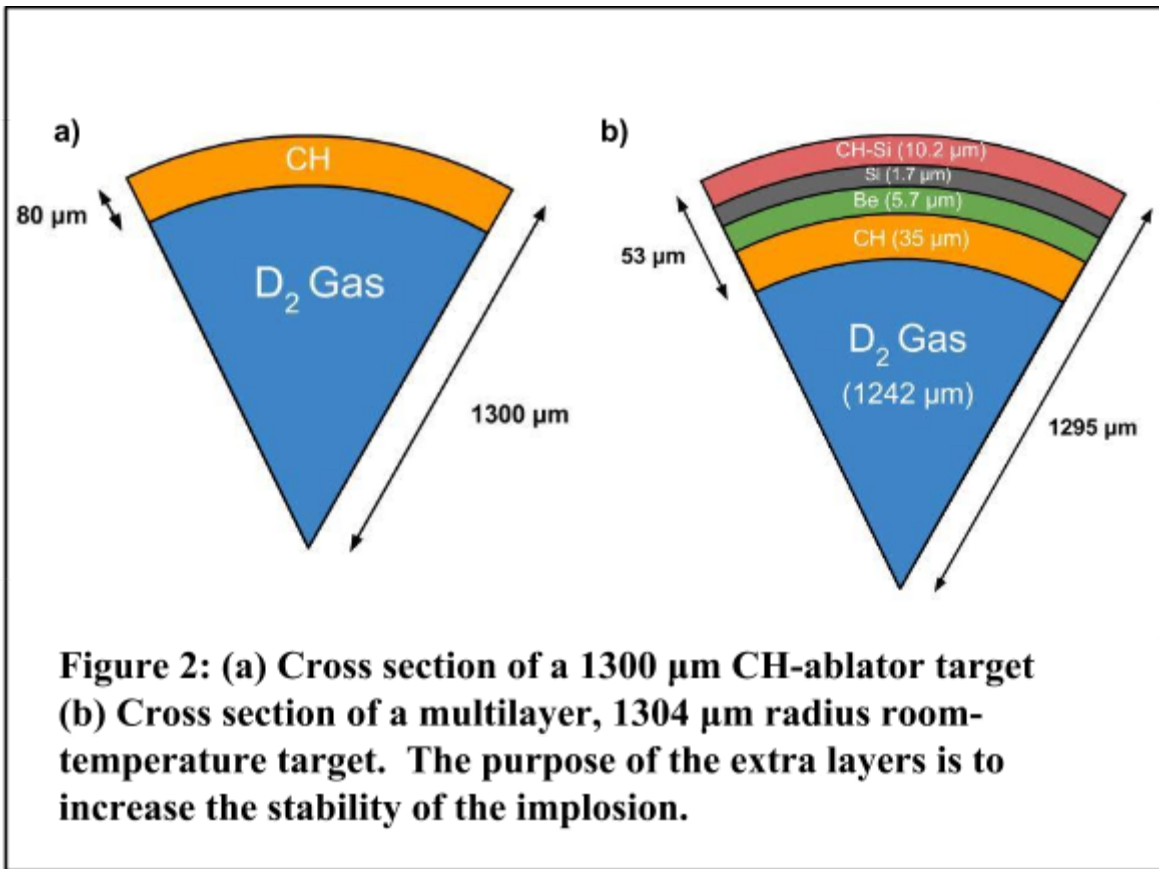
beams are shifted from their original normal angle of incidence, the repointed beams strike the surface of the target at more oblique angles of incidence. This results in the laser energy being deposited over a wider area of the target surface at more oblique angles, which equates to a reduction in drive.

Although the use of polar drive significantly improves the uniformity of the on-target beam arrangement, it also introduces various complications such as the need for different beam energies in each ring to compensate for the increasingly oblique angles of incidence as the beams are displaced further from their original positions. Additional improvements to the irradiation uniformity can be made through the optimization of the laser pulse shapes, beam energies, and the spatial cross-section of each laser beam (beam profiles).

In this paper, the optimization of a multi-layer room-temperature capsule is described. The beam profiles, the capsule parameters, and the total laser power as a function of time are given and the beam pointings and relative laser powers are adjusted to provide maximum uniformity. Beam profiles determine the intensity of the beam and are characterized by a high intensity center and then decreasing intensity towards the edges of the beam. These profiles are engineered using expensive optics known as phase plates. It is therefore important to ensure that the phase plates can be used to drive a variety of designs with a high degree of uniformity. The primary goal is to identify if the previously determined beam profiles for a plastic-only capsule [6] can be used to drive a multi-layer target near-spherically.

## II. Target Design

The target considered in this paper (shown in Fig. 2b) is a spherical capsule with an outer radius of approximately 1295  $\mu\text{m}$  and includes a 53  $\mu\text{m}$  thick shell with multiple layers encasing compressed deuterium gas. The capsule contains layers of plastic (CH), beryllium, silicon, and a doped-CH layer (doped with 6% Si). The inner CH layer



serves as a surrogate for the cryogenic layer. A surrogate target can be imploded more easily on the NIF as it does not require the hardware necessary for cryogenic implosions. This target design can therefore be used to study the physics of the implosion without actually imploding cryogenic targets. In an ignition-relevant implosion experiment, the inner CH shell would be replaced with cryogenic deuterium-tritium ice.

The multilayer target is different from the typical CH ablator design (shown in Fig. 2a) used in many fusion experiments. Surrounding the innermost plastic shell is a 5.7  $\mu\text{m}$  thick layer of beryllium. Material properties of Be make it a superior ablator to CH. This layer is then surrounded by a 1.7  $\mu\text{m}$  thick layer of silicon and a 10.2  $\mu\text{m}$  thick layer of silicon-doped plastic. The Si-doped layer has been shown to mitigate laser imprint (the imposition of the single beam nonuniformity on the target) [7] whereas the pure Si layer is expected to mitigate laser-plasma interactions (LPI) that can compromise the compression of the target [8]. The advantages of this multi-layered fusion target as opposed to the CH ablator design are a significant increase in the stability of the implosions, the increased energy coupled to the imploding shell, and mitigation of LPI instability. This design, therefore, can potentially compress more effectively than a target with only a CH ablator, therefore producing more neutrons.

Another crucial part of the target design is the laser beam pulse shape that describes the changes in single beam power over the course of the implosion. Laser pulse shapes can be adjusted independently for each ring of quads, making them a useful tool for tuning and optimizing polar drive implosions. The overall length of the laser pulse is determined by the energy available on the laser system. Up to 700 kJ is normally available to implode room-temperature targets on the NIF.

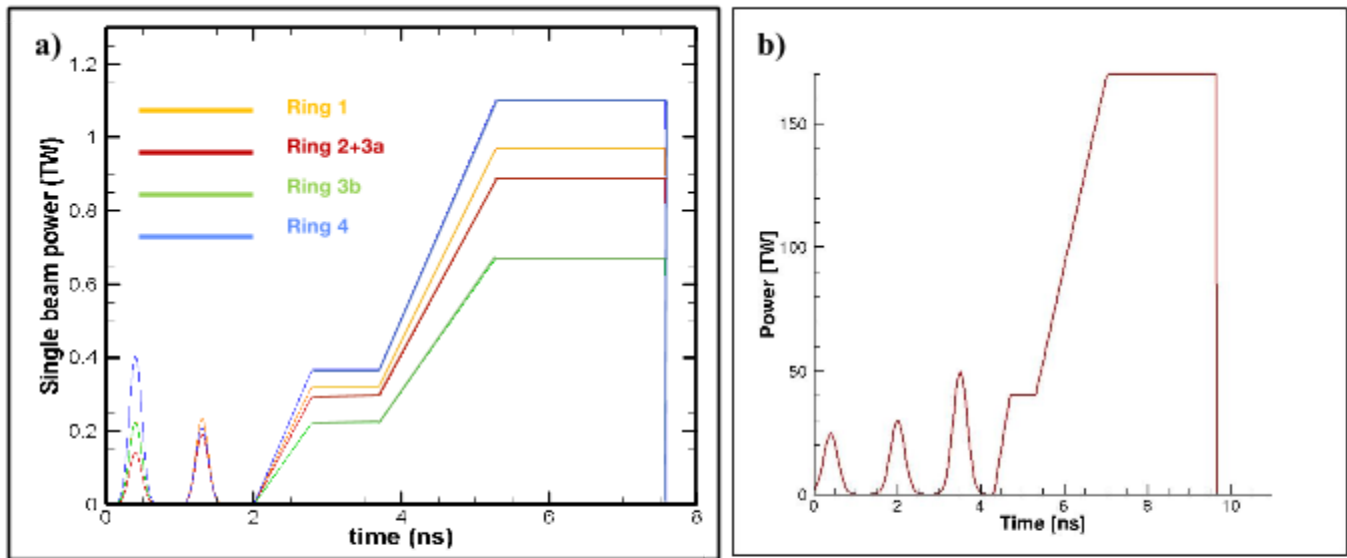


**Figure 3. (a) The double-picket pulse shape for the CH-ablator design showing the beam power in terawatts for each ring. Note that Rings 2 and 3a have identical pulse shapes. (b) The base triple-picket pulse shape used in this work, with the power summed over all 192 beams.**

Shown in Figure 3a are the laser pulse shapes for the CH-ablator implosion.

Preceding the main pulse, there are two jumps or spikes in single-beam power known as “pickets.” These picket pulses generate shocks that travel through the shell of the target and decrease Rayleigh-Taylor instability growth [9] of the target implosion.

Following these two picket pulses is a brief jump in power known as a “foot,” which also launches a shock into the shell. This is followed by the slow rise to the main pulse, which is meant to compress the target adiabatically, meaning that preheat of the target shell is minimized. This results in an effective compression of the target. A triple-picket pulse (Fig. 3b) before the main pulse is more effective than a double picket pulse to achieve higher compression. In a triple-picket pulse shape implosion, there are four

shocks launched into the shell that precede the main pulse, one for each of the three picket pulses and then one for the foot pulse before the rise to the main pulse. The shocks move through the shell first, compressing it, and then break out of the shell and move into the internal  $D_2$  gas. This transition between the layers during the implosion is called a “shock breakout”. The beam pulse shape explored in this work is a triple-picket pulse in combination with a multi-layer target (Fig. 3b). Because there are differences in coronal absorption between the CH ablator target and the multi-layer target, the beam pointings and energies must be readjusted to achieve a uniform implosion using the pre-designed beam profiles.

### **III. Improving Uniformity**

The hydrodynamics modeling code *DRACO* [10] was used to simulate implosions of a multi-layer target with a triple-picket pulse beam shape and identify an optimal set of parameters to maximize uniformity. A systematic approach was employed by first modifying the beam pointings to achieve better uniformity of the initial on-target intensity. Then, the laser-beam picket power ratios in each of the rings were adjusted to reduce nonuniformity at each of the shock breakouts created by the picket pulses before finally optimizing the foot and main pulse to achieve greater overall uniformity throughout the implosion.

It is necessary to keep the initial conditions of the implosion as uniform as possible because any nonuniformity which is introduced early on in the implosion will grow due to the converging shell. Therefore, by optimizing the picket pulse shock

breakouts in the order in which they occur, uniformity can be maintained throughout the entire implosion.

	Original $\theta$ (CH Ablator)	Repointed $\theta$ (Multi-layer)
Ring 1	22.94	27.0
Ring 2	45.0	38.0
Ring 3a	45.0	56.0
Ring 3b	83.48	70.0
Ring 4	83.48	87.0

**Table 1: Original and repointed angles for the rings. Rings were displaced only in their polar angle. Beams were equally spaced in the azimuthal direction within each ring.**

The beam pointings from the CH ablator model shown in Table 1 were used as a starting point for this optimization and adjusted to account for the multi-layer target and triple-picket pulse shape. These beam pointings define the positions of the rings in the northern hemisphere only. Beam displacements are identical in the southern hemisphere. A polar angle of  $0^\circ$  corresponds to the pole and  $90^\circ$  corresponds to the equator. Since the northern and southern hemispheres are symmetric, only the northern hemisphere is simulated in this work. The same improved beam pointings are shown in Fig. 1b.

The initial normalized on-target intensity as a function of polar angle, shown in Figure 4, provided insight into the improved beam pointings that reduce nonuniformity. Regardless of the target type, a higher on-target intensity at the equator compared to the pole is required to compensate for the reduced energy absorption from the oblique angles of incidence of the repointed beams. However, during early runs the intensity at

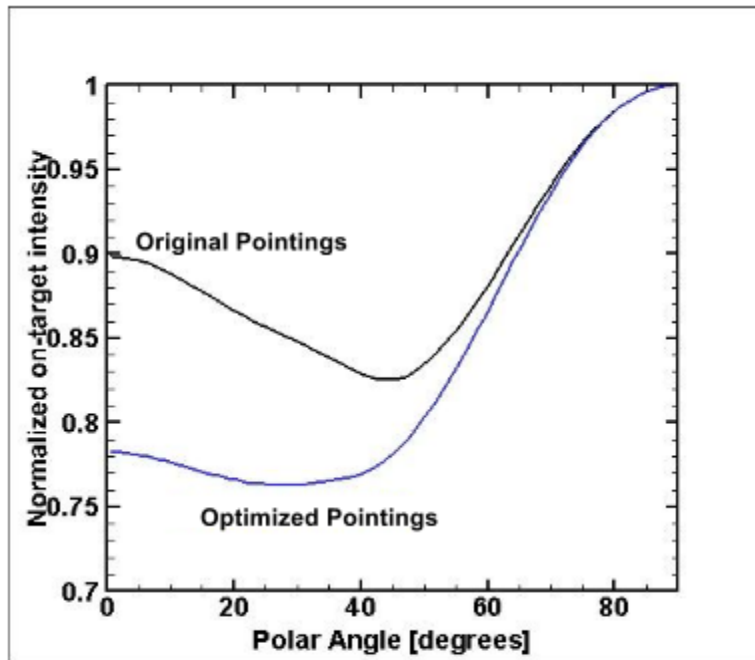
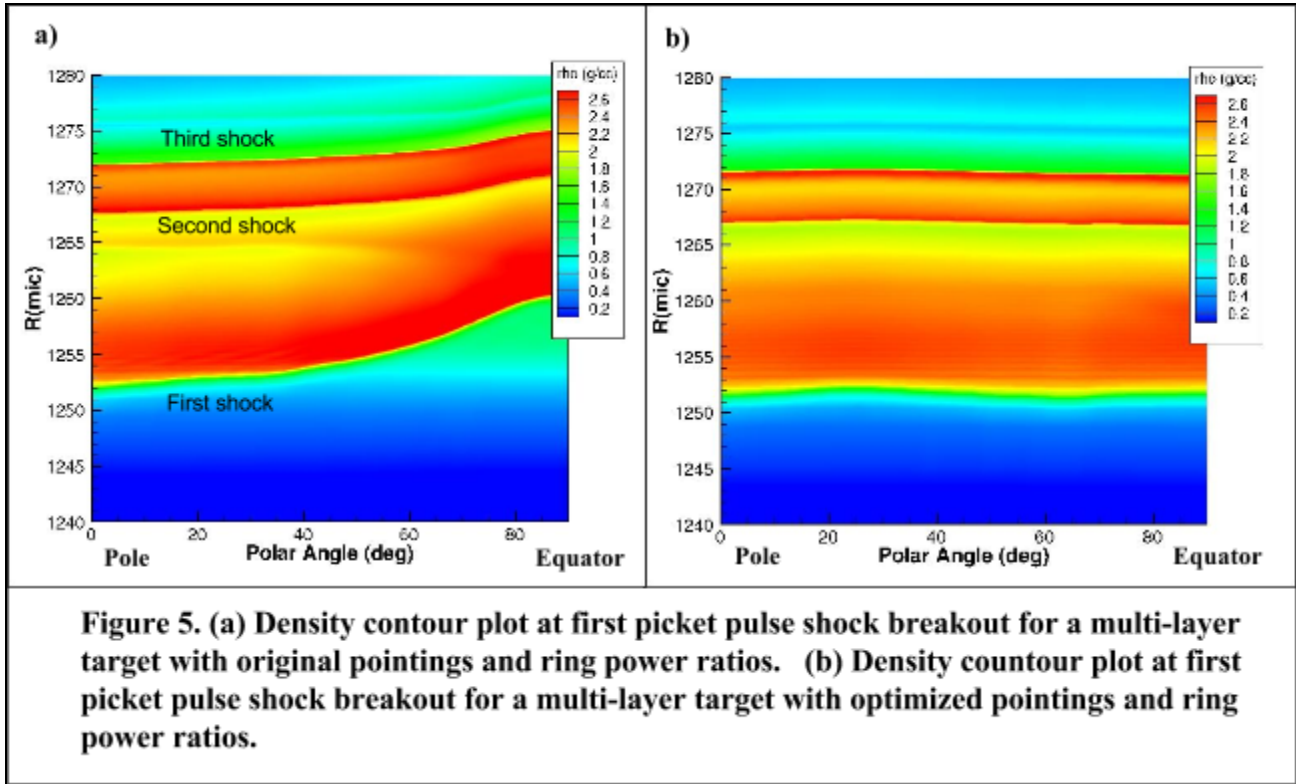


**Figure 4. Initial normalized on-target intensity at 0 ns for an implosion with original beam pointings and the on-target intensity at 0 ns for an implosion with optimized pointings.**

the pole was larger than required, leading to nonuniformities (corresponding to “original pointing” in the Fig. 4). This was identified by the nonuniform first shock in the shell. Therefore, a set of beam pointings were identified where the rings were repointed more toward the equator. This reduced the intensity near the pole, improved the initial on-target uniformity (corresponding to “optimized pointing” in Fig. 4), and resulted in a more uniform first shock.

In Figure 5, a density contour plot is shown at the time of the first picket pulse shock breakout for the original pointings and beam power ratios using a triple picket pulse shape (Fig. 5a), and for the improved pointing and beam power ratios (Fig. 5b).



There is a noticeable lack in drive at the equator compared to the pole in Fig. 5a due to differences in coronal absorption between the multi-layer target and the CH ablator target for which the original pointings were designed. A more uniform shock breakout of the multi-layer target was obtained with optimized pointings and beam power ratios. To achieve this greater uniformity, systematic changes were made to the beam power ratios for each ring at different stages of the implosion. For the first shock breakout, beam power ratios were modified between 0 ns and 1.5 ns. The same process was used to optimize the shock from the second picket.

Of the three picket pulses, the third was shown to have the greatest impact on the overall uniformity of the implosion. The third picket pulse shock breakout (shown in Fig. 6) was also optimized for uniformity using incremental modifications to beam power

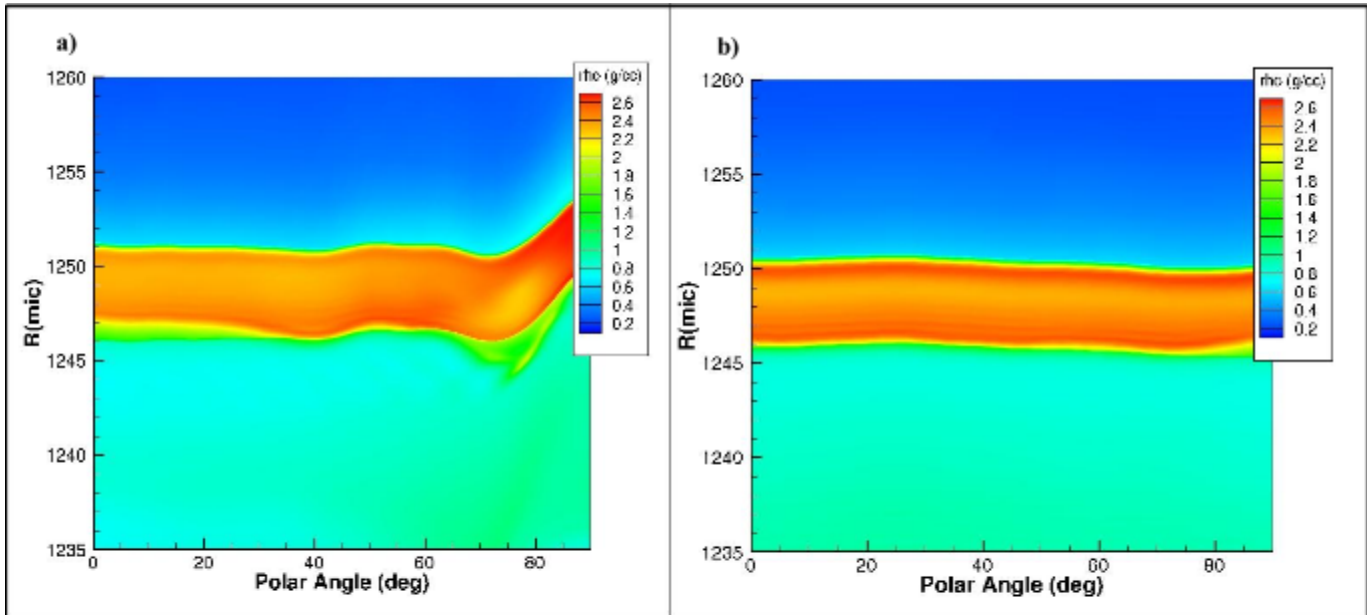


**Figure 6. (a) Density contours of multi-layer target with original pointings and beam power ratios at the time of third shock breakout. (b) Density contours of multi-layer target with optimized pointings and beam power ratios at the time of third shock breakout.**

ratios until a uniform shock breakout was achieved. As shown in Figure 6, the uniformity during the third shock breakout can be greatly improved with changes to

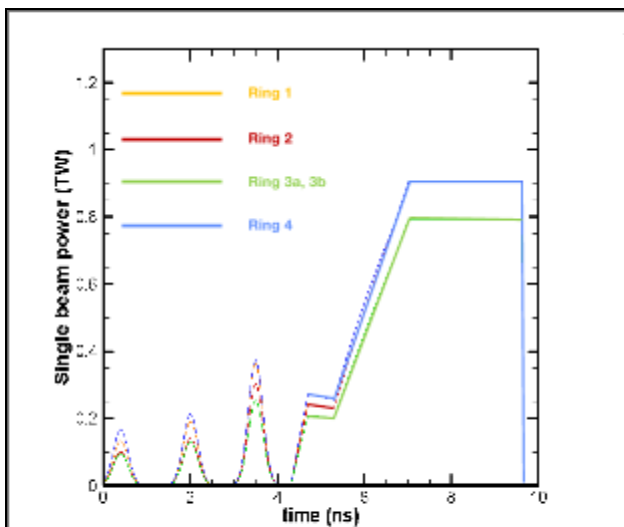
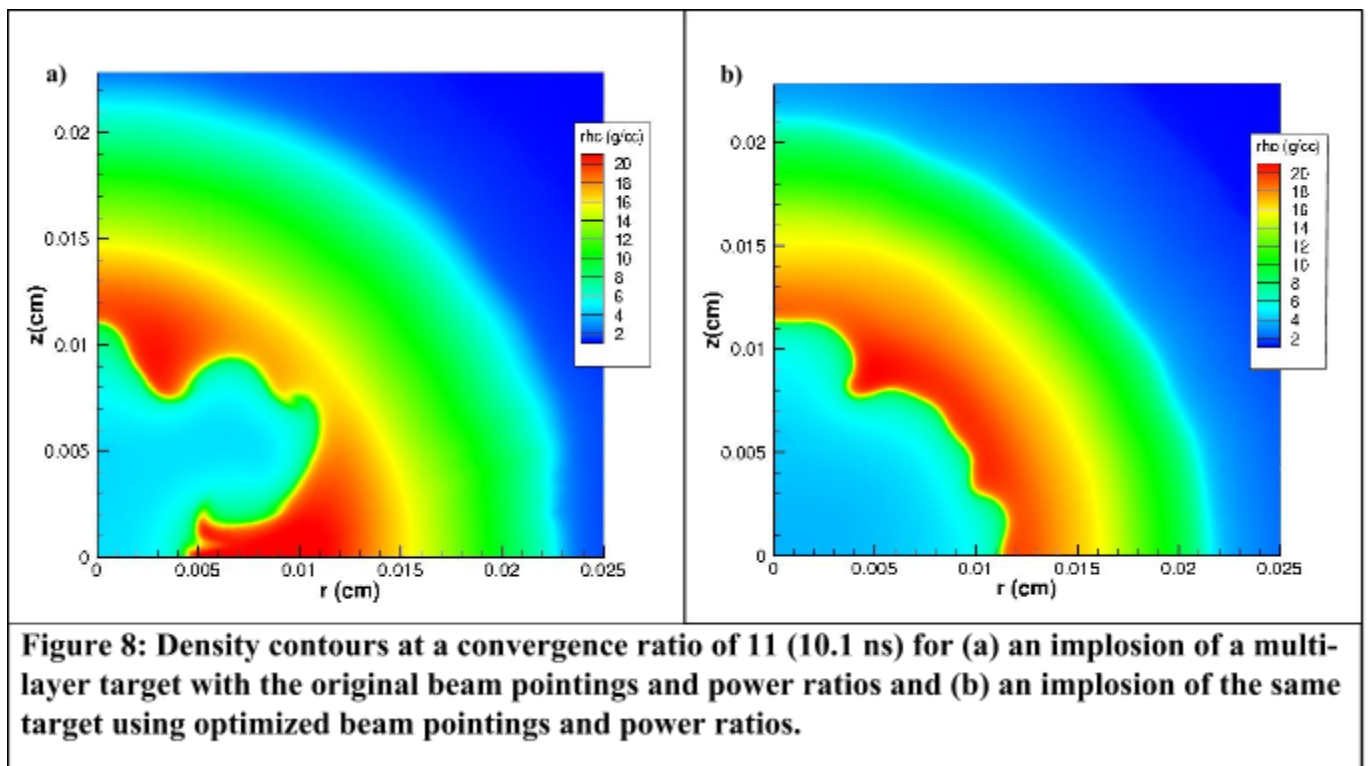


**Figure 7. Laser pulse shapes for all five rings for the optimized multi-layer target design with a triple-picket pulse. During the main pulse, the red curve overlaps with the blue and the yellow curve overlaps with the green.**

beam pointings and power ratios. This systematic method of optimization was then employed to optimize the shock created by the foot pulse in order to achieve a high degree of uniformity throughout the entire implosion leading up to the main pulse. The final pulse shape for the implosion is shown in Figure 7 with all of the optimized beam power ratios. The pulse shapes for rings 3a

and 3b must be the same because both originate from one ring, although slight differences in the energy ratio between the two rings are tolerable. Here, the ratio is kept to 1. Optimizing past shock breakout was accomplished by adjusting the power of each ring during the main pulse to maintain the uniformity of the imploding shell. The late-time results of the implosion using the optimized laser pulse shape and beam pointings are shown in Fig. 8b, along with a late-time implosion of a multi-layer target with the original pointings and beam energies. Here it is easy to see the improvement on the late-time uniformity of the implosion at peak compression.

Hot spot distortion is defined as the ratio of the root-mean-square deviation of the



inner fuel-shell interface from the average radius of the interface and can be used as a quantitative measure of nonuniformity of the compressed core. In Fig. 8a, the hot spot distortion is calculated to be 8.5%, while the hot spot distortion of Fig. 8b is 3.9%. This

shows that hot spot distortion can be reduced by more than half with changes to just beam pointings and beam energies.

#### **IV. Conclusion**

Simulations were carried out using the 2D hydrodynamics code DRACO to optimize the uniformity of a multi-layer target driven by a triple-picket pulse shape using pre-designed beam profiles. A combination of picket energy adjustments and beam repointings were used to create uniform shocks during each of the three pickets and then further adjustments were made to the foot and main pulses to achieve excellent uniformity at peak compression in the implosion. These results suggest that the pre-designed beam profiles are versatile and permit nearly uniform implosions when targets and pulse shapes are varied. The versatility of the beam profiles is of great value because the optics that are used to obtain these profiles on laser facilities are expensive to manufacture and difficult to change once they are in place. The ability to implode varying designs with fixed hardware significantly improves the ability to explore implosion physics.

#### **V. Acknowledgements**

I would like to thank those who helped me in the completion of my project and this report and everyone who made my time at LLE such an incredible experience. First, I'd like to thank Dr. Stephen Craxton for giving me the opportunity to take part in this amazing program and for all the work he has done to give other high school students this experience each year. Second, I'd like to thank all the participants in this

year's high school program for making our work environment so fulfilling and enjoyable and helping me whenever I needed assistance. Third, I'd like to thank Felix Weilacher for all the knowledge and expertise he's shared with me and his continual motivation and support of me throughout my time at LLE. Finally, I'd like to give special thanks to my advisor, Dr. Radha P. Bahukutumbi, for all the countless hours of work she put into designing my project and for her patience and understanding as she guided me through the obstacles and difficulties to reach a successful end to my project.

## References

1. J. Nuckolls, L. Wood, A. Thiessen, and G. Zimmerman, *Nature* **239**, 139 (1972).
2. T. R. Boehly, D. L. Brown, R. S. Craxton, R. L. Keck, J. P. Knauer, J. H. Kelly, T. J. Kessler, S. A. Kumpan, S. J. Loucks, S. A. Letzring, F. J. Marshall, R. L. McCrory, S. F. B. Morse, W. Seka, J. M. Soures, and C. P. Verdon, *Opt. Commun.* **133**, 495 (1997).
3. J. D. Lindl, *"Inertial confinement fusion: the quest for ignition and energy gain using indirect drive"*, American Institute Of Physics, 1998.
4. C. A. Haynam, P. J. Wegner, J. M. Auerbach, M. W. Bowers, S. N. Dixit, G. V. Erbert, G. M. Heestand, M. A. Henesian, M. R. Hermann, K. S. Jancaitis, K. R. Manes, C. D. Marshall, N. C. Mehta, J. Menapace, E. Moses, J. R. Murray, M. C. Nostrand, C. D. Orth, R. Patterson, R. A. Sacks, M. J. Shaw, M. Spaeth, S. B. Sutton, W. H. Williams, C. C. Widmayer, R. K. White, S. T. Yang, and B. M. Van Wonterghem, *Appl. Opt.* **46**, 3276 (2007).

5. S. Skupsky, J. A. Marozas, R. S. Craxton, R. Betti, T. J. B. Collins, J. A. Delettrez, V. N. Goncharov, P. W. McKenty, P. B. Radha, T. R. Boehly, J. P. Knauer, F. J. Marshall, D. R. Harding, J. D. Kilkenny, D. D. Meyerhofer, T. C. Sangster, and R. L. McCrory, *Phys. Plasmas* **11**, 2763 (2004).
6. D. Cao, J. Marozas, T. Collins, P. B. Radha, and P. W. McKenty, “*An Intermediate Far Field Design for Polar Direct Drive at the National Ignition Facility*”, presented at the 57th Annual Meeting of the Division of Plasma Physics, Savannah, GA, 2015.
7. Fiksel, G., S. X. Hu, V. A. Goncharov, D. D. Meyerhofer, T. C. Sangster, V. A. Smalyuk, B. Yaakobi, M. J. Bonino, and R. Jungquist, *Phys. Plasmas* **19**, 062704 (2012).
8. J. Myatt, H. X. Vu, D. F. DuBois, D. A. Russell, J. Zhang, R. W. Short, and A. V. Maximov, *Phys. Plasmas* **20**, 052705 (2013).
9. Lord Rayleigh, *Proc. London Math Soc.* **XIV**, 170 (1883); G. Taylor, *Proc. R. Soc. London Ser. A* **201**, 192 (1950).
10. P. B. Radha, V. N. Goncharov, T. J. B. Collins, J. A. Delettrez, Y. Elbaz, V. Yu. Glebov, R. L. Keck, D. E. Keller, J. P. Knauer, J. A. Marozas, F. J. Marshall, P. W. McKenty, D. D. Meyerhofer, S. P. Regan, T. C. Sangster, D. Shvarts, S. Skupsky, Y. Srebro, R. P. J. Town, and C. Stoeckl, *Phys. Plasmas* **12**, 032702 (2005).

*Modeling Damage Propagation on the OMEGA EP Laser*

**Ryan Gao**

Brighton High School

Advisor: Dr. Matthew Barczys

Laboratory for Laser Energetics

University of Rochester

Rochester, NY

September, 2015

## 1. Abstract

A set of tools was created to simulate the propagation of the OMEGA EP laser after being reflected off a damaged optic. The simulations can be used to assess laser damage threats to subsequent optics due to modulations in the propagated beam. Microscope images of damage on a final OMEGA EP UV target mirror were processed and used as inputs to the simulations. The simulations were validated by comparison with actual propagation images of the same damage regions. The acquired actual propagation images had significant background artifacts due to the camera and laser illumination source that were removed before comparison with the simulations. After the simulation tools were tested, they were used to determine the size of damage on the UV target mirror that would pose the greatest threat to the UV focus lens in the OMEGA EP laser. These tools will be used in the future to evaluate the damage threat to additional critical OMEGA EP final UV optics, such as the distributed phase plate and the vacuum window, in an ongoing attempt to increase UV performance on OMEGA EP shots by better understanding UV optics damage.

## 2. Introduction

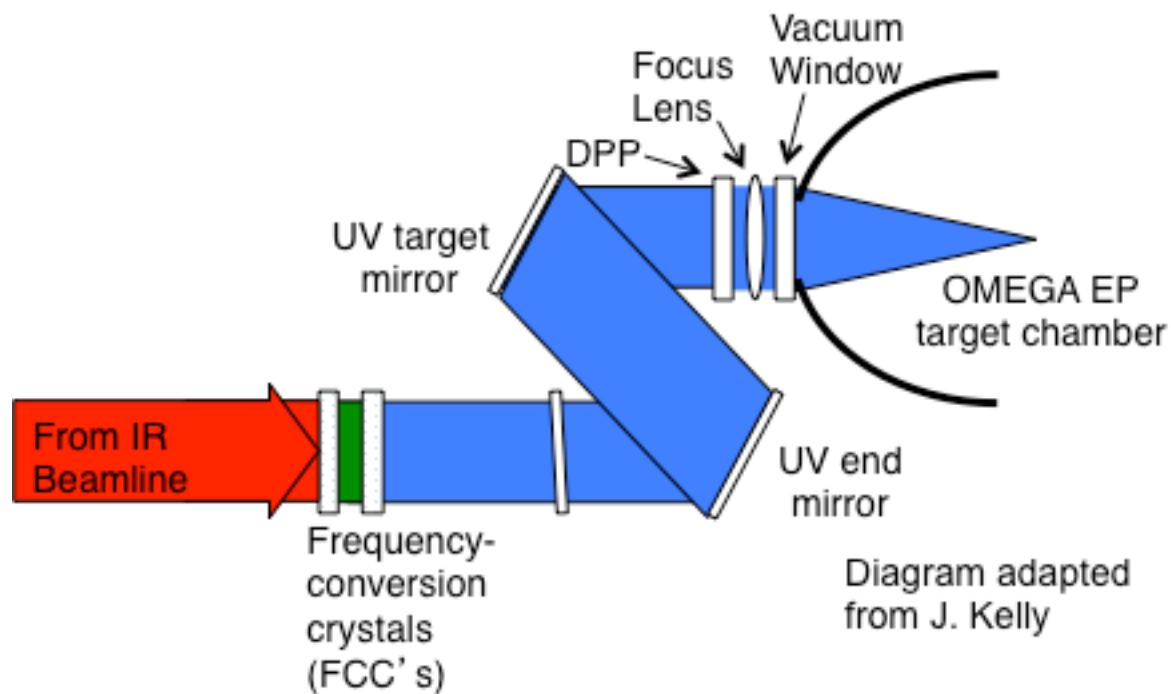


*Figure 1: The final UV optics on the OMEGA EP laser. The DPP, focus lens, vacuum window, and UV target mirror are shown.*

Damage issues related to the final UV optics limit the energy available from the OMEGA EP laser. These optics, shown in Figure 1, start at the frequency conversion crystals where the IR beam is converted to the UV and include two mirrors, a distributed phase plate (DPP) used to smooth the beam, a focus lens, and a vacuum window. The issue of damage on the final UV optics of OMEGA EP was discovered in August 2014 and has led to reduced UV energy limits for most shots. In this situation, a part of the beam was reflected back (a ghost beam), was highly modulated by the DPP, and came into focus near the UV target mirror, resulting in heavy damage in a central square region on the target mirror. This problem has since been resolved

by moving the target mirror so that the beam would focus farther from the UV target mirror. Despite eliminating this damage mechanism, there still is some minor damage occurring on the target mirror. The cause of this damage is unknown, but damage appears to occur randomly over the whole mirror. For the purposes of this work, damage is defined as areas that scatter or diffract light, as opposed to reflect (for a mirror) or transmit (for a lens or other transmissive optic). The damage causes intensity modulations in the main EP beam, which then threaten to damage the downstream final optics including the DDP, the focus lens, and the vacuum window.

While damage does occur to other UV optics, most of the damage that propagates to the final optics is from the UV target mirror, because the target mirror is the closest to these final optics. Therefore, the project focused solely on studying damage propagating from the UV target mirror. These optics are costly and difficult to replace, and as a result, reduced energy limits are set to prevent damage to the final UV optics, meaning the laser is not being used at full capacity. A simulation of damage propagation will be helpful because it allows users to predict how the damage will propagate before the laser is actually shot, therefore hopefully preventing damage on the final UV optics.

### **3. Experimental Setup**

#### **3a. Acquisition and processing of microscope damage images**

First, the simulation of damage propagation was verified by comparing it to measured images of actual propagation from damaged regions. In addition, microscope images of damaged regions were obtained, both for studying damage morphology and for use as input to

the damage propagation simulations. Using a damaged optic that had been taken off OMEGA EP, the technique for visible-light microscope imaging was developed in an off-line lab. After taking images of damaged regions with both an off-axis plasma light source and an on-axis ring light that was attached directly to the microscope, it was clear that the ring light provided clearer images, as shown in Figure 2. After the technique was tested in the lab, it was used with optics still installed on the OMEGA EP laser. Images were taken of multiple damaged regions on the UV target mirror. Only a small portion of the mirror that showed significant damage was imaged. Figure 2 shows a zoomed-in portion of one of these images to more clearly show the detail in one of the damage regions. The size of the imaged region was essentially limited by the microscope that was used and the distance away from the mirror in which it was possible to image the region clearly. So, the imaged region was always much smaller than the 35 cm beam diameter.

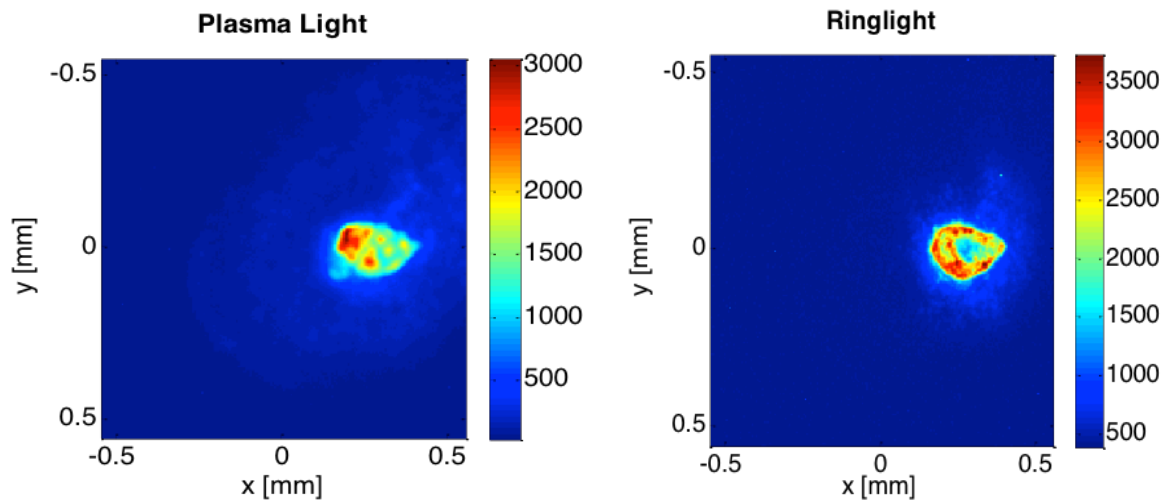


*Figure 2: Damage spot imaged with plasma light source and damage spot imaged with ring light. The ring light was selected since that image shows more detail in the damaged region.*

Because the OMEGA EP laser operates in the UV, but all microscope images are in visible light, the microscope images had to be interpreted to be applicable to what would actually propagate through the final UV optics. When the microscope images were taken, the visible light that is scattered shows up as bright regions on the image. The rest of the visible light passes through the mirror since the mirrors are specifically designed to reflect UV light, not visible light, and will show up as dark regions in the image. Therefore, it is assumed that dark areas are undamaged and will reflect the light well in the UV spectrum. In addition, it is assumed that areas that scatter visible light will also scatter UV light, and therefore these areas are considered damage. To apply these interpretations, the microscope images of damaged regions needed to be inverted, so that damage areas become low pixel values and areas that are assumed to reflect UV light become high pixel values.

In order to invert these images, first all the values were normalized by dividing by the maximum value. This ensures that all of the pixel values in the image are between 0 and 1, and all the values can simply be subtracted from 1 to get the inverted image. Following these steps, all the pixels values are divided by the median value. Since the background is relatively flat and large in comparison to the damage, it is reasonable that the median of the image will essentially be the background value, or region of high UV reflectance, therefore making the values of most background pixels roughly 1. The normalization is important because it allows different images, which may have different pixel values at first, to be compared side by side.

Next, the modified image is thresholded to create a transmission mask. This allows the image to be interpreted so that all values below a certain cutoff limit are considered damage,

and all of the light that passes through these areas will be scattered. In practice, image values from the microscope image of damage that are below the cutoff limit are set to 0, indicating that no light is reflected in these regions. This cutoff limit may have to be varied from image to image, but generally it was found to be around 0.8.

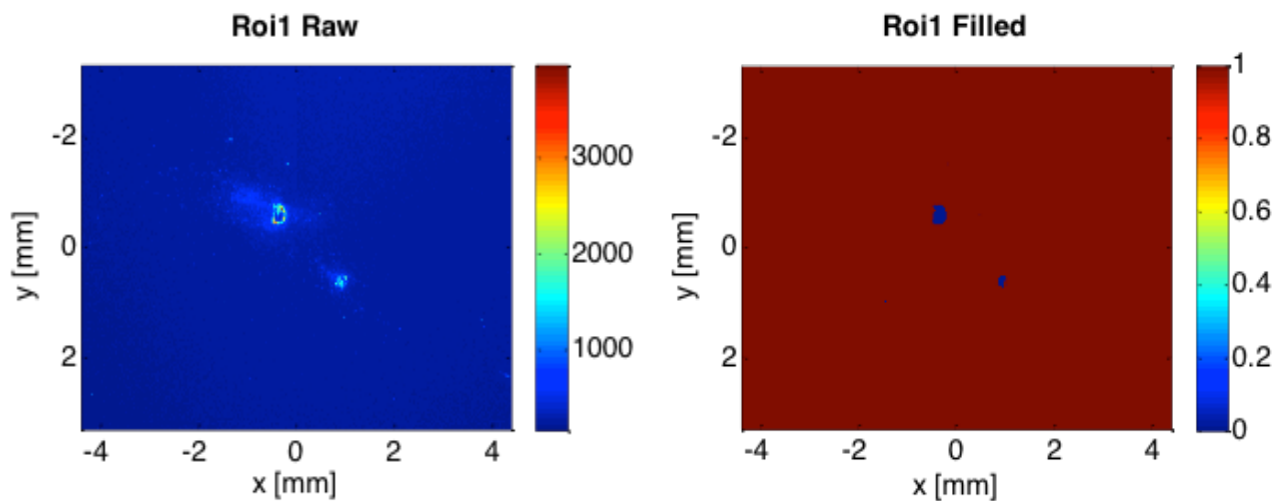


*Figure 3: Original damage image and the corresponding transmission mask. The left shows the original damage image that was taken via a long-working-distance microscope. The right shows the transmission mask, which is the modified image after it is inverted, normalized, and has the damage spots filled in.*

In microscope images of damaged regions, the center of damage often appears dark, as shown in figures 2(b) and 3(a). But it is assumed that the center is still damaged even though the area no longer scatters light. Therefore, the “holes” that appear on the image after thresholding are treated as damage, and filled in and set to 0. An example of the final transmission mask created after all these steps is shown in figure 3(b), which may be compared with a microscope image of that damaged region shown in figure 3(a). The original image is then multiplied by the transmission mask in order to make the image more realistic by including

some of the minor background noise, which may potentially be smaller damage sites. This multiplication preserves the damage regions because they have been set to zero already by the thresholding. Next, a super-gaussian border must be added to the modified microscope damage image. A super-gaussian border can be thought of a mathematically determined edge to the image, so that the color gradually slopes downward from pixel values of roughly 1 to pixel values of 0. The purpose of the super-gaussian border is to limit artificial diffraction around the edges of the image during the simulation, which would otherwise occur due to the steep drop-off from the background of the image, which has pixel values of around 1, to the edge of the image. This artificial diffraction occurs because the image ends abruptly due to the fact that the image is not actually the entire beam. The super-gaussian border reduces this diffraction because it gradually transitions from ones to zeroes at the edges of the image. In order to add this transition at the edges, the modified microscope image of the damaged region is extended in all directions to ensure that when the Gaussian border is added, none of the microscope image of the damage region is disturbed.

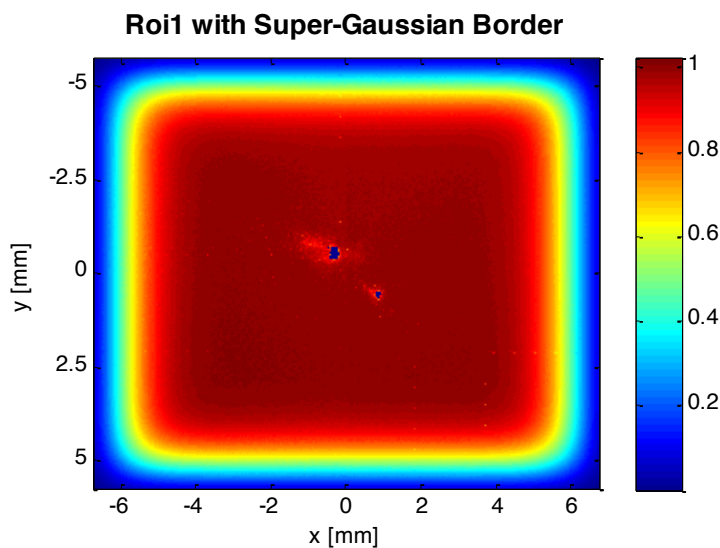


*Figure 4: A damage region just before it is inputted into the simulation, modified by the addition of a super-gaussian border around the edges. The image is artificially enlarged so that no information about the damage region is lost.*

Finally, before inputting the image into the simulation, the images were converted from intensity to electric (E)-field magnitude. The microscope images directly measure intensity, but the input to the Fresnel Propagation program (described below) must be E-field magnitude. The images are converted according to:

$$|E| \propto \sqrt{I}$$

### **3b. Simulated propagation of damage images**

After these steps, the microscope damage images were processed by a Fresnel Propagation code to study how the damage regions modulate an input beam at various propagation distances. The code, developed by LLE scientist, Brian Kruschwitz, is based on an algorithm in Ref. 1. The code simulates the propagation of light at a specific wavelength to a certain distance, which can be inputted into the code. A set of output propagation images is shown on the left of Figure 6 below. Care is also required to properly set the spatial sampling size for the simulation, in order to produce output images that can be subsequently compared to measured images of a modulated beam. After propagation, the code returns the E-field magnitude at each pixel location, which is then converted back to intensity.

A few additional manipulations were performed on the simulated damage images in order to process them in the same way that the measured propagated damage images were processed, as described below. In particular, the images were median filtered in an 110  $\mu\text{m}$ , or 20x20 pixel, box for the images that were used. Median filtering is the process of setting every

pixel equal to the median pixel value of a box of a specified size around it. This smoothens the image and makes it more realistic in this case. The last step before comparison is removing the super-gaussian borders by simply displaying the region inside of the borders, since these were artificially added.

### 3c. Acquisition of actual propagation images

In order to verify the simulation, the simulated propagation images were compared with actual propagated images. To do this, propagation images were taken on the OMEGA EP laser using a UV alignment laser beam;

an example image is shown in figure 5. Images were taken at varying propagation distances from the OMEGA EP optic of interest (the UV target mirror)

from 41 cm to 81 cm at

increments of 10 cm. Before

comparison with the simulation,

artifacts in the measured propagation

images had to be eliminated. Artifacts in the propagation images were due to the UV alignment

beam, which is not perfectly flat. As a result, there were areas of high and low pixel values in

the background that would affect the image statistics if they were not removed. To do this, the

image was first median filtered with a 200x200 pixel box. The 200 pixel box is quite large, so it

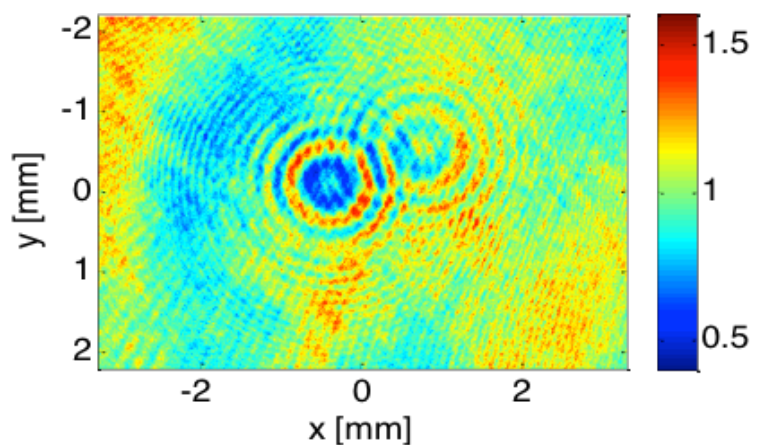


*Figure 5: A raw damage propagation image from the OMEGA EP laser. There are image artifacts that need to be eliminated prior to comparison with simulated images.*

effectively removes the damage spots, which are small relative to the size of the background. However, it mostly leaves the large-scale features of the UV alignment beam. As a result, the median filtered image can be subtracted from the original image to leave the damage spots with a relatively flat background. The resulting image is then median filtered again, this time using a 20x20 pixel box. This removes fringing in the image due to interference in camera optical elements. In order for the images to match up visually, the actual propagation images were also rotated to match the orientation of the initial damage site microscope images.

#### **4. Analyzing the images**

The actual and simulated propagation images were compared qualitatively and quantitatively to validate the simulation results. Figure 6 shows that the images display many qualitative similarities, particularly with the size and amplitude of the diffraction pattern peaks and valleys, throughout all distances, from 41 cm to 81 cm. Figure 6 includes the actual and simulated images from the damage image in Figure 5. Quantitative analysis was performed on the pixel values from the images to measure the modulation of the beam as a result of the damage on the target mirror. One important measure of the modulation enhancement is the peak-to-mean ratio for a damage propagation image. The peak is the brightest pixel in the image and, in this case, the mean was essentially 1 because the background was normalized to 1 for both the measured and simulated images. The peak-to-mean value is significant so that these images can be more generally compared with other images that are not normalized, such as beam profiles of the OMEGA EP UV beam itself. It can also be seen that the diffraction pattern size is the same in both the simulated and actual propagation at the varying distances.

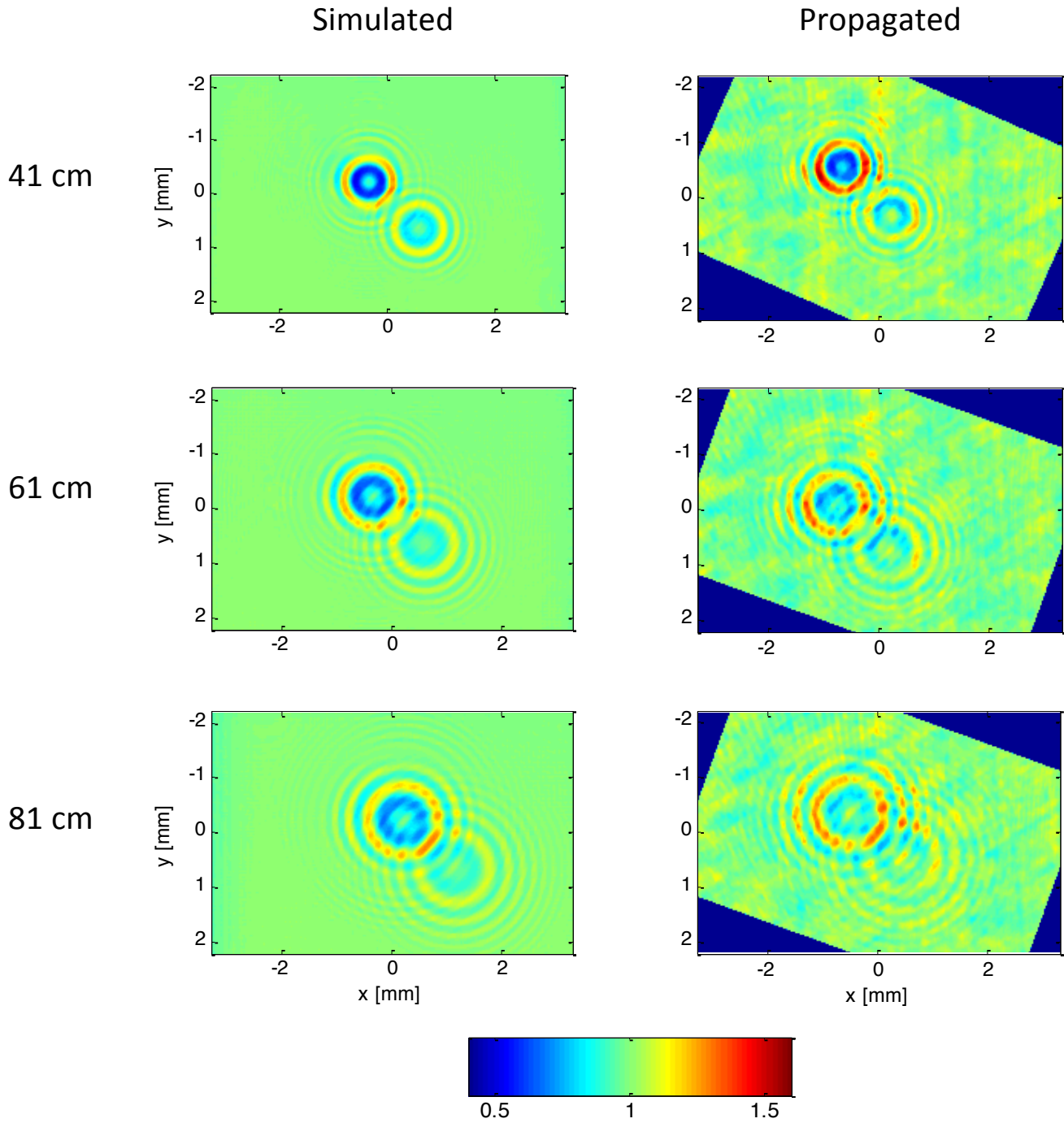


*Figure 6: A side by side comparison of the simulated and actual propagation images at varying distances. Simulated images are shown on the left; measured propagation images are shown on the right. In all of the images, there is good agreement between the size and amplitude of the propagating diffraction pattern resulting from damage on the UV mirror being studied.*

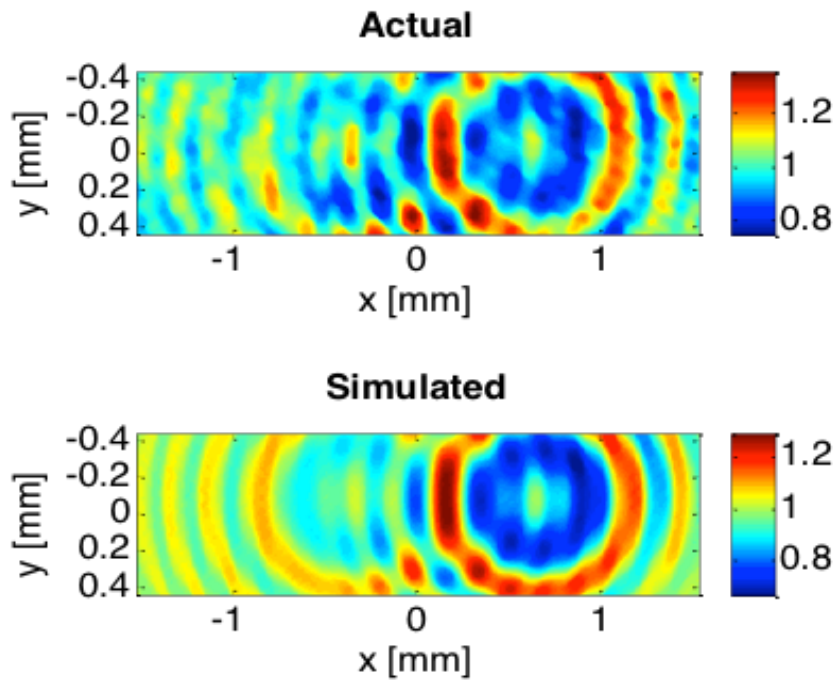


*Figure 7: A close up comparison of the damage regions in both the simulated and actual propagation images. These regions were used to generate the graph shown in figure 9.*

In addition, line plots were made to compare pixel values in corresponding regions of the simulated and measured damage propagation images. A program was written to create such a line plot over a specified box size, and at an arbitrary angle, in both measured and simulated images. Figure 7 shows close-up intensity contour plots of the damage regions shown in Figure 6 at 81 cm. This gives a visual comparison of the structures in the two images. Figure 8 gives line plots corresponding to Figure 7, found by averaging over the whole vertical region shown in Figure 7. Figure 8 shows close similarity between the propagated and simulated regions with the shapes of the diffraction patterns in good quantitative agreement.

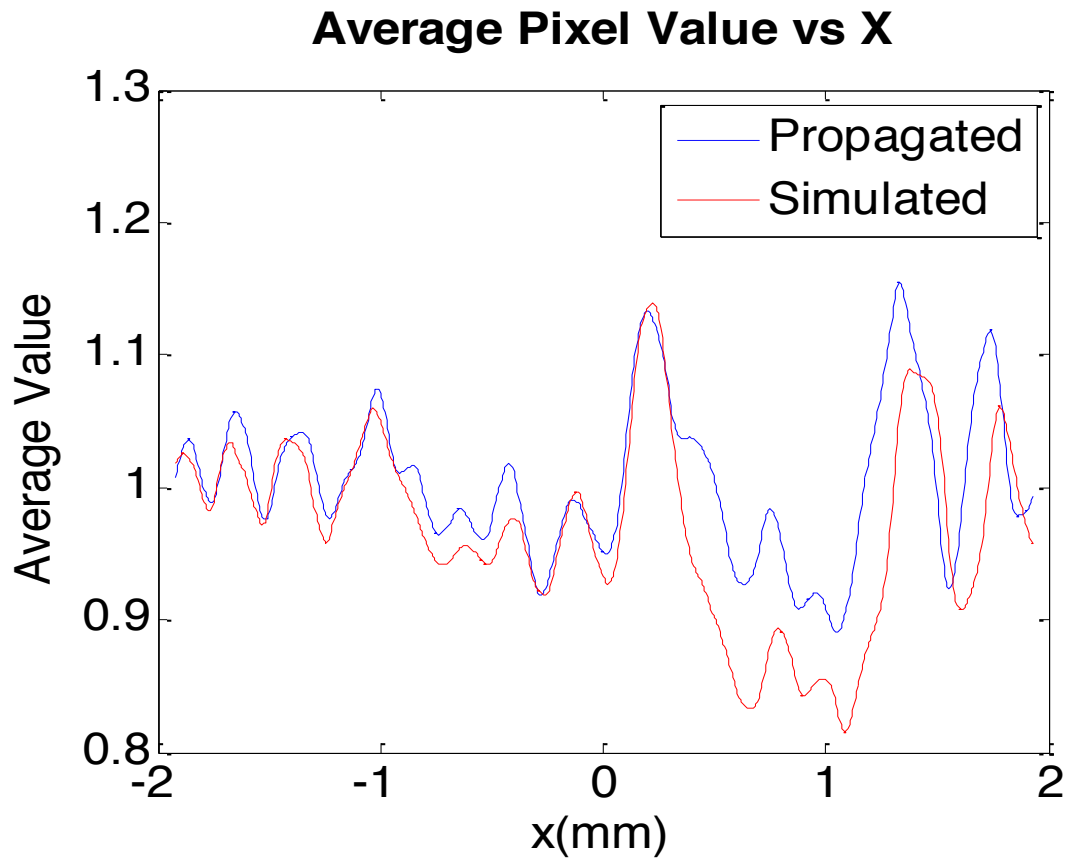


*Figure 8: Plots of the average pixel values (found by averaging vertically in the entire damage region against horizontal distance). The propagated and simulated match closely, in both shape and intensity.*

## 5. Applications and Future Possibilities

This simulation program can be used in the future to predict how damage will affect the laser before a shot is actually taken. Most importantly, the simulations can be run with actual optic damage taken from the laser, to predict whether that damage is harmful to the final UV optics on the laser. Additionally, these simulations provide insight into how real damage propagates. Applications of these simulations also include using them to find the size of damage that will result in the greatest effect on downstream optics at a fixed distance, or the

distance at which a fixed size of damage will result in the greatest damage to downstream optics.

## **6. Conclusion**

In this project, a set of tools was created and verified to simulate downstream propagation of damage from the UV target mirror on OMEGA EP. The tools were shown to result in simulated propagation images that have reasonable agreement, both quantitatively and qualitatively, with actual propagation images taken on the laser. Downstream propagation is a concern because it threatens to damage expensive final UV optics in the OMEGA EP laser, including the distributed phase plate, the focus lens, and the vacuum window. Energy limits are currently imposed in order to preserve these optics, but as a result of these simulation tools, there is the opportunity to better understand which shots and which pieces of damage will have the greatest effect on the downstream optics. This work is part of an ongoing effort to increase the overall UV performance on shots with the OMEGA EP laser.

## **7. Acknowledgments**

First, I thank those at the UR Laboratory for Laser Energetics for giving me this unique opportunity. I would like to give special thanks to my mentor, Dr. Matthew Barczys, for leading me every step of the way and always being there for my questions. I also thank Dr. Stephen Craxton and everyone else involved in running the high school summer program; it was an invaluable growing experience for me as both a person and a scientist. The completion of this project would not have been possible without help from Dr. Brian Kruschwitz, who wrote the Fresnel Propagation program, Dr. Koslov and Dr. Papernov from the damage test group who

allowed us to borrow a long working distance microscope and the plasma light source, Ms. Rigatti from the optical manufacturing group who arranged for us to study a UV target mirror in the system science lab, and Mr. Gibney from the optical mechanical group who worked with Dr. Barczys to obtain damage propagation images. Finally, I thank my fellow interns for their moral support and willingness to help whenever I got stuck on a part of my project.

## References

---

<sup>1</sup>Fienup, J. R. "*Phase-retrieval algorithms for a complicated optical system.*" *Applied Optics* 32, p1737-1746 (1993).

*Analysis of Unabsorbed Light from Exploding-Pusher Targets Used for Proton Backlighting on  
the National Ignition Facility*

**Phoebe Huang**

Webster Schroeder High School

Advisor: Dr. R. S. Craxton

Laboratory for Laser Energetics

University of Rochester

Rochester, New York

March 2016

## 1. Abstract

There is substantial interest in proton backlighting on the National Ignition Facility (NIF), requiring a small number of beams to be pointed at a secondary backlighter target (a thin shell containing  $D^3He$  that produces a burst of protons when it implodes) while a larger number irradiate a primary target. The protons provide a diagnostic of the primary target by being deflected or absorbed as they pass through it. Optimized designs for different size proton backlighter targets, using 32 of the 192 NIF beams, have been developed using the hydrodynamics simulation code SAGE. Small targets are desirable for producing a small proton source size. In all cases, the phase plates (optics that set a large beam size at best focus) are assumed to remain in the system (to avoid the time that would be required to remove them for the backlighter beams). It was found, as expected, that the amount of scattered light (unabsorbed laser energy that can pass through the target chamber and damage laser optics on the opposing side) increases as the target diameter decreases from 1500 to 420 microns. Adjustments were made to include the known scaling of optics damage with laser pulse length. These simulations explore the limits of what the NIF can safely shoot.

## 2. Introduction

As the world attempts to move away from fossil fuels and other nonrenewable energy sources, clean energy has become an important topic of research. One developing source of potential clean energy is nuclear fusion. Nuclear fusion can be achieved by irradiating a small, spherical target, consisting of a plastic or glass shell filled with tritium and deuterium, with laser beams. During irradiation, the shell of the target ablates outwards, forcing the fuel inside to be compressed. The compressed fuel reaches high density, pressure, and temperature, allowing for fusion reactions to take place. The extreme conditions are necessary for the deuterium and tritium, both positively charged nuclei, to overcome Coulomb repulsion forces and fuse before the target completely explodes. The fusion of deuterium and tritium produces a helium nucleus and an energetic neutron, the latter carrying most of the energy from the fusion reaction. In a perfect setting, the helium nucleus would redeposit its energy into the fuel and create a chain reaction of fusions in a process called ignition. Ignition is the first step in reaching breakeven, where the energy released by the reaction equals the energy put in by the laser. After breakeven has been achieved, the next goal is high gain, where the energy released by fusion is substantially more than the energy put in by the lasers. To make nuclear fusion into a plausible source of clean energy, high gain must be achieved.

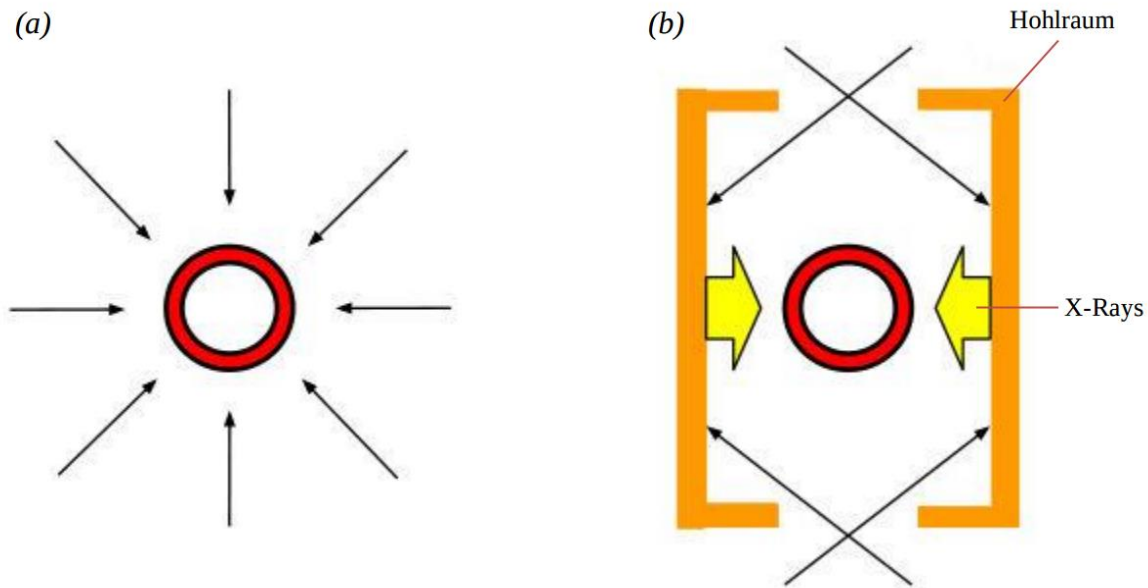


**Figure 1:** The two main approaches to inertial confinement fusion (ICF). (a) In direct drive, the lasers are aimed directly at the target. (b) In indirect drive, the lasers are aimed at the hohlraum, which emit x rays that then irradiate the target. (From Reference 3)

Currently, there are two main approaches used for laser fusion: direct drive<sup>1</sup> and indirect drive.<sup>2</sup> In direct drive Figure 1a, the lasers are aimed at the target and the target is irradiated directly by the laser beams. In indirect drive Figure 1b, lasers are pointed at the inner walls of a hohlraum, usually made of a metal with a high atomic number, so that the target can be irradiated by the x rays emitted by the hohlraum. The Omega laser at the Laboratory of Laser Energetics (LLE) is configured for direct drive, while the National Ignition Facility (NIF) at the Lawrence Livermore National Laboratory is configured for indirect drive. Indirect drive offers better uniformity of the implosion because the target is being irradiated more evenly by the x rays. However, 80% of the energy from the laser beams is either lost in the walls of the hohlraum or escapes through the openings of the hohlraum. The target only absorbs 20% of the energy originally provided.

Even though the NIF is configured for indirect drive, it can be adjusted to perform direct drive by repointing the beams in a method called polar drive. The NIF has a total of 48 beam ports, all evenly spaced around the azimuth ( $\Phi$ ) in 8 rows at angles of  $\Theta = 23.5^\circ, 30.0^\circ, 44.5^\circ,$  and  $50.0^\circ$  from the poles on the top and bottom. The lasers are grouped into quads, consisting of 4 beams; in total the NIF has 48 quads, or 192 beams. In polar drive, the beams are pointed away from the poles and towards the equator to make up for the lack of ports there, as illustrated in Figure 2.

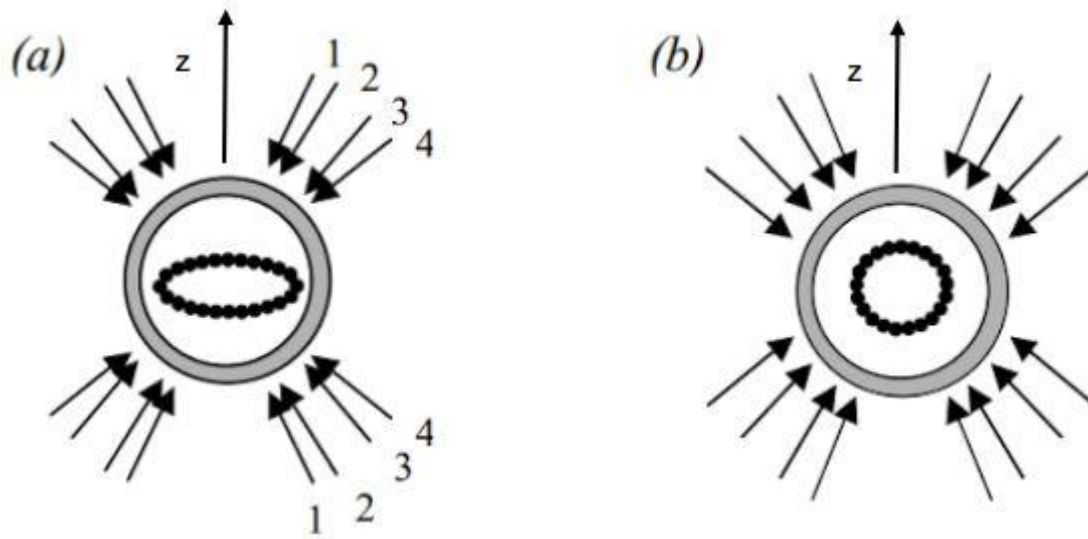


**Figure 2:** Direct drive beam pointings on the NIF. Each arrow represents a ring of quads. (a) With the beams aimed at the center of the target, the deposited energy is unevenly spread. The result is a much faster implosion at the poles than at the equator. (b) Repointing the beams towards the equator for the polar drive approach spreads out the energy more evenly, allowing for a much more uniform implosion. Based on Fig. 2 of Ref. 4

Using polar drive has been effective in creating uniform implosions during direct drive experiments on the NIF carried out by LLE.<sup>5</sup> It is also being used on the NIF<sup>6</sup> for the development of proton backlighting, a diagnostic technique illustrated in Figure 3. The backlighter and primary target are irradiated with different groups of laser beams. The

backlighter releases protons, which are deflected by the magnetic and electric fields of the primary target, hit a detector, and produce an image.

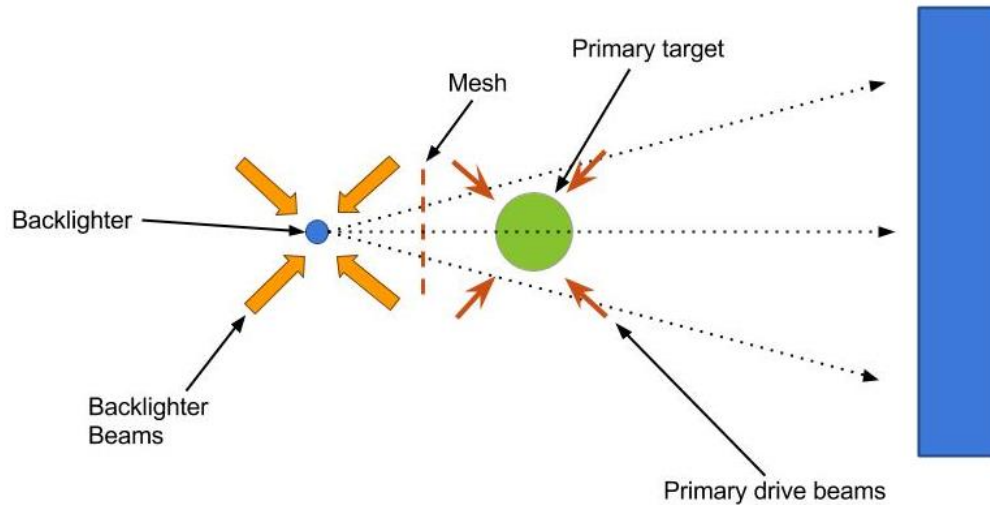


**Figure 3:** The proton backlighter, represented by the blue circle, sits behind the primary target, the green circle. A few beams are reserved for the backlighter, while most are pointed at the primary target. The backlighter beams irradiate the backlighter target directly, and release protons (dotted lines) that will produce an image providing information about the magnetic and electric fields of the primary target.

This project focused on the proton backlighter. The backlighter target in this project has a thin plastic shell, 4 microns thick, and is filled with a deuterium and helium-3 fuel. A small proton backlighter is desirable because a smaller point source leads to higher quality, more focused images, but has the disadvantage that scattered light may damage the laser optics. This project entailed the optimization of several proton backlighter targets of varying sizes and the assessment of their safety. As most of the quads would be required to irradiate the primary target, only 8 quads were reserved for use on the backlighter: every other quad  $44.5^\circ$  from the poles.

Another restriction was that phase plates, optics placed in laser beams to increase their size, spread, and uniformity in the target plane as shown in Figure 4a, must be used. Removing the phase plates takes a lot of time, so if the backlighter can be used with phase plates left in, it

will save a lot of time and expense. Current direct drive implosion experiments on the NIF use the phase plates (designed for indirect drive) with appropriate repointings and defocusing as proposed by Cok et al.<sup>4,7</sup>

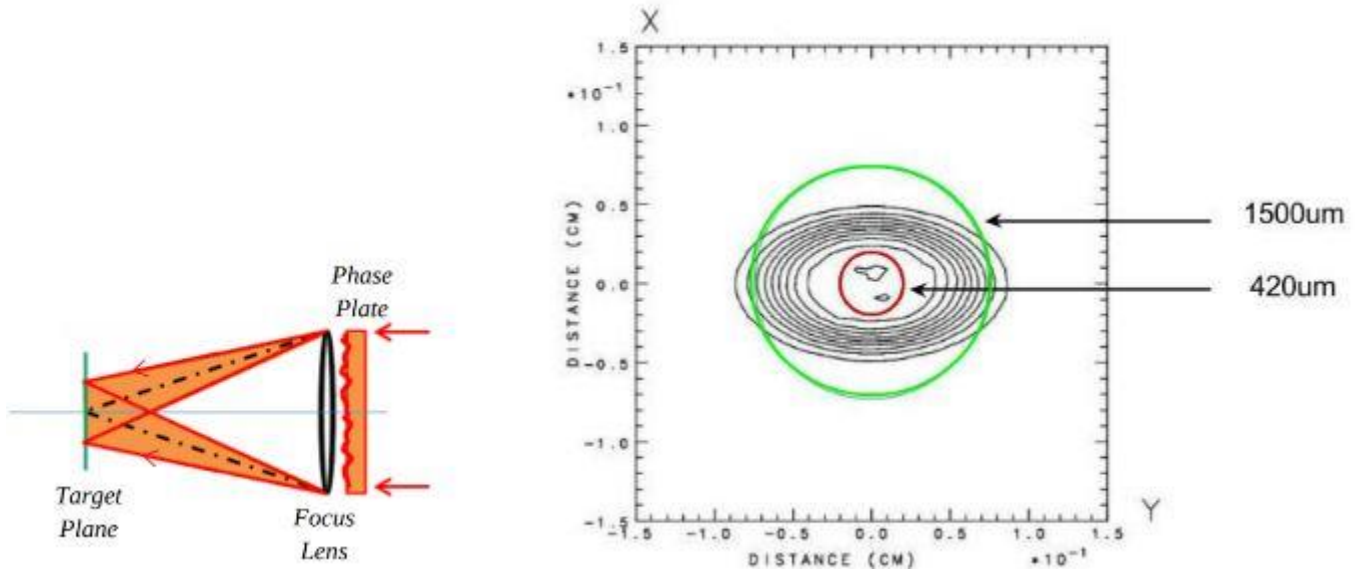


**Figure 4:** (a) Phase plates increase the size and spread of a beam to increase uniformity in energy distribution in the target plane. (b) The dark, oval rings represent intensity contours of the laser beam. A target with a larger diameter, in green, covers more area and can absorb more energy from the pulse. The smaller target, in red, is not big enough to absorb much energy. Most of the beam blows by it on the sides. (Based on Fig. 11 of Ref. 3)

An ideal implosion has minimized amounts of scattered light, to prevent possible damage to laser optics on the opposite side of the target chamber, and maximized uniformity. Depending on the size of the target and on where the beams are repointed, different amounts of scattered light, or unabsorbed energy, are produced. This can be seen in Figure 5, which shows ray-trace plots for two different target sizes.

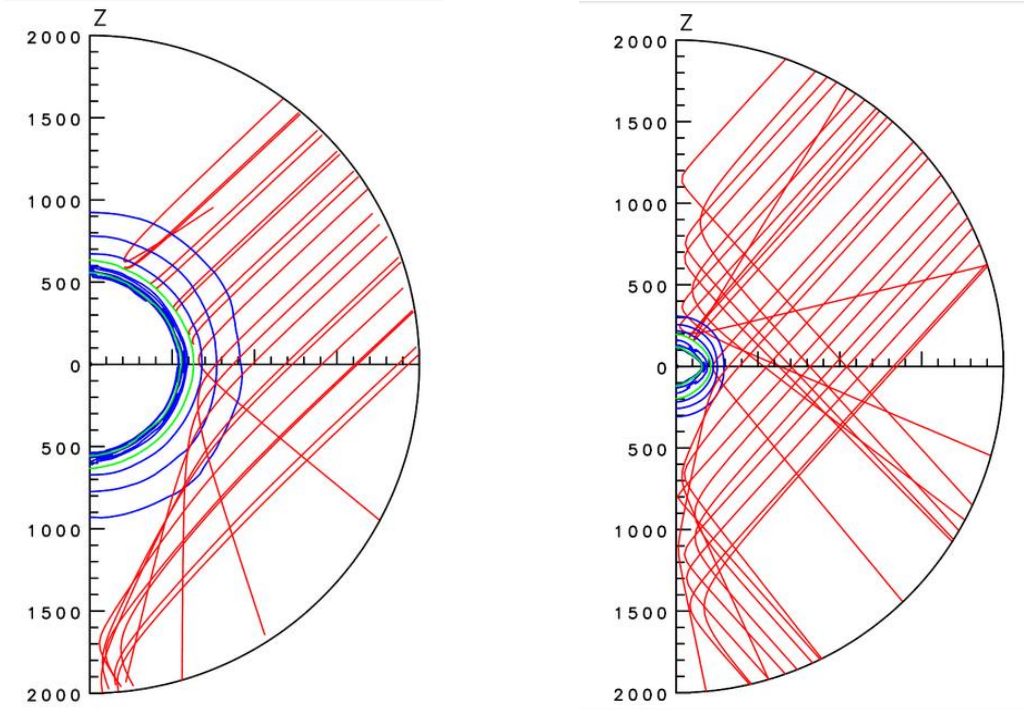


**Figure 5:** Ray trace diagrams show how the difference in size affects how each target absorbs energy. On the left is a 1500 micron target and on the right is a 420 micron target. The red lines represent the beams and the blue is the target. Notice that the beams are not aimed at the target center; this is a result of repointing for polar direct drive. The slant comes from the port angle. The 1500 micron target blocks most of the red rays, but the smaller target does not. The excess beam energy that is neither absorbed nor blocked becomes scattered light.

Scattered light is produced when not all the energy provided by the laser is absorbed by the target. Repointing beams can cause an increase in scattered light because many rays no longer point directly at the target and are not completely absorbed or blocked by it. Repointed beams give a better spread of energy and better uniformity because they cover more area. However, if scattered light increases too much, the design is not viable. Phase plates also increase the spread of a beam and contribute to better uniformity at the price of increased scattered light.

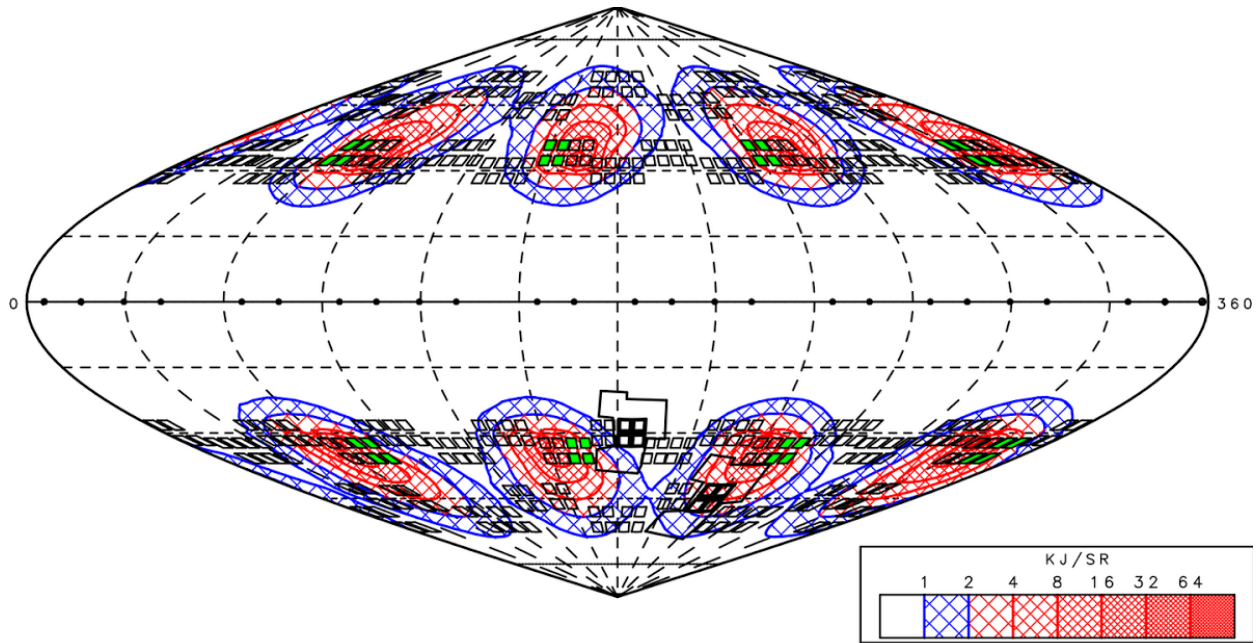


**Figure 6:** This scattered light contour plot shows where the excess energy from the beams is hitting. The red areas are where the most energy is concentrated, and blue is the least. The quads in green are the ones being used. The most concentrated red areas are extremely close to the green quads, indicating that much of the excess energy is hitting close to the ports being used on the opposite side of the target chamber.

Figure 6 gives a contour plot of the scattered light as a function of angle for a target with diameter 1000 microns. The regions of greatest scattered light lie very close to the beam ports being used (shown in green). The quads used are almost directly across from each other, and if too much excess energy gets into them, the mirrors in the laser beam path can be damaged. For each design, the maximum scattered light at any angle was used to assess the damage risk.

### 3. Simulation results

An optimized design for a 1500  $\mu\text{m}$  diameter target developed by Garcia<sup>8</sup> was used as the starting point for data collecting and was the only 1500  $\mu\text{m}$  diameter target analyzed. Optimized designs for targets of 1000, 800, 600, and 420 micron diameters were created by varying the beam position, focus, and pulse length. The designs were optimized for good uniformity. Three

designs with best uniformity at each target size were typically chosen and their amounts of scattered light graphed.

Optimization of targets proceeded in descending order of their diameters. For each new target size, the first two runs used Garcia's design and the design with best uniformity from the previous design to provide starting points for the optimization. In the case of the 1000 micron diameter target, just Garcia's design was used as the starting point. For the 1500 micron diameter target, Garcia's design produced a nonuniformity of 1.53% and a maximum scattered light flux of 31.6 kJ/sr up to the time of peak implosion, equivalent to  $0.05 \text{ J/cm}^2$  on the laser optics. An example of a design optimized for uniformity is given in Figure 7, which shows contours of the center-of-mass radius for a 1000-micron target. The poles and equator were significantly underdriven in the starting design, so in the optimized designs [Figure 7], three out of the four beams in each quad were pulled towards the equator and the remaining one was aimed closer to the pole. This provided a much better uniformity.

The original plan was to use best focus for all the designs to reduce the amount of scattered light by as much as possible, but it was found that with defocus, the amount of scattered light did not increase by too significant of an amount but uniformity improved. Defocusing the beam increases its spread. The best design created for the 1000 micron target had a nonuniformity of 1.82% and produced 54.3 kJ/sr of scattered light at its time of peak implosion. The same method was used for optimizing the 800 and 600 micron diameter targets, which had similar designs to the optimized 1000 micron diameter target. The best design for the 800 micron diameter target produced a nonuniformity of 4.11% and 59.8 kJ/sr of scattered light. The best design for the 600 micron diameter target produced 5.64% nonuniformity and 73.0 kJ/sr of scattered light.

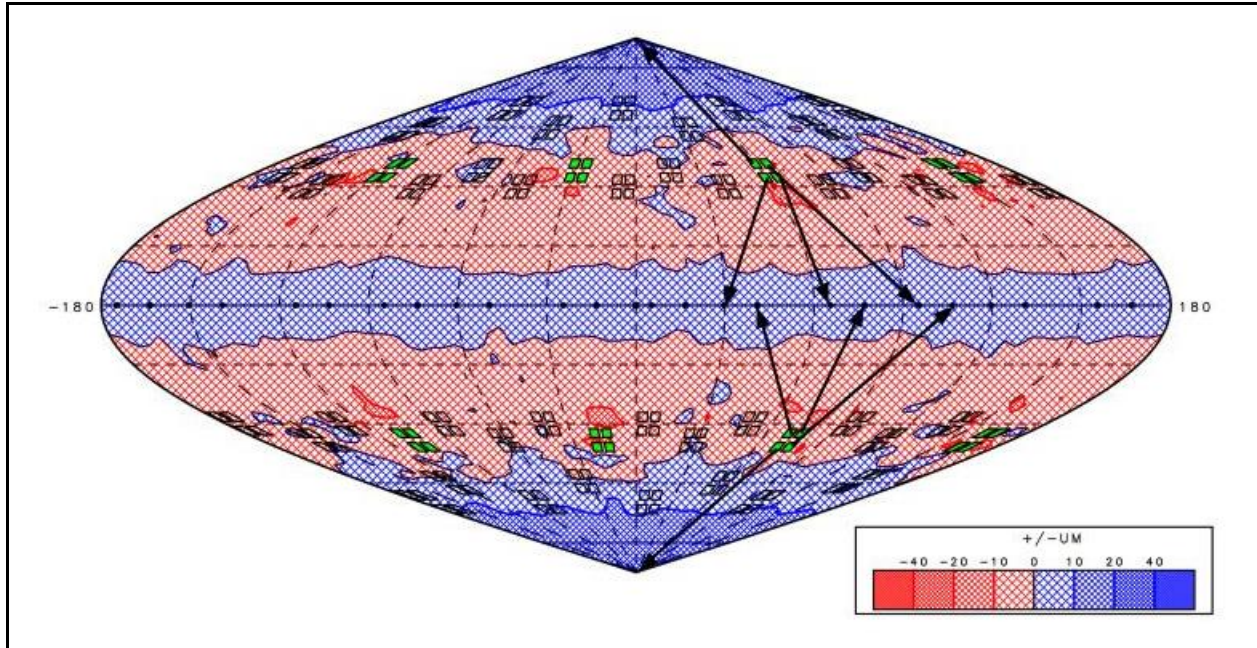


**Figure 7:** Contour plot of deviation in the center-of-mass radius of the imploding shell when the shell has imploded approximately half way, on a sinusoidal projection of a 1000 micron target, showing the entire surface. The green quads are the ones in use and the black arrows show where each beam of a quad is pointed in an optimized design. Red areas are overdriven and blue areas are underdriven. Variations of this design were tested with different beam defocuses to achieve a better uniformity but with a minimal increase in scattered light. The optimized designs for the smaller targets were very similarly structured.

Simulations for the 420 micron diameter target began the same way as the others, but it was found that the target was imploding before the beam had reached full power. Therefore, the length of the beam was changed from 2.1 ns to 1.1 ns and the time to reach full power was decreased from 1.0 ns to 0.2 ns. The thickness of the shell was also changed from 4 microns to 2 microns. The optimized design had a nonuniformity of 5.62% and produced 83.9 kJ/sr of scattered light.

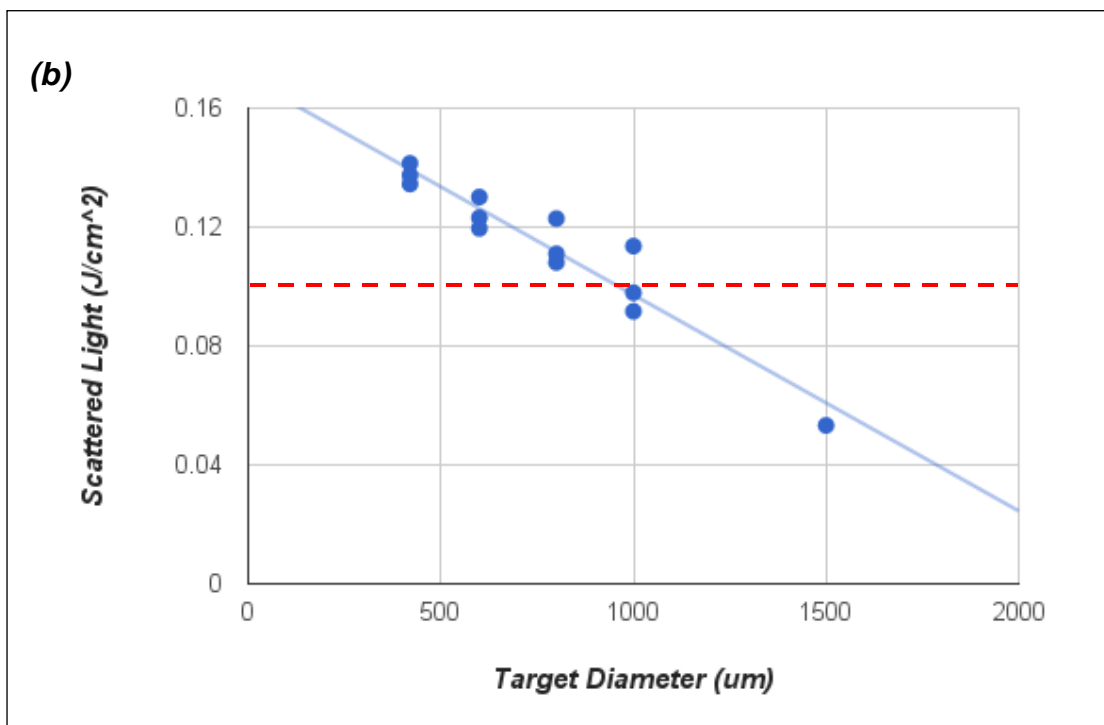
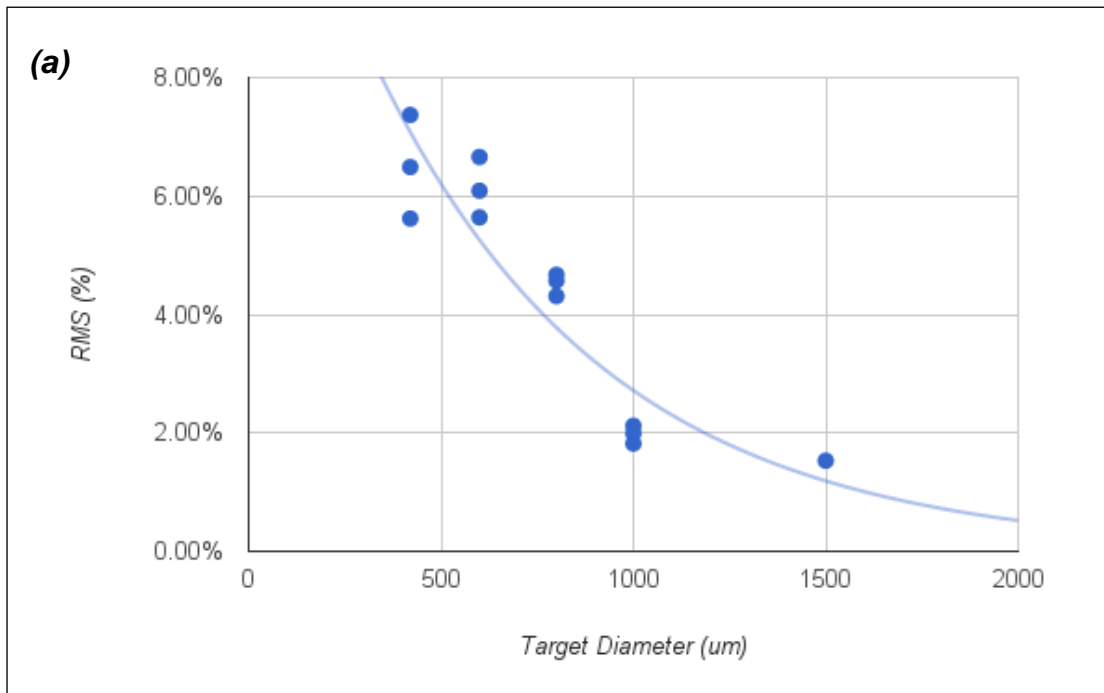


**Figure 8:** Graph (a) is of uniformity vs target diameter for the best designs. Graph (b) is of the amount of scattered light produced by the same designs vs the target diameter. As the target size gets larger, the nonuniformity and amount of scattered light decrease. The red dotted line at  $0.10 \text{ J}/\text{cm}^2$  represents the level of scattered light considered safe.

Graphs of the nonuniformity and amount of scattered light for the best designs are shown in Figure 8. There is a clear trend: both nonuniformity and the amount of scattered light decrease when the target diameter increases. The 1500 micron target is definitely safe to shoot and two out of the three optimized 1000 micron designs are safe. However, these results do not account for the short amount of time in which all the energy hits the mirrors. The same amount of force, applied in a short amount of time, will cause more damage than if it took a long time to completely expend its energy. To accommodate the short pulses, the amount of scattered light measured was converted to find their 5 ns equivalent. Dr. B. MacGowan from the Lawrence Livermore National Laboratory provided the conversion equation:<sup>9</sup>

$$F_{adj} = F(5 \text{ ns}/T)^{0.35}$$

where F is the flux on the mirror,  $F_{adj}$  is the flux adjusted to a 5-ns equivalent, and T is the length of the scattered light pulse.

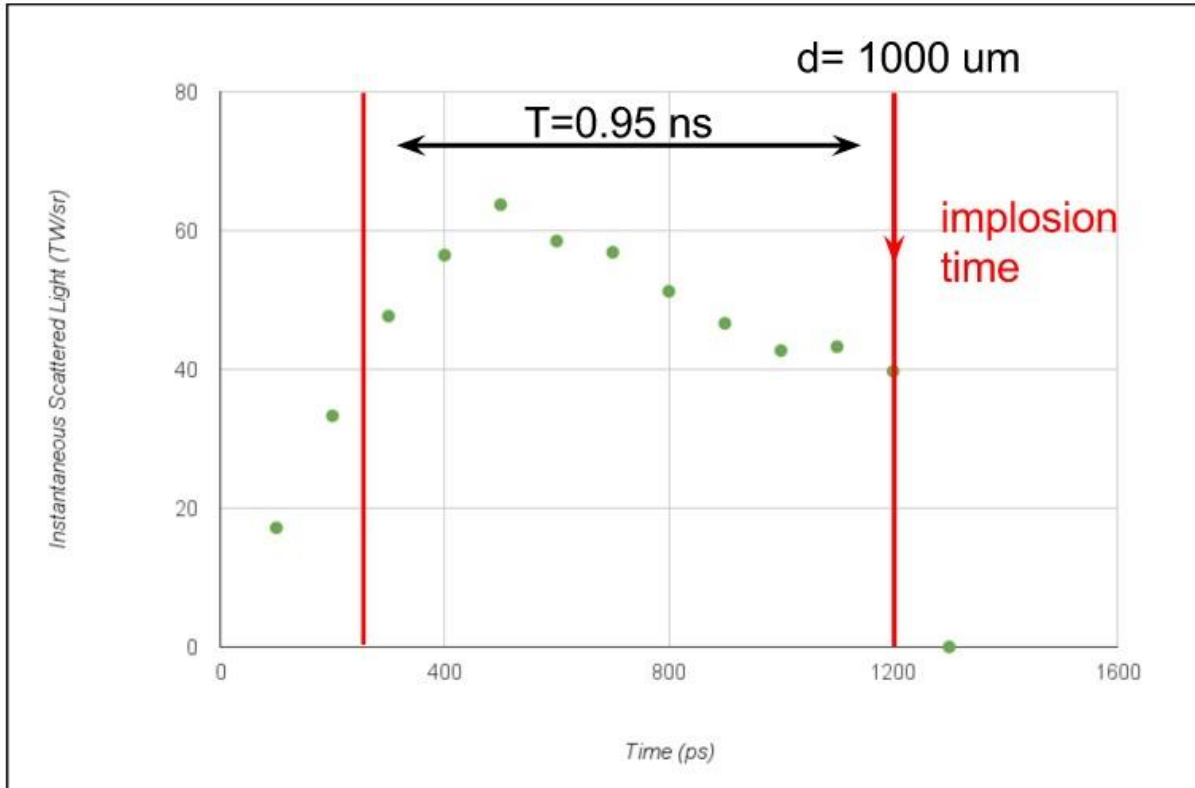


**Figure 9:** A plot of instantaneous scattered light vs time for a 1000 micron target. The red lines mark the beginning and the end of  $T$  (labeled by the black arrow).

To find  $T$ , the scattered light produced every 100 picoseconds was graphed, as shown in Figure 9, and from it the approximate  $T$  was obtained for every target size. The beginning of  $T$  was roughly halfway to the first peak in scattered light and the end of  $T$  was at the time of implosion. This method provides a more accurate estimate of  $T$  than simply taking the pulse length up to the implosion time (around which time the laser pulse would normally be shut off). Applying the formula gave the results shown in Table 1.

**Table 1.** Adjustment factor  $(5ns/T)^{0.35}$  for the various designs.

Diameter	Time (ns)	Factor
1500 um	1.35	1.58
1000 um	.95	1.79
800 um	.80	1.90
600 um	.75	1.94
420 um	.30	2.68

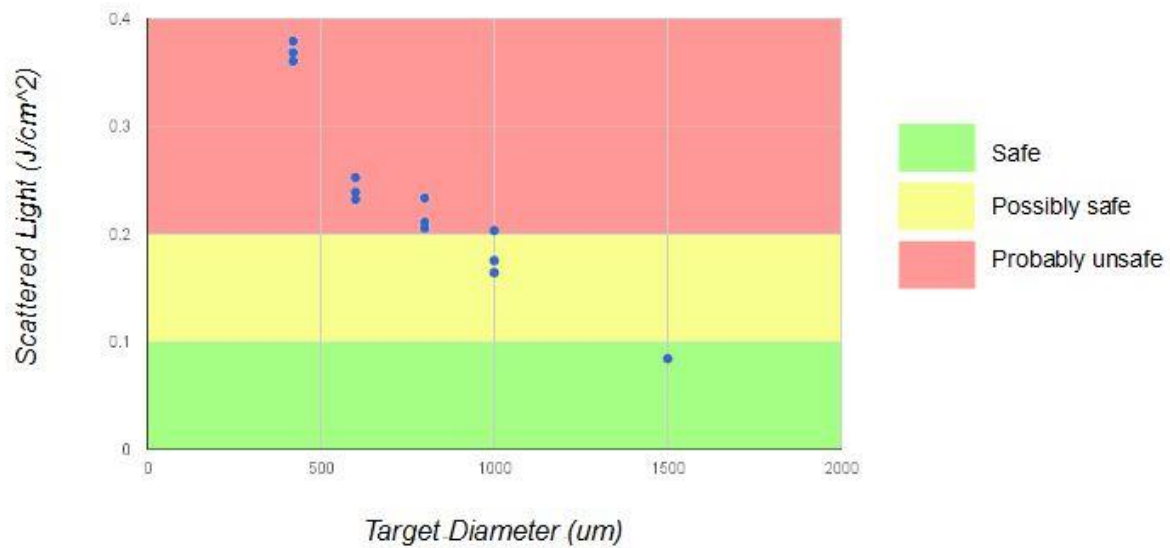


**Figure 10:** This graph is the same as Figure 9b, but with the scattered light fluxes adjusted to a 5-ns equivalent. The zones where the adjusted scattered light renders a shot safe (green), possibly safe (yellow), and unsafe (red) are shown. The only backlighters in the green zone are the 1500 micron ones. The 1000 micron targets fall mostly in the yellow zone. The 800, 600, and 420 micron targets all fall in the red zone.

Using the factors in Table 1, the scattered fluxes of Figure 8b were adjusted to provide more accurate estimates of what is safe to shoot [Figure 10]. The only target that is completely safe to shoot is the 1500 micron one. The 1000 micron target is borderline safe. Two designs for

this diameter are in the possibly safe zone, indicating that further tests will need to be done to determine their viability. The other design is in the unsafe zone, along with all the smaller target sizes.

#### **4. Conclusion**

The amount of scattered light produced in the implosion of proton backlighter targets has been investigated for targets of diameter ranging from 1500 microns to 420 microns. Accurate estimates of the scattered light are required because excessive light passing through beam ports on the opposite side of the NIF target chamber can damage laser optics. Since shorter pulses provide a greater risk to the optics for a given laser flux, the duration of the scattered light pulse was calculated for each target size and the flux was appropriately adjusted to an equivalent flux at 5 ns.

The amount of scattered light produced from 420 micron diameter targets is above the recommended and safe amount. It may be possible to use the backlighters deemed unsafe in this project if different beams are available for use and the ports on the opposite sides of the target chamber are blocked to prevent damage from scattered light. However, this would reduce the number of beams available to irradiate the primary target.

#### **5. Acknowledgements**

I would like to thank Dr. Craxton for showing me how to work with SAGE and helping me along with my project. Also, I would like to give a big thank you to Emma Garcia for giving me advice and helping solve my computer issues.

## 6. References

1. J. Nuckolls et al., “*Laser Compression of Matter to Super-High Densities: Thermonuclear (CTR) Applications,*” *Nature* **238**, 139 (1972).
2. J.D. Lindl, “*Development of the Indirect-Drive Approach to Inertial Confinement Fusion and the Target Basis for Ignition and Gain,*” *Phys. Plasmas* **2**, 3933 (1995).
3. Y. Kong, “*Beam-Pointing Optimization for Proton Backlighting on the NIF,*” Laboratory for Laser Energetics High School Summer Research Program (2013).
4. A.M. Cok, “*Development of Polar Direct Drive Designs for Initial NIF Targets,*” Laboratory for Laser Energetics High School Summer Research Program (2006).
5. P.B. Radha et al., “*Direct Drive: Simulations and Results from the National Ignition Facility,*” to be published in *Phys. Plasmas*.
6. J.R. Rygg et al., “*A Monoenergetic Proton Backlighter for the National Ignition Facility,*” *Rev. Sci. Instrum.* **86**, 116104 (2015).
7. A.M. Cok et al., “*Polar-Drive Designs for Optimizing Neutron Yields on the National Ignition Facility,*” *Phys. Plasmas* **15**, 082705 (2008).
8. E.M. Garcia, private communication (2015).
9. B.J. MacGowan, private communication (2015).

*Optimization of Backlighter Targets Using a Saturn Ring on the National Ignition Facility*

**Jake Kinney**

Pittsford Sutherland High School

Advisor: Dr. R. S. Craxton

Laboratory for Laser Energetics

University of Rochester

February 2016

## 1. Abstract

Backlighting on the National Ignition Facility (NIF) is a process by which a primary target is irradiated by x rays or protons produced by a secondary “backlighter” target. Uniform spherical implosions of these backlighter targets are ideal to produce high-energy x rays or protons from a small point source at peak compression. In some experiments, the primary target needs to be driven by the NIF beams closest to the equator, leaving only the more polar beams (positioned at  $23.5^\circ$  and  $30.0^\circ$  from the poles) to drive the backlighter target (typically a CH shell with diameter 2 mm and thickness 20  $\mu\text{m}$ ). Given this constraint, it is very difficult to get a uniform implosion even if the beams are repointed to the equator. Using the hydrodynamics simulation code SAGE, a design was developed with a CH “Saturn ring” surrounding the target. The presence of the Saturn ring gave more drive at the target’s equator and allowed for a more uniform spherical implosion. The position of the Saturn ring as well as the beam pointings and defocus were adjusted to produce this optimized design.

## 2. Introduction

Nuclear fusion has the potential to provide the world with abundant clean, safe energy. Fusion relies on fuel found in water rather than oil or gas, and as such does not harm the environment or contribute to global warming. One method to achieve nuclear fusion is to irradiate a spherical target consisting of a glass or plastic shell surrounding cryogenic deuterium and tritium with powerful lasers. When the lasers irradiate the target, the shell ablates outward, causing an opposing force to compress the deuterium and tritium in the interior. The implosion compresses the inner layer to extreme densities. High temperature and pressure in the compressed core provides the kinetic energy needed for the positively charged deuterium and tritium to overcome Coulomb repulsion forces and fuse together.<sup>1</sup> This fusion reaction forms a

helium nucleus and an energetic neutron, which accounts for most of the energy released. The energy in the helium nucleus is redeposited in the fuel in a process known as ignition. Ignition represents the first step towards breakeven, defined as the point at which energy released by fusion is equal to the energy input from the laser. When energy output is substantially higher than energy input, it is known as high gain. High gain is necessary for laser fusion to be used as a plausible energy source.

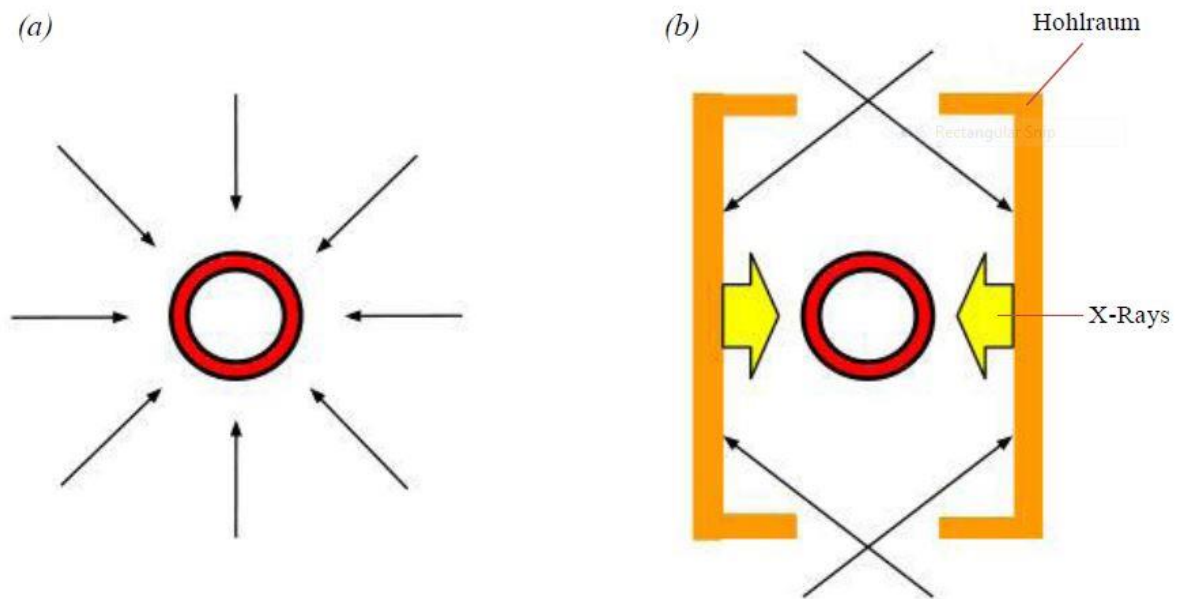


*Figure 1: The two main approaches to laser fusion. (a) Direct drive involves beams striking the target directly. (b) Indirect drive involves beams striking the inner walls of a cylindrical hohlraum, which emits x rays that then irradiate the target. (Figure 1 of Ref. 2).*

Following the description of Ref. 2, there are two main methods of conducting laser fusion, shown in Fig. 1: direct drive<sup>1</sup> and indirect drive.<sup>3</sup> In direct drive, each beam strikes the shell directly, coming in towards the target at normal incidence. The beams are arranged

symmetrically around the shell so that the shell is irradiated from all directions. The OMEGA laser at the University of Rochester's Laboratory for Laser Energetics (LLE) is configured for direct drive. In indirect drive [Fig. 1(b)], laser beams irradiate a cylindrical hohlraum made of a metal with a high atomic number (usually gold) that has been placed around the target. The beams are directed through openings at the top and bottom of the hohlraum to strike the cylinder's inner walls. The hohlraum then re-emits about 80% of the energy it absorbed as x rays, which irradiate the target. There is a significant loss in deposited energy using indirect drive: only 20% of the x rays emitted by the hohlraum are absorbed by the target. A large amount of energy is lost either in the hohlraum walls or through the openings at the ends of the hohlraum. While indirect drive represents an inefficient method of fusion because of the loss in energy, indirect drive does have the advantage of irradiating the target with good uniformity. The National Ignition Facility (NIF)<sup>4</sup> at Lawrence Livermore National Laboratory (LLNL) is configured for indirect drive.

The NIF is currently the most powerful laser in the world; it can deliver a total of 1.8 MJ to a target. It has 192 beams organized in 48 groups of 4 beams each, called "quads" (See Fig. 4 below). The quads are arranged in eight equally spaced rings around the target, with four quads making up each of the two rings closest to the north and south poles and eight quads in each of the two rings above and below the equator. The four rings in both the north and south hemispheres are aligned to strike the target at polar angles ( $\theta$ ) of 23.5°, 30.0°, 44.5°, and 50.0° from the vertical. The locations of the beams in these rings are not conducive to direct drive experiments. If the NIF beams are pointed at the center of the target (as in a direct drive experiment), the resulting implosion does not exhibit good uniformity, as the poles are drastically overdriven in comparison to the equator. In order to execute uniform direct drive

implosions on the NIF, polar drive is used.<sup>5,6</sup> Polar drive is a method in which some of the beams are repointed towards the equator of the target instead of the center of the target. Fig. 2(a) shows an implosion without beam repointing. The poles have been overdriven, resulting in a severely flattened target. As seen in Fig. 2(b), a polar drive implosion involving beam repointing leads to a more uniform spherical implosion. By depositing their energy near the equator, the repointed beams compensate for the lack of quads in the equatorial region.

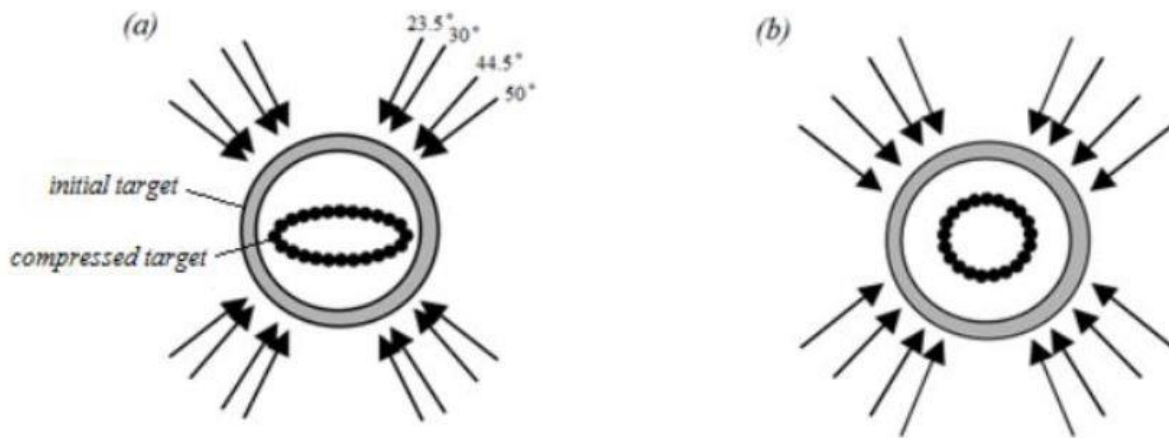


*Figure 2: Polar drive on the NIF. (a) A direct drive implosion on the NIF with the beams pointed at the center results in a nonuniformly compressed target with not enough drive at the equator. (b) Aiming beams towards the equator using polar drive results in a more uniform spherical implosion. (Figure 2 of Ref 2).*

An important use for direct drive implosions is proton or x ray backlighting, first modeled for the NIF in Ref. 2. Backlighting involves using protons or x rays generated by a backlighter target to irradiate a primary target. Due to the presence of multiple targets, two different sets of beams must irradiate each target. Since the majority of NIF beams must be used

to drive the primary target, a limited number of beams can be used to drive the backlighter target. This makes creating a uniform polar drive implosion on a backlighter target extremely difficult. A uniform implosion is desirable because it is ideal to produce a large quantity of protons or x rays emanating from a single point source.

Craxton and Jacobs-Perkins first proposed the addition of a “Saturn ring” around a polar direct drive target on the NIF, to refract beams towards the equator so that more energy will be deposited at the equator.<sup>7</sup> This counteracts the poles being overdriven compared to the equator and leads to a much more uniform spherical implosion. The purpose of this work is to improve the uniformity of backlighter target implosions by adding a Saturn ring around the target. Various parameters have been adjusted in an attempt to create optimized designs. A design has been produced that offers significantly improved spherical uniformity of a backlighter target due to the addition of a Saturn ring.

### 3. Initial Design

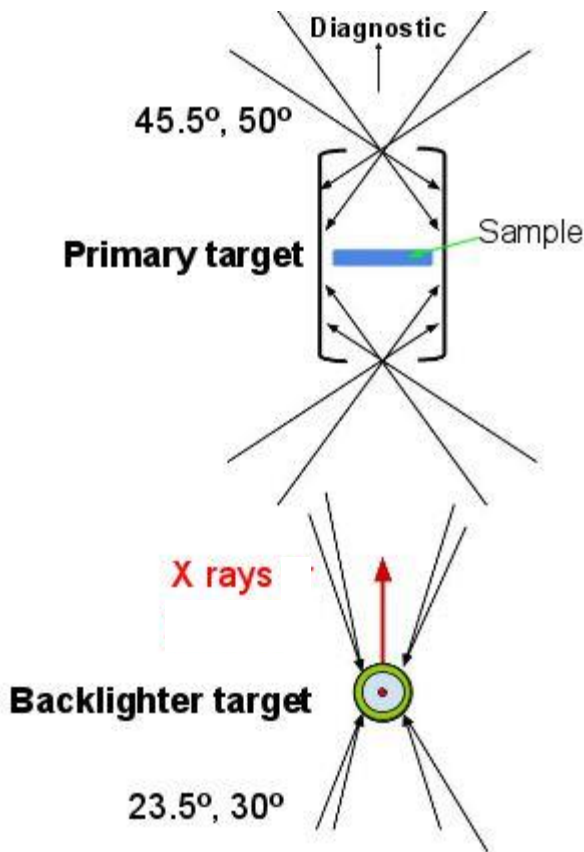
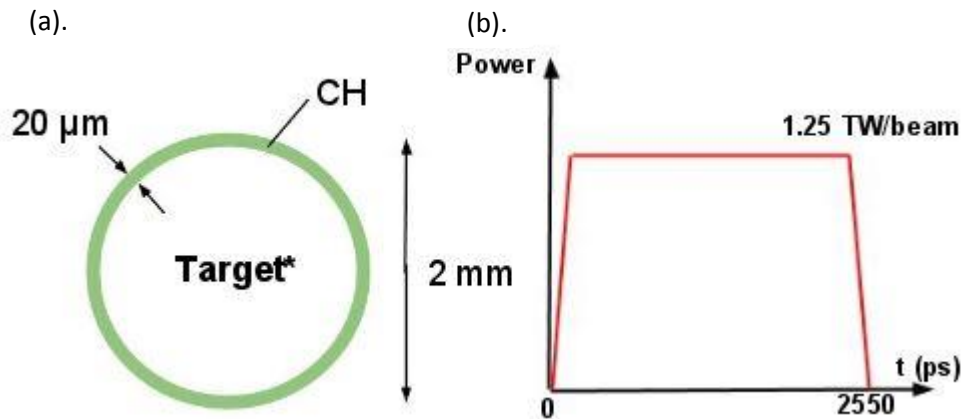


Figure 3: Setup for a backlighter experiment conducted by Heeter et al.<sup>8</sup> The backlighter target is irradiated by rings of beams at  $23.5^\circ$  and  $30^\circ$  from the poles. X rays released from the backlighter implosion pass through the hohlraum, where a primary target is heated by x rays from the hohlraum, to a diagnostic.

At LLNL, Heeter et al.<sup>8</sup> proposed and conducted an experiment on the NIF to test the concept of using a backlighter target to diagnose a primary target. The setup for Heeter's experiment is shown in Fig. 3. The rings of beams at  $44.5^\circ$  and  $50.0^\circ$  from the poles are used for the primary target. This leaves the smaller rings at  $23.5^\circ$  and  $30.0^\circ$  from the poles for the backlighter target. A total of sixteen quads are used for the backlighter, giving 64 beams to drive the target.

As shown in Fig. 4(a), the backlighter target for this NIF experiment consisted of a  $20\ \mu\text{m}$  thick CH shell with diameter 2 mm. Each beam carries a 2550 ps pulse with a maximum

power of 1.25 TW/beam [Fig. 4(b)]. These target parameters were used as the starting point for this work. Using the two-dimensional hydrodynamics code SAGE, and the beam parameters from the LLNL design, this experiment was simulated.



*Figure 4: Parameters for the backlighter design used by Heeter et al. (LLNL). (a) The backlighter target is a glass shell, 20 μm thick and 2 mm in diameter. (b) Each beam has a maximum power of 1.25 TW with a brief ramp-up time (100 ps).*

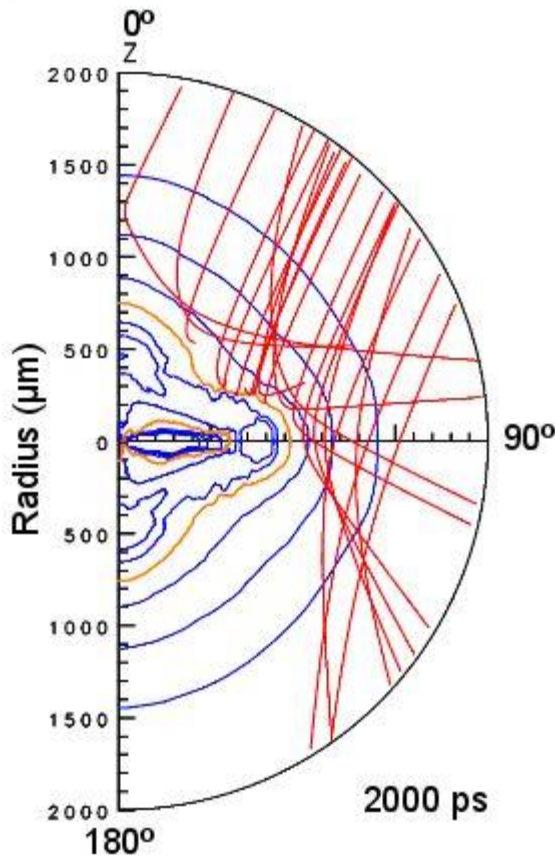


*Figure 5: Raytrace plot showing a simulation of the experiment without a Saturn ring at  $t = 2000$  ps. Red lines indicate the locations of laser rays as they refract through the target. Blue lines are mass density contours of the target. The orange line represents the critical surface beyond which laser rays cannot penetrate. At  $t = 2000$  ps, the equator is severely underdriven and the target is flattened.*

It can be seen clearly in Fig. 5 that the experiment, which did not include a Saturn ring, resulted in poor spherical uniformity. The equator is severely underdriven and the compressed target has simply been flattened. The shape of the orange line, representing the critical surface beyond which laser rays cannot penetrate, can be observed to provide a good approximation to the shape of the shell at a given time. The shell is driven most strongly at around  $45^\circ$  to the  $z$  axis.

Two important ways to measure the effectiveness of the implosion were used. The first measured the radial center of mass as a function of  $\theta$  at different times throughout the implosion. At a given angle  $\theta$  from the pole and a given time  $t$ , the center of mass of the imploding shell will be a certain distance away from the initial center of the target. Center of mass plots such as those

shown in Fig. 6 give these values across an entire hemisphere of the target, from  $\theta = 0^\circ$  (the north pole) to  $\theta = 180^\circ$  (the south pole). In Fig. 6, several of these plots, from different times of a given experiment, are superimposed. These plots provide an easy way to examine the progression of an implosion and see the uniformity. Soon after the start of the implosion, at  $t = 1000$  ps, the areas of the target between the equator and the poles have centers of mass closer to the center of the target than at the poles and especially the equator. At  $t = 2000$  ps, this disparity is much more pronounced. The equator has not been driven enough and the center of mass at the equator remains at over 0.7 mm from the center. At 2000 ps, the root mean square (RMS) deviation on the center of mass plot has a value of 16.1%. This center of mass superposition plot clearly shows the poor uniformity of the original design.

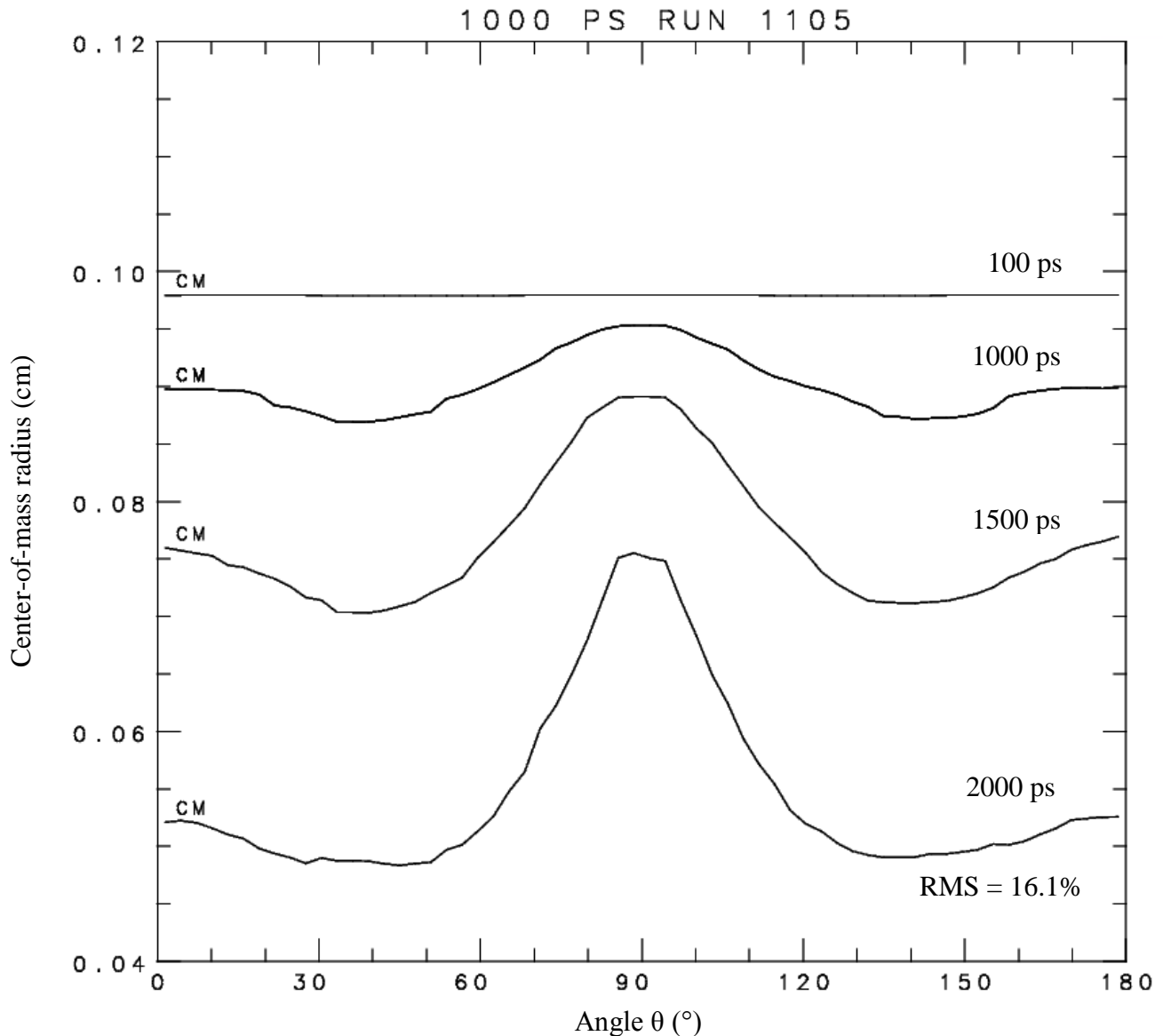
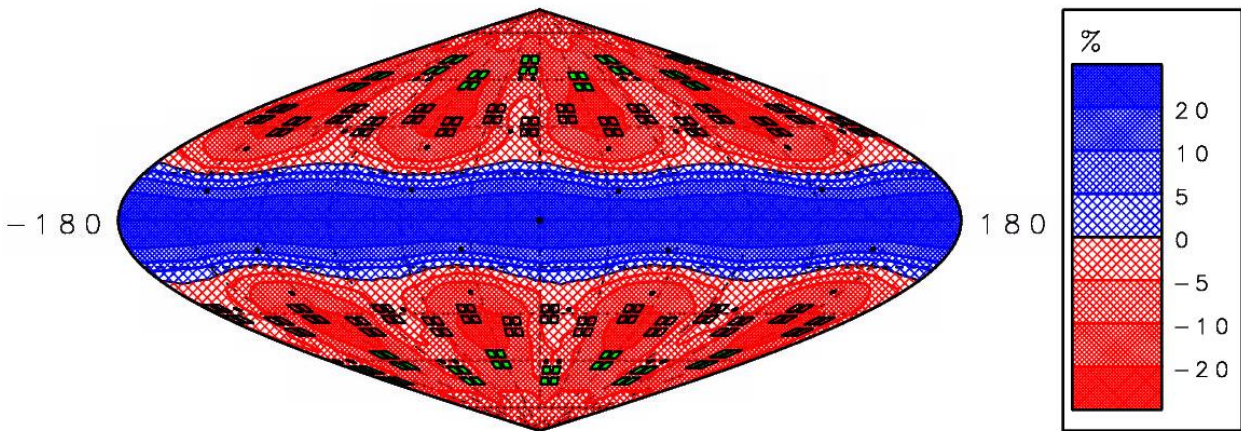


Figure 6: Center of mass radius superposition plot for Heeter’s experiment (without a Saturn ring). As the shell implodes, the equator travels far slower than the poles, leaving the shell severely underdriven around  $\theta = 90^\circ$ .

Another way to study the uniformity of a laser-driven implosion is through a contour plot, such as in Fig. 7, showing the deviation from the average center of mass radius over the whole surface of the target. Fig. 7 is a projection of the entire surface of a sphere. Red areas are

places where the center of mass is closer to the center than average, while blue areas are those where the center of mass is further from the center than average. The outlines of the NIF quads can be seen in black. The black squares shaded with green represent the quads that are used to irradiate the backlighter target. The black dots on the contour plot show where beams have been repointed. The beams were repointed to greater polar angles  $\theta$ , but this was not enough to provide adequate drive to the equator. The contour plot shows very weak drive on the equator, and the strongest drive around  $\theta = 45^\circ$ . This is consistent with Fig. 6. The contour plot shows an RMS of 32.1%. It is worth noting that the contour plots will always have a higher RMS than the center of mass plots, since they take into account differences across the horizontal angle  $\Phi$  rather than just the vertical angle  $\theta$ . These deviation values must be drastically reduced to create an effective backlighter implosion with a small source size and short flash.



*Figure 7: Contour plot of the center of mass radius at 2.0 ns for Heeter's experiment (without a Saturn ring). The blue band surrounding the equator indicates that the region has moved significantly less than average, while the red regions have moved more than average. The z axis is vertical.*

The results of this simulation demonstrated that the implosion on the NIF without a Saturn ring yielded poor spherical uniformity. The beams did not provide adequate drive on the equator and the compressed target was severely flattened instead of imploded spherically.

#### **4. Optimized Design Using a Saturn Ring**

An optimized design was developed in which a Saturn ring was placed around the equator of the target. The purpose of the Saturn ring is to fix one of the major problems with polar drive. Since, by definition, the beams do not strike the target at normal incidence, much of the energy in the beam is not deposited onto the target's surface. This can be seen in Fig. 5, where rays to the right pass through the equatorial region without depositing much energy. However, as shown in Fig. 8, the Saturn ring refracts rays of the beams so that they strike the target with a more desirable angle. As a result, more energy can be deposited at the equator, leading to a more uniform implosion.

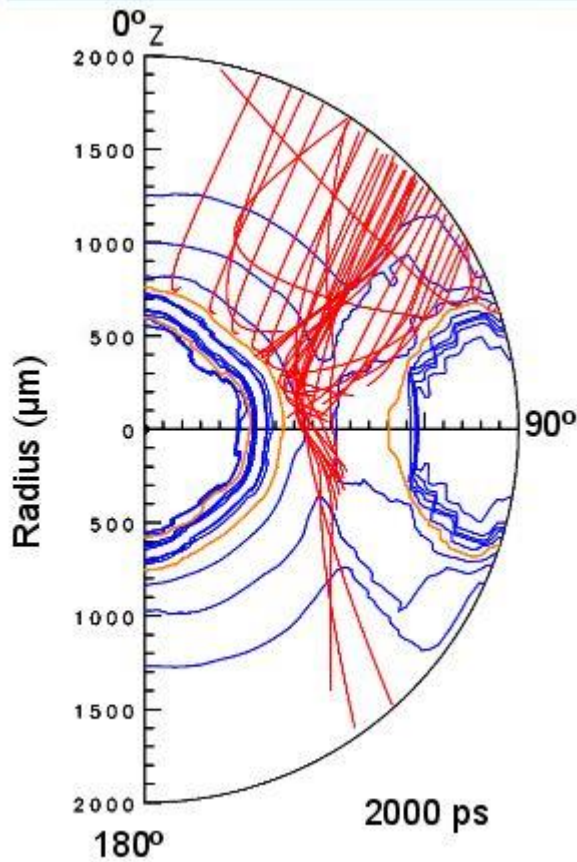


*Figure 8: Raytrace plot showing optimized design with a Saturn ring at  $t = 2000$  ps. Rays (shown in red) refract off the Saturn ring, represented by the blue mass density contours on the right side of the figure. This gives more drive to the equator, resulting in a more uniform spherical implosion.*

Many factors must be taken into account when it comes to optimizing the reaction with the Saturn ring, including shape, size, and position of the ring. The position of the ring is especially important. If the ring is too far away from the target the ring will not refract the beams at all and the beams will interact with the target as if there was no ring. In contrast, if the ring is too close to the target, a phenomenon known as shadowing can occur. The ring will completely obscure the equatorial region from the incoming beams and prevent any of the beams' energy from being deposited on the equator. An intermediate distance must therefore be found that does not lead to either of these problems. Experimentation determined that a radial distance from the surface of the target to the ring of  $400 \mu\text{m}$  was optimal. The shape of the Saturn ring was also varied. The final design took the shape of an irregular pentagon. The flat face on the interior of

the ring, opposite the surface, allows the ring to be placed close enough to the target to effectively refract incoming beams towards the target while not blocking the equatorial region of the target and causing shadowing. It should be noted that the variations explored in the shape of the Saturn ring were by no means comprehensive, and further research should be conducted to further optimize the shape of the ring.

Variations were made in the setup parameters including beam pointing and beam defocus. Each beam in a given quad can be repointed to a different spot on the target's surface through  $\theta$ -shifts and  $\Phi$ -shifts. By repointing beams, the deposited energy can be spread over the entire surface of the target, providing drive everywhere and leading to a uniform implosion. Beam repointings can have a profound impact on the effectiveness of an implosion. For the optimized design, one beam in each of the quads used was pointed to  $\theta = 30^\circ$  from the pole and the remaining three beams in each quad were pointed to  $\theta = 80^\circ$  from the pole.

Because each beam is focused onto the target through a lens, there is a point for every beam that represents the point of best focus. The "defocus" of a beam refers to the distance away from the point of best focus that the target is placed. The larger the defocus of a beam, the larger the area over which its energy is deposited. Defocusing beams has the advantage of depositing energy over a wider area, which is desirable for a uniform spherical implosion; however, there is a tradeoff. Greater defocus means lower overall deposited energy, resulting in a less efficient implosion. The optimum defocus distance was found to be 1.5 cm.

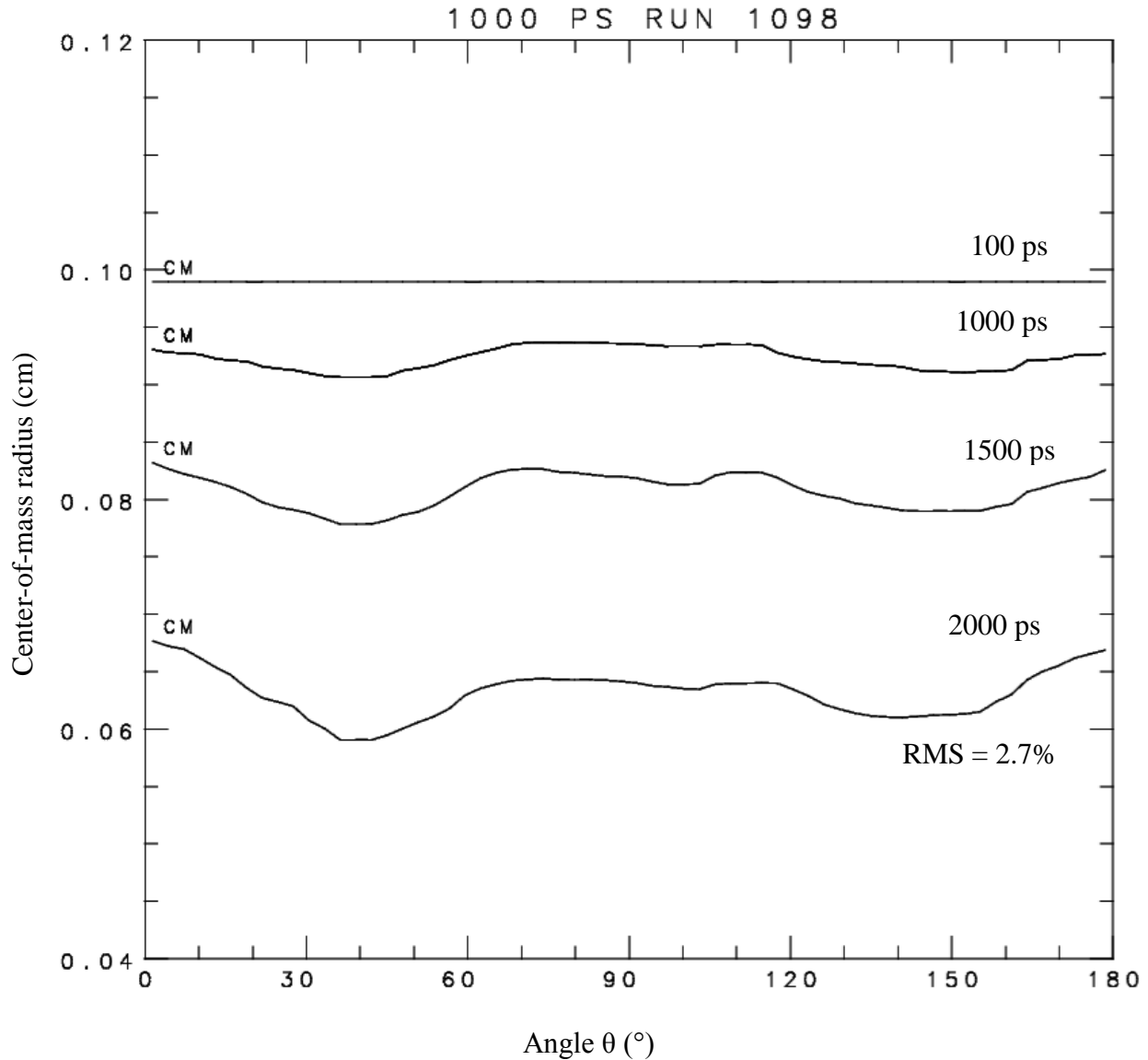
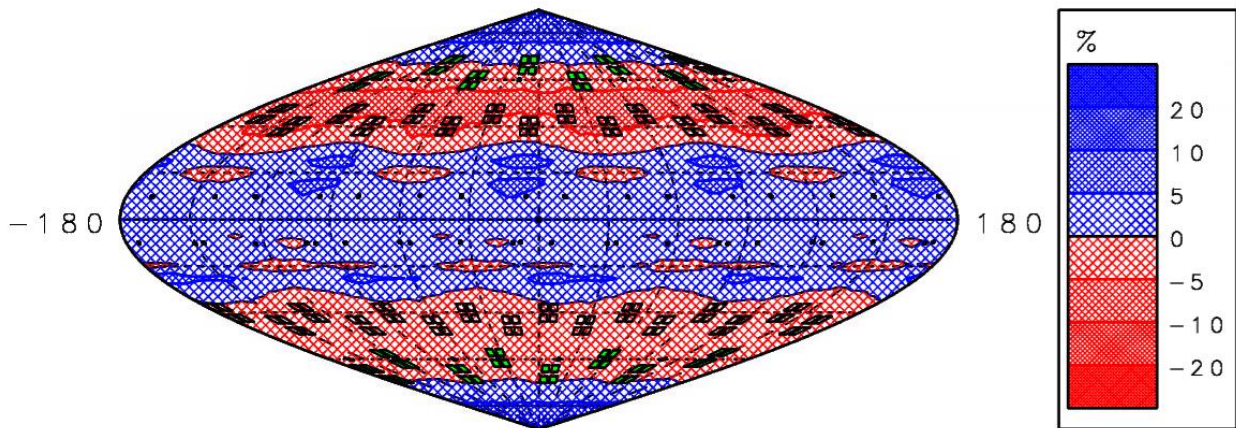


Figure 9: Center of mass radius superposition plot for the optimized design using a Saturn ring. The graph remains much more flat as the surface of the target implodes than in the case without a Saturn ring (Fig. 6). The plot clearly indicates that adding a Saturn ring led to a more uniform implosion.

The optimized design with a Saturn ring produced far greater uniformity than the original design. Center-of-mass radius plots (Fig. 9) for the optimized simulation show an RMS of 2.7%

at 2000 ps, down from 16.1% for the original design. It can be seen in Fig. 9 that the areas at  $45^\circ$  and  $135^\circ$  are still slightly overdriven, and the poles and the equator less so; however, this difference is clearly much more minor than in the original design without the Saturn ring. The flatter center of mass lines in Fig. 9 are indicative of the higher degree of uniformity that results from the addition of the Saturn ring.



*Figure 10: Contour plot of the center of mass radius for the optimized design with a Saturn ring. The lack of darker regions illustrates a more uniform center of mass distribution.*

A contour plot of the center of mass radius for the optimized design, seen in Fig. 10, shows similar improvements, yielding an RMS of 3.4% at 2000 ps, down from 32.1% for the original design. On the optimized design, the poles are slightly above average in terms of center of mass radius, evidenced by the blue color around the poles. The equatorial region is also slightly above average. However, there are few darker regions, indicating that there is less deviation from the average center of mass radius. It can also be seen in Fig. 10 that  $\Phi$ -shifts were added to the beams, demonstrated by the black dots that represent where the beams have been repointed to. These horizontal shifts further improve the uniformity of the implosion. The addition of the Saturn ring gave the equator more drive, producing a near-uniform implosion.

## 5. Scattered Light on the National Ignition Facility

Another advantage provided by adding a Saturn ring to a polar drive backlighter target on the NIF is limiting the amount of scattered light. Scattered light refers to laser rays that do not deposit their energy on the target, but instead go past the target and pass through beam ports on the other side of the target chamber. If these laser rays have enough energy, they can damage the final mirrors in the infrared part of the laser. It is thus desirable to limit the amount of scattered light. It can be seen in the raytrace plot for the experiment without the Saturn ring (Fig. 5) that rays on the edge of the beam pass through low mass densities only, so they do not deposit much of their energy; they are also not refracted very much so they go near the poles. In Fig. 8, the raytrace plot of the Saturn ring experiment, laser rays on the edge of the beam have been blocked and absorbed by the Saturn ring. This reduces the amount of scattered light.

Figures 11 and 12 show contour plots of scattered light for the simulations without the Saturn ring (Fig. 11) and with the Saturn ring (Fig. 12). The red regions represent areas with higher scattered light levels, while the blue regions are areas with less significant scattered light. Regions without significant scattered light have been left unshaded. Fig. 11 shows that scattered light is concentrated at the poles, while the equatorial region does not have much scattered light. With the addition of the Saturn ring, scattered light is still predominantly at the poles, but it is significantly less (as seen in Fig. 12). With the Saturn ring, the equator has no significant scattered light.

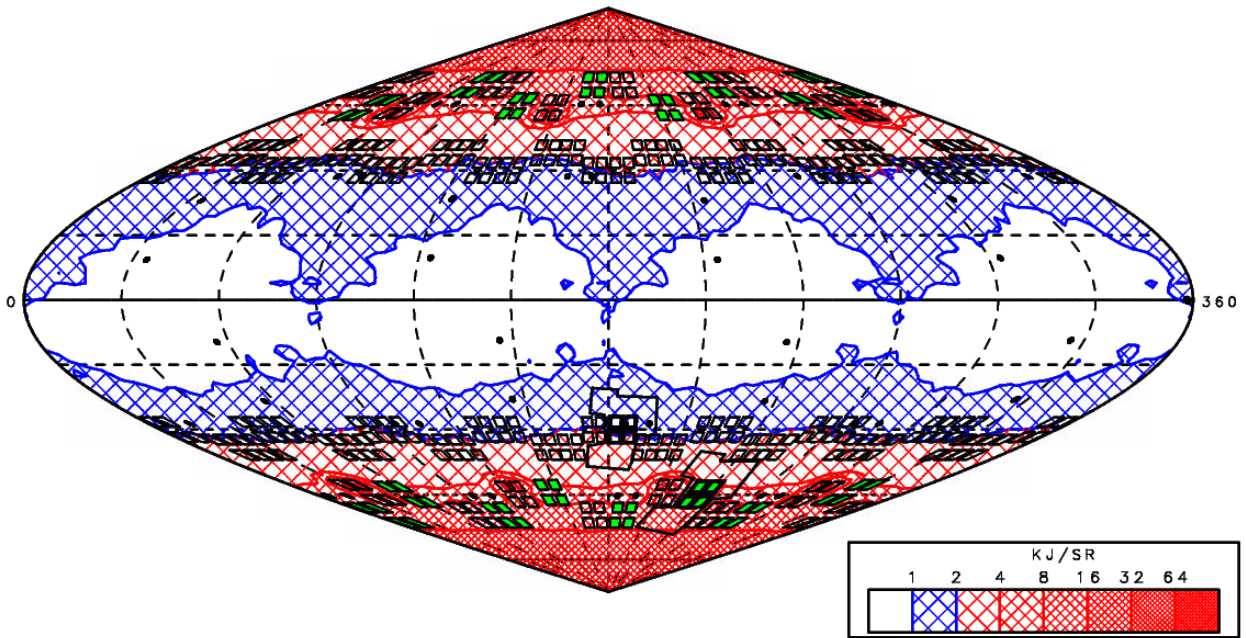
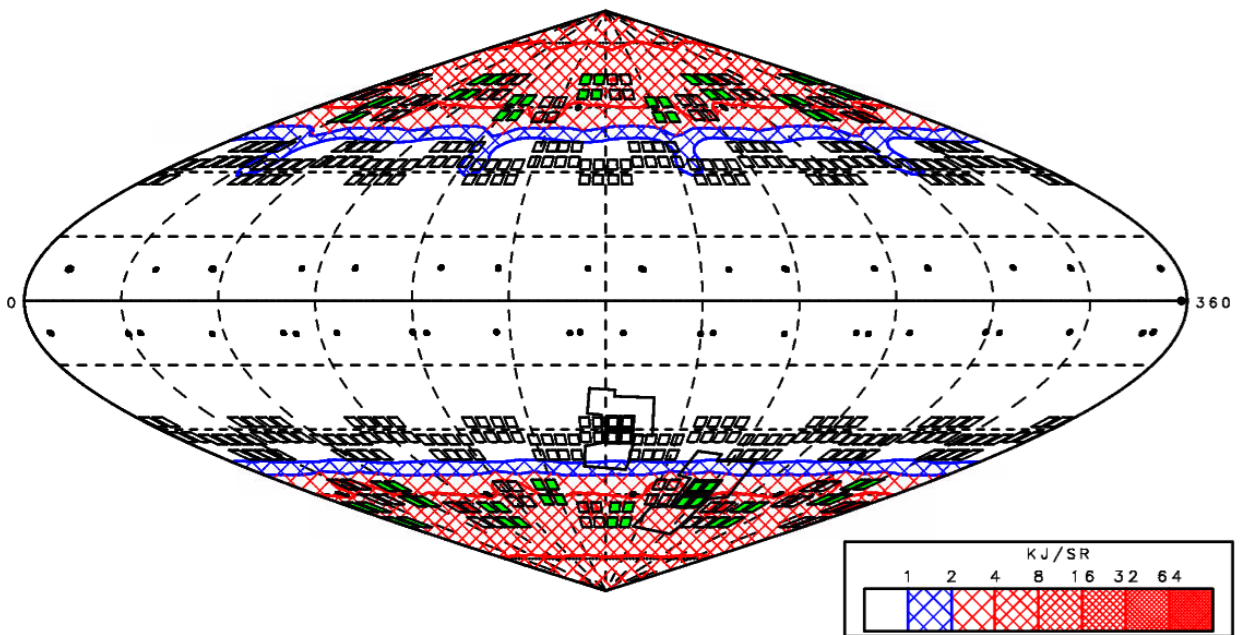


Figure 11: Scattered light on the original design without the Saturn ring. Colored regions indicate levels of scattered light, with red regions representing the highest amount of scattered light detected. The maximum flux is 22.5 kJ/sr.



*Figure 12: Scattered light on the optimized design with a Saturn ring. The level of measured scattered light is drastically reduced, with the maximum flux 9.0 kJ/sr.*

Without the Saturn ring, the highest level of scattered light measured had a peak value of 22.5 kJ/sr. The addition of the Saturn ring lowered this value to 9.0 kJ/sr. The presence of a Saturn ring has clear positive effects on scattered light levels. It should be noted that even the value of 22.5 kJ/sr is considered small and does not pose a problem for experiments with a 2-mm diameter target.

## **6. Simulations of Smaller Targets**

Implosions of smaller targets with diameter 866  $\mu\text{m}$  were also simulated, also irradiated just with beams in the 23.5° and 30° rings. The addition of a Saturn ring produced limited improvement in uniformity. Center of mass radius plots had an RMS of 7.9% at 600 ps in a simulation with a Saturn ring, as compared to an RMS value of 14.7% at 600 ps in a simulation without the ring. While the addition of a Saturn ring did not greatly improve the spherical uniformity of implosions, the presence of the ring drastically reduced the scattered light. The peak scattered light for the simulation with the Saturn ring was 2.8 kJ/sr, while without the ring the peak scattered light had a value of 81 kJ/sr. It is possible that a scattered light level of 81 kJ/sr could have detrimental effects on the laser optics.

## **7. Conclusion**

A design has been developed for a polar drive backlighter target on the National Ignition Facility that uses the addition of a Saturn ring around the target to greatly improve the uniformity of the implosion of the target. The design applies to a specific geometry wherein only rings of beams at 23.5° and 30° from the poles can be used. The presence of the Saturn ring gave lower

RMS deviations of the center of mass radius. A simulation with the Saturn ring produced an RMS value of 3.4%, while the original design without the Saturn ring yielded an RMS value of 32.1%. In addition, the presence of the Saturn ring limited the amount of scattered light produced in the implosion. Designs were also studied for smaller targets, but the addition of a Saturn ring did not greatly improve the uniformity of the implosion. However, the presence of the ring drastically reduced the amount of scattered light on the smaller targets.

## 8. Acknowledgements

I would like to thank Dr. Craxton for his consistent and incredibly helpful advice and feedback throughout this process, as well as for running the High School Program. I would like to thank the Laboratory for Laser Energetics for the wonderful opportunity to take part in the High School Program; it has been a rewarding and informative experience in scientific research.

## References

- 
1. J. Nuckolls et al., "*Laser Compression of Matter to Super-High Densities: Thermonuclear (CTR) Applications*," *Nature* 239, 139 (1972).
  2. Yifan Kong, "*Beam-Pointing Optimization for Proton Backlighting on the NIF*," Laboratory for Laser Energetics High School Summer Research Program (2013).
  3. J. Lindl, "*Development of the Indirect-Drive Approach to Inertial Confinement Fusion and the Target Physics Basis for Ignition and Gain*," *Phys. Plasmas* 2, 11 (1995).
  4. C. A. Haynam et al., "*National Ignition Facility Laser Performance Status*," *Applied Optics* 46, 16 (2007).
  5. S. Skupsky et al., "*Polar Direct Drive on the National Ignition Facility*," *Phys. Plasmas* 11, 5 (2004).

6. R. S. Craxton et al., “*Polar Direct Drive: Proof-of-principle Experiments on OMEGA and Prospects for Ignition on the National Ignition Facility*,” Phys. Plasmas 12, 056304 (2005).
7. R. S. Craxton and D. W. Jacobs-Perkins, “*The Saturn Target for Polar Direct Drive on the National Ignition Facility*,” Phys Rev. Lett. 94, 095002 (2005).
8. R. F. Heeter, Lawrence Livermore National Laboratory, private communication.

A Web-based Interface for Collaborative Multi-User Data  
Analysis in a Scientific Research Environment

**Nathan Knauf**

The Harley School

Brighton, NY

Advisor: Richard Kidder

**Laboratory for Laser Energetics**

University of Rochester

Rochester, NY

January 2016

## 1. Abstract

A web-based interface was developed for scientific data analysis that allows data to be intuitively viewed and interpreted in a collaborative online environment. The interface improves the ability of scientists and engineers to analyze and compare results from different experiments and diagnostic types. It allows users to quickly view and investigate laser shot results without the need to manually download or manipulate data for specialized routines and to analyze shot results with both preexisting and user-written Python routines. The interface was demonstrated using data from experiments on the OMEGA and OMEGA EP lasers. The work also provides a framework for future networked utilities in which users both on and off site could collaboratively analyze data in web-based live sessions.

## 2. Introduction

At LLE, many diagnostic systems are in place on both the OMEGA and OMEGA EP laser systems for use during laser shots. Principal Investigators (PIs) require access to the data from these diagnostics to better understand the results of their experiments. Currently, there is a page on the LLE website, illustrated in **Figure 1**, through which PIs can search for laser shots on the basis of their shot identification numbers, view logistical information about the shots, and download data files from the different diagnostics used in the shots. The current page is not designed to pair PIs with data from their own experiments, instead relying entirely on a search function that finds shots on the basis of their identification number, so PIs must recover these numbers from physical records outside of the website in order to access their data. When PIs view the diagnostic data from a laser shot, they are presented with basic summary information and preview images of the data, but the PIs are ultimately limited in their usage of this data, because they cannot access any

information beyond a few summary statistics of each diagnostic, they cannot compare data between multiple diagnostics, and in some cases they cannot even preview the entire data set from a single diagnostic.

OMEGA Shot  
Images and Reports

[Query Page](#)  
[Omega Home Page](#)

---

**Search Options**

**Single Query:**

For    go to

---

**Multiple Query:**

For   to  go to   [Advanced Search](#)

---

**General Shot Summary  
for Shots 78444 - 78453**

Color Legend  
 System Shot  Trigger Tests  System Aborts

[Previous 20 Shots -->](#)

Shot	Date	Shot Type	RID	Campaign	Target ID(s)	# of PCUs	
<a href="#">78453</a>	25-Aug-2015 13:48:38	Target High Yield	<a href="#">53879</a>	LBS	ISE-3Q15-02-22	215	<a href="#">Download Images</a>
<a href="#">78452</a>	25-Aug-2015 12:27:14	Target High Yield	<a href="#">53878</a>	LBS	ISE-3Q15-02-15	215	<a href="#">Download Images</a>
<a href="#">78451</a>	25-Aug-2015 11:35:20	Target High Yield	<a href="#">53867</a>	LBS	ISE-4Q15-01-05	215	<a href="#">Download Images</a>
<a href="#">78450</a>	25-Aug-2015 11:23:54	Target Low Yield	<a href="#">50349</a>	Other	PCRYO_ANY	0	<a href="#">Download Images</a>
<a href="#">78449</a>	25-Aug-2015 10:40:47	Target High Yield	<a href="#">53865</a>	LBS	ISE-4Q15-01-04	215	<a href="#">Download Images</a>
<a href="#">78448</a>	25-Aug-2015 09:37:47	Target High Yield	<a href="#">53864</a>	LBS	ISE-4Q15-01-02	215	<a href="#">Download Images</a>
<a href="#">78447</a>	25-Aug-2015 09:23:12	Non-Prop				1	<a href="#">Download Images</a>
<a href="#">78446</a>	25-Aug-2015 08:52:42	Target High Yield	<a href="#">53841</a>	LBS	ISE-4Q15-01-01	215	<a href="#">Download Images</a>
<a href="#">78445</a>	25-Aug-2015 08:40:25	Non-Prop				0	<a href="#">Download Images</a>
<a href="#">78444</a>	25-Aug-2015 08:28:39	Non-Prop				213	<a href="#">Download Images</a>

[User Feedback](#)  
[Previous 20 Shots -->](#)

Figure 1: The current LLE search page, where PIs can look up laser shot records by their Shot ID numbers

In this research, a new, streamlined, and user-friendly interface was designed and developed for PIs to access and interpret all of their data on the website both intuitively and efficiently. Existing information from the records of laser shots about which PIs are associated with each shot was incorporated into the new web page so that when PIs use the web page, they are immediately presented with shots they are associated with so that they do not have to rely on external records of laser shot numbers to find their data. PIs may search for laser shots on the basis of which other PIs worked on them and also on the basis of shot identification number, just as in the original interface. The new interface implements new web-based technologies so that PIs can interact with the data and its component layers in a more thorough manner. Most importantly, the

new web page allows PIs to perform detailed analysis within their browser, with both a wide assortment of pre-made analysis routines and the ability to write and execute custom Python<sup>1</sup> code, which is of special value to both external and internal PIs who may need to work with their data from a computer that is not equipped with specialized analysis software.

### **3. Development**

The layout and design of the new interface were made as intuitive and usable as possible, while remaining consistent with the aesthetic and organization of the rest of the LLE website. Work was done to implement a system that would run user-selected data analysis routines on data on the LLE servers, display both the data and analysis results on the user's computer in an efficient and convenient manner, and allow users to write their own custom Python analysis algorithms for a more adaptable analysis.

Python scripts were used on LLE's servers to process shot data according to user input independent of the computing power of the user's workstation. Thanks to its free, open-source, high-level, and easy to use nature, Python has established itself as a widely popular language among the scientific community. Since it is so universally known as well as structurally similar to many other common high-level languages (such as MatLab, Mathematica, Ruby, etc.), Python was determined to be the best suited for use in the software.

Different graphics libraries were considered to allow the shot data and analysis output to be viewed in interactive JavaScript widgets on the analysis page. After investigating Bokeh, MPLD3,<sup>2</sup> and a custom HTML5 framework, MPLD3 was chosen for its lightweight nature and smaller processing power need, which allowed it to perform well on users' possibly less powerful personal workstations or laptops as well as on specialized and powerful lab computers.

Different open-source Python notebook projects, such as Sage and Jupyter<sup>3</sup> (previously known as IPython), were investigated to allow users to write and execute code in Python inside of a web browser so as to run custom analysis routines on their shot data. Jupyter was determined to be the optimal notebook framework, as it supported over fifty other languages besides Python, had a much larger and more active development team, and had recently received a large research grant of \$6,000,000 to continue its development.<sup>3</sup>

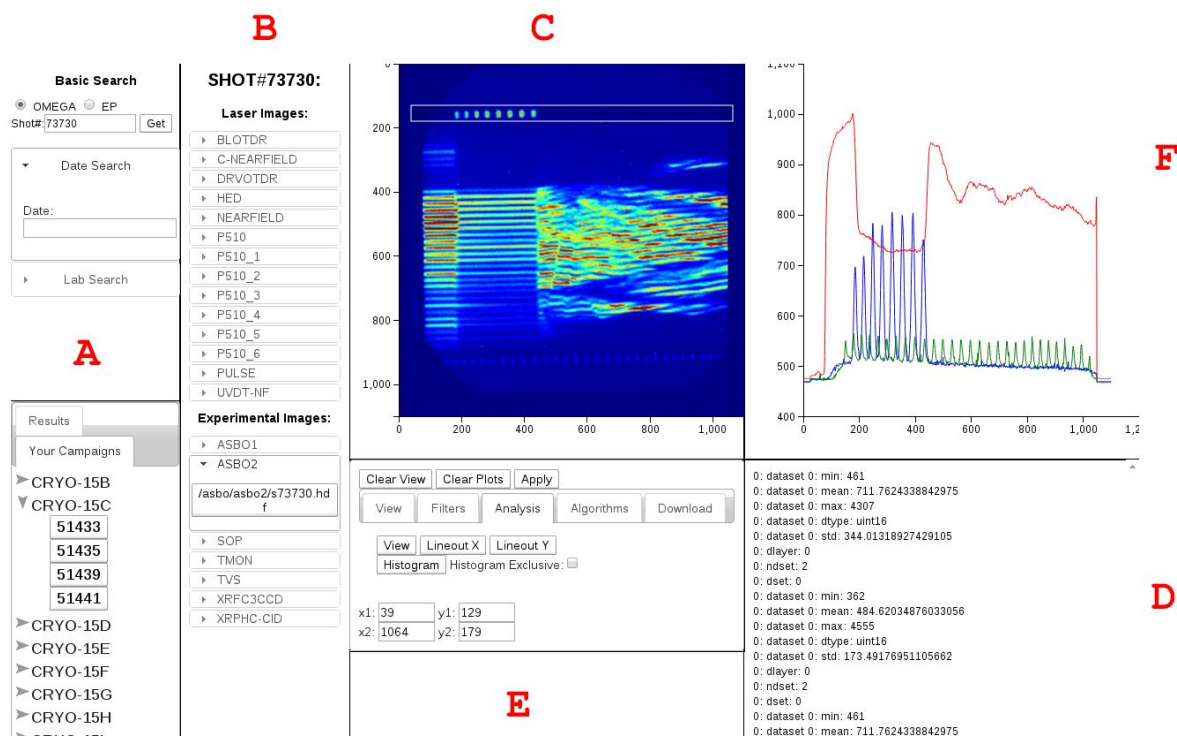


Figure 2: The Diagnostic Analysis page developed in this research, where PIs can search for, review, and analyze shot data

#### 4. New Interface Capabilities

The new interface is centered on the new Diagnostic Analysis page shown in Figure 2. This page was designed so that PIs are immediately presented with data records from campaigns and laser shots they are associated with. PIs also have access to a search functionality, depicted in Section A of Figure 2, which allows them to search for different laser shots based on shot identification numbers, the dates the shots occurred, and the laboratories and researchers

associated with the shot. Once they have selected a laser shot, PIs are shown a list of all diagnostics utilized in the shot and all the data files created from the shot, depicted in Section B of **Figure 2**.

Upon the selection of any data file, the analysis page sends an asynchronous JavaScript (AJAX) request to the LLE web server, with identifying information about the diagnostic the PI wishes to view. After verifying that the user has permissions to view the diagnostic data, the web server pulls the data files (generally in .HDF and .DAT formats) from the shot records and uses Python and MPLD3 routines to create a .JSON file containing the diagnostic data and necessary information about how the data should be viewed, such as the type of the data, the dimensions of the dataset, or whether it should be interpreted as a line graph or an image. After the .JSON file is sent back to the client analysis page, it is interpreted by the MPLD3 JavaScript package to create an interactive JavaScript widget on the page, depicted in Section C of **Figure 2**, through which PIs can scale, transform, and view the data in detail. Summary information and details about the .JSON file are printed in a log depicted in Section D of **Figure 2**.

On the page, depicted in Section E of **Figure 2**, are a variety of settings for how the diagnostic data is to be viewed. PIs can manipulate these settings to view the data in different ways, such as by viewing different layers and datasets, by entering coordinates to designate which regions of the data to view, by changing the color map used to represent the data as images, by selecting the level of quality used to render data images, or by stretching, shrinking, or rotating data images. When PIs alter any of these view settings, new AJAX requests are sent from the analysis page to the web server, and the web server replies with .JSON files containing the appropriate selections and interpretations of data.

Alongside the view settings, also depicted in Section E of **Figure 2**, PIs have access to an array of analysis options for their data and are able to view the output from their chosen analysis

routines in a secondary graph widget, depicted in Section F of **Figure 2**, so that they can view their interpreted data in comparison with the original data. PIs can use the interactive JavaScript widget holding the diagnostic data to intuitively drag selection boxes around regions of interest in the diagnostic data, automatically calculating appropriate coordinates and designating these regions for analysis. PIs are then able to analyze their data in a variety of ways, by viewing histograms and distributions of the values of a data file, by exploring the differences in values between the layers and datasets of a multi-dimensional data file, and by producing specialized graphs of regions of interest such as images with data values normalized or averaged over the horizontal or vertical axes. Also in Section E of **Figure 2** are tools to download the images and plots of both the original and output data, with options for graph format and scale.

A significant advantage of this new interface is that PIs are able to view data from multiple diagnostics as well as from different shots simultaneously in order to quickly visualize the differences between diagnostic datasets. **Figure 3** depicts four datasets being plotted individually in the old interface on the left, but together in the new interface on the right, showing how the new interface can make data visualizations more meaningful by allowing PIs to view data in the context of other data.

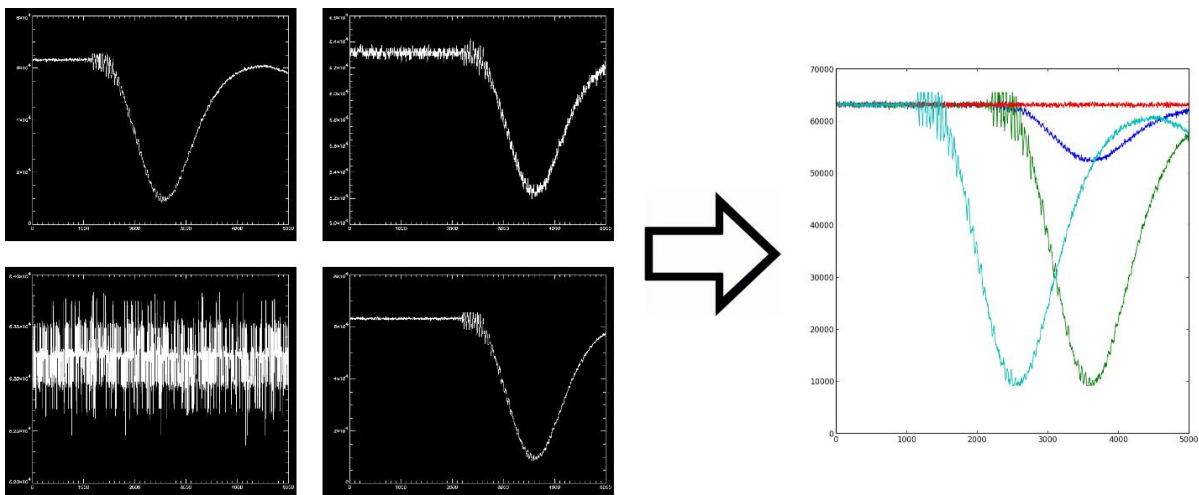


*Figure 2: Multiple datasets viewed simultaneously in the new interface*

As well as having access to a large number of predefined analysis routines, PIs now have the ability to write their own custom routines, in Python and other languages, through the newly implemented Jupyter notebooks on the LLE server. PIs are able to create notebook files in their own secure directories, where they can write and execute code in their browser to analyze diagnostic data in further depth and specialization than is possible in the analysis page, as well as use the text editing features of the notebook to accompany their mathematical interpretations of the data with written explanations of their methods. PIs may export their notebooks as HTML files or upload them to GitHub, an industry standard free source code repository, so that other researchers, scientists, and colleagues may view the PIs' work in a collaborative online environment, where they can assist PIs by sharing and discussing their experimental and analytical techniques.

**Figure 4** shows an example of a Jupyter notebook being used to analyze shot data. **Figure 4** depicts a portion towards the end of a longer notebook of Python code that analyzes a shot data file from the LLE server, specifically from a P510 Diagnostic that records data in the form of an image of parallel streak lines. The full code breaks the image down into different regions containing the distinct streak lines and then plots distinct curves, one for each streak line, depicting the sum of values along the vertical columns of data in each region of the image. Through this kind of analysis, a PI might observe the differences between the streak lines, such as variations in intensities, lengths, or timings. Since code written in the Jupyter notebooks is processed by LLE servers, the use of Jupyter Notebooks allows PIs to use custom code to pursue detailed analysis of their data from their personal workstations or laptops, which might not have enough processing power to run the analysis code locally.

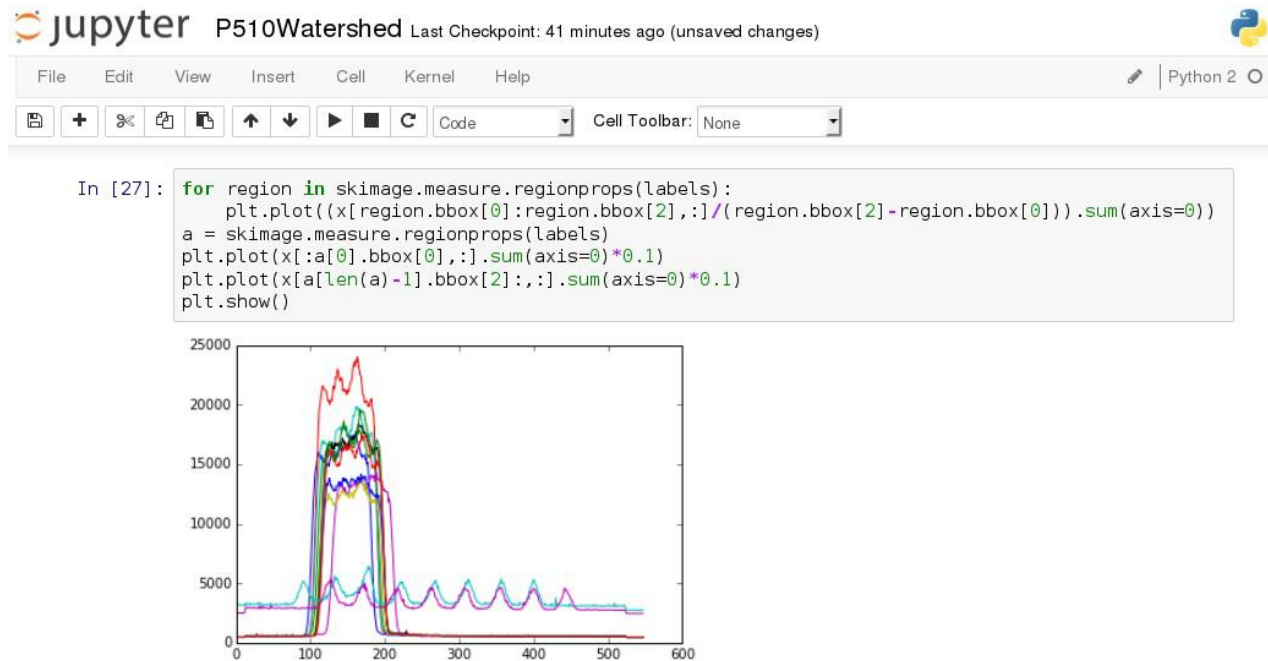


Figure 5: An example of a graph from a Jupyter Notebook being utilized to display lineouts from P150 streak data

## 5. Future Plans

In earlier work by Smith,<sup>4</sup> an online tool was researched and developed to view experimental and diagnostic configurations of the OMEGA laser system. This work demonstrated the feasibility and benefits of web-based live sessions, in which PIs can work on the same configuration simultaneously in a collaborative online environment. In the future, this research can be implemented into both the Diagnostic Analysis page and the Jupyter notebook pages to allow PIs from different laboratories to more effectively communicate and to collaboratively analyze data from laser shots in the OMEGA and OMEGA EP systems.

The analysis page can also be expanded to include further features, such as a custom graphic interface, the ability to directly compare data values between different diagnostic data files by subtracting or overlapping their data, and a larger selection of specialized analysis routines designed for specific diagnostics.

## **6. Conclusion**

A new web-based interface has been developed to allow PIs to analyze diagnostic data from laser shots on the OMEGA and OMEGA EP laser systems. New analytical tools have made the workflow of PIs significantly more efficient by providing a streamlined and intuitive user interface. The new tools are advantageous to PIs because they allow diagnostic data to be viewed quickly and intuitively, they facilitate the comparison and interpretation of data from different diagnostics and shots, and they provide an online environment in which PIs can collaborate and easily share their findings. The new interface serves as a basis for future tools and software to allow LLE scientists as well as researchers from around the world to work efficiently and collaboratively in online environments.

## **7. Acknowledgements**

This research could not have been accomplished without the assistance of Mr. Richard Kidder, my advisor, who guided the overall direction of the project while giving me the opportunity to research and develop the new analysis tools independently. I also received significant support from my coworkers, Andrew Zeller and Michael Charissis, who helped me to investigate the current technologies in use at LLE and to implement the newly developed tools into the existing LLE website. Without Dr. Stephen Craxton's hard work managing and advocating LLE's Summer Research Program for High School Juniors, none of this research would have been possible.

## 8. References

1. “Python” Python Software Foundation. Web. Jan 2016.  
<https://www.python.org/>
2. “MPLD3” MPLD3 Developers. Web. Jan 2016.  
<http://mpld3.github.io/>
3. “Jupyter” Project Jupyter. Web. Jan 2016.  
<http://jupyter.org/>
4. Liam Smith, “Evaluation of a Collaborative Networking Environment for Experimental Configurations” Laboratory for Laser Energetics High School Summer Research Program (2014).

*Design of an Imaging Telescope with Variable Magnification and  
Imaging Distance*

**Eileen Norris**

Brighton High School  
1150 Winton Road, Rochester, NY

Advisor: Dr. Seung-Whan Bahk

Laboratory for Laser Energetics  
University of Rochester, Rochester, NY

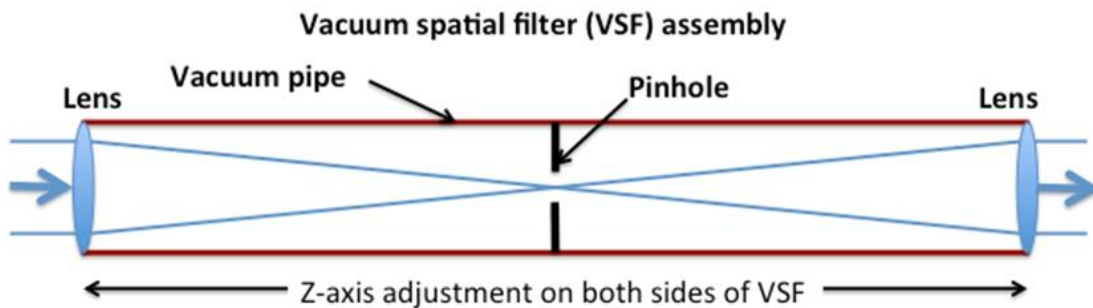
March 2016

**Abstract**

Vacuum spatial filters, used to control beam quality and remove unwanted high spatial frequency noise from amplified beam pulses, mostly rely on two-lens imaging telescopes with no flexibility in magnification and imaging distance unless the lenses themselves are replaced. New three-lens and four-lens imaging telescopes facilitate adjustable beam magnification and imaging distance by altering only lens positions. Systems of ray matrices were constructed for three-lens and four-lens systems. This formalism determines the required adjustments of lens positions and can be used to predict and analyze beam magnification and imaging distance. Constraints, primarily fixed positions of lenses that are not moved, were set to maximize the convenience of the lens systems, confirming that for a range of magnification, not all lenses need to be moved when optimized initial focal lengths are used. A more detailed ray tracing program was created to model the new designs, verifying ray matrix calculations and revealing a peak-to-valley wave front error of typically 0.02 to 0.05 waves. Experimentally tested three-lens systems presented magnifications with a maximum deviation of 2.3% from the calculated values, confirming the calculations.

## I. Introduction

Vacuum spatial filters are used frequently at the Laboratory for Laser Energetics (LLE) to relay system image planes and remove unwanted high spatial frequency noise from amplified pulses. Figure 1 shows a common vacuum spatial filter assembly. Prior to this work, vacuum spatial filters at LLE have relied primarily on two-lens imaging telescopes. While the collimation of the beam can be adjusted with small shifts in lens positions, the magnification and imaging distance of these two-lens systems can only be changed by altering the focal lengths of the lenses, and therefore replacing the lenses themselves.




---

**Figure 1:** Schematic of a spatial filter. A pinhole is used to remove high spatial frequency noise from the amplified pulses and the lenses are adjusted along the z-axis to maintain beam collimation.<sup>1</sup>

---

New three-lens and four-lens imaging telescope designs, however, facilitate adjustable beam magnification and imaging distance by altering only lens positions. This report describes the use of ray matrix formalism and experimental setups to determine and verify a three-lens optical system enabling variable magnification and imaging distance.

## II. Three-Lens System

First, we produced a three-lens design [Figure 2]. Based on the ray matrix formalism shown in Sec. III, the position of the first lens (F1) is fixed in this design with the distance labeled D1

also fixed. Fixing the first lens position provides the advantage of fixing the location of the spatial-filtering pinhole. While the positions of F2 and F3 are adjustable within the system, the total length of the system ( $L = D1+D2+D3+D4$ ) can be set for a given system, but once set, is immutable for the remainder of the calculations for that system. The plane on the left of Fig. 2 is imaged onto the plane on the right.

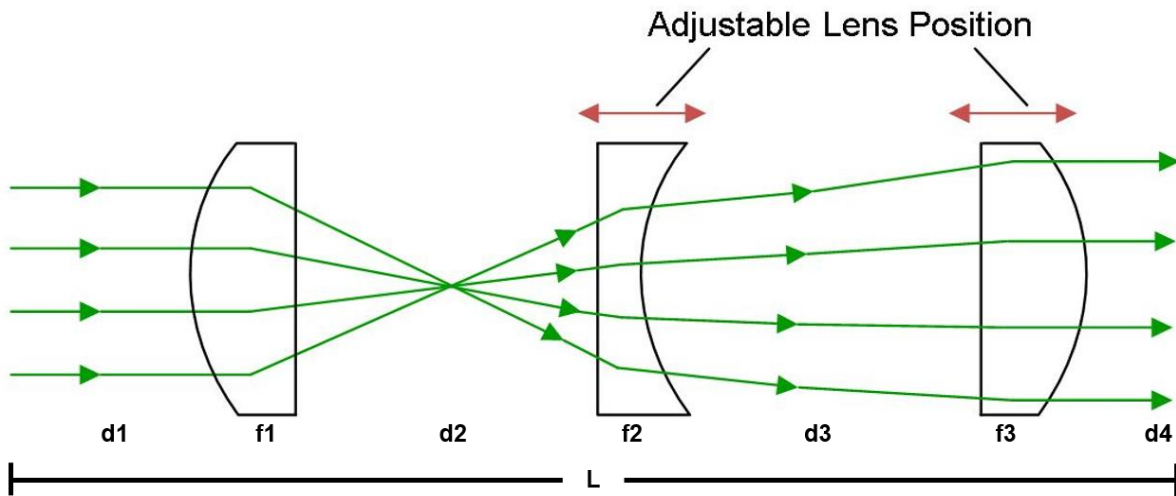


**Figure 2:** Schematic of the propagation of a beam through the proposed three-lens system. The first lens, F1, is fixed, and F2 and F3 are adjustable. The total length of the system, L, is also fixed. The ray paths are shown schematically; in reality the ray paths are refracted outward by the center lens F2.

As in conventional laser-beam imaging systems, the system is designed to be comprised of plano convex and plano concave lenses. The first and third lenses, F1 and F3, are plano convex, and the center lens is plano concave. Due to anticipated lab constraints, the positions of the lenses in the system were optimized for a specific set of lens focal lengths.

### III. Ray Matrix Formalism

Lens systems can be modeled with paraxial ray matrix formalism and a more comprehensive three-dimensional ray tracing model. A paraxial ray can be defined as a ray which is close enough to the optical axis of a system that sines of angles between the rays and the optical

axis may be replaced by the angles themselves in calculations. The change in position and inclination of a paraxial ray through an optical system can be represented by paraxial ray matrices.<sup>2</sup> For this experiment, the behavior of an optical ray can be separated into two scenarios: through free space and through a thin lens. The propagation of an optical ray in free space is given by

$$\begin{pmatrix} r' \\ \theta' \end{pmatrix} = \begin{pmatrix} 1 & d \\ 0 & 1 \end{pmatrix} \begin{pmatrix} r \\ \theta \end{pmatrix}, \quad (1)$$

where  $d$  is the distance the ray is traveling through free space,  $r$  and  $r'$  are the initial and final distances of the ray from the optical axis, respectively, and  $\theta$  and  $\theta'$  are the initial and final angles of the ray with respect to the optical axis, respectively.

The propagation of an optical ray through a thin lens is given by

$$\begin{pmatrix} r' \\ \theta' \end{pmatrix} = \begin{pmatrix} 1 & 0 \\ -1/f & 1 \end{pmatrix} \begin{pmatrix} r \\ \theta \end{pmatrix}, \quad (2)$$

where  $f$  is the focal length of the lens and  $r$  [ $r'$ ] and  $\theta$  [ $\theta'$ ] are the same parameters used in Eq. (1). It should be noted that we used the thin lens approximation for each lens in the system in our initial ray matrix calculations. This approximation ignores the optical effects associated with finite lens thicknesses and therefore simplifies ray tracing calculations. In reality, the lenses used to model and construct the three- and four-lens systems are 2-3 mm in center thickness. This thickness is considered in the more complex ray tracing program as described in Sec. IV.

Ray transfer matrices can be multiplied together in sequence to obtain an overall ray transfer matrix for the optical system – lens and free-space components together. It is important to note that this matrix multiplication is not commutative, so the matrices must be ordered according

to the setup of the optical system. Thus, the behavior of a ray through an optical system of both lens and free space components can be given by

$$\begin{pmatrix} r' \\ \theta' \end{pmatrix} = \begin{pmatrix} A & B \\ C & D \end{pmatrix} \begin{pmatrix} r \\ \theta \end{pmatrix}, \quad (3)$$

where the matrix [A, B, C, D] is the product of matrices describing the individual components of the optical system. By the rules of matrix multiplication, we know that

$$r' = Ar + B\theta \quad (4)$$

The imaging condition set on the optical system states that the displacement of the ray through the optical system from the optical axis does not vary with the initial angle  $\theta$  (i.e. all rays from a point in the object plane pass through the same point in the image plane), requiring  $B = 0$  because  $r'$  is independent of  $\theta$ .

Through matrix multiplication, we also know that

$$\theta' = Cr + D\theta \quad (5)$$

The collimation condition set on the optical system states that the angle  $\theta'$  of the optical ray is independent of the displacement of the ray. If the beam enters the system collimated – that is, the ray bundles are all parallel – it will exit the system collimated. Therefore,  $C = 0$ .

When the beam is collimated and imaged, the ratio of beam sizes ( $r'/r$ ) or the ratio of angular divergences ( $\theta/\theta'$ ) is the magnification of the system. From Eqs. (4) and (5), we infer that

$$A = \frac{1}{D} = M < 0, \quad (6)$$

where  $M$  is the magnification, which is negative because the image is reversed.

Assuming these three conditions, ray matrix algebra can be easily performed in Mathematica. The free space and thin lens components can be multiplied in sequence to obtain the

overall ray transfer matrix for the optical system. This ray transfer matrix, accepted imaging and collimation conditions, and controlled focal lengths and total system length can be used to solve the distances at which the three lenses in the system are located versus the desired magnification of the system. Eqs. (7) – (17) represent ray matrix algebra performed in Mathematica. First, the propagation of a lens through free space and a thin lens, as seen in Eqs. (1) and (2), is defined by

$$\mathbf{D}_{\text{Free}} = \begin{pmatrix} 1 & d \\ 0 & 1 \end{pmatrix} \quad (7)$$

$$\mathbf{D}_{\text{Lens}} = \begin{pmatrix} 1 & 0 \\ -1/f & 1 \end{pmatrix} \quad (8)$$

The overall ray transfer matrix was then calculated by multiplying the individual components of the three-lens system in respective order, given by

$$\mathbf{D}_{\text{Free}}[D4] \cdot \mathbf{D}_{\text{Lens}}[F3] \cdot \mathbf{D}_{\text{Free}}[D3] \cdot \mathbf{D}_{\text{Lens}}[F2] \cdot \mathbf{D}_{\text{Free}}[D2] \cdot \mathbf{D}_{\text{Lens}}[F1] \cdot \mathbf{D}_{\text{Free}}[D1] = \begin{pmatrix} A & B \\ C & D \end{pmatrix} \quad (9)$$

Assuming the conditions given in Eqs. (4) – (6), a system of equations was written, stating

$$A = M \quad (10)$$

$$B = 0 \quad (11)$$

$$C = 0 \quad (12)$$

$$D1 + D2 + D3 + D4 = L \quad (13)$$

This system of equations, and the previously defined overall ray transfer matrix in Eq. (9), were used to solve for D1, D2, D3, and D4, with respect to the focal lengths (F1, F2, and F3), magnification (M), and total length of the system (L). D1, D2, D3, and D4 are given by

$$D1 = \frac{F2^2 F3^2 + F1^2 F2 F3 M + 2 F1 F2^2 F3 M + 2 F1 F2 F3^2 M - F1 F2 F3 L M + F1^2 F2^2 M^2 + F1^2 F3^2 M^2 + F1^2 F2 F3 M^3}{F1 F2 F3 (-M + M^3)} \quad (14)$$

$$D2 = \frac{F1F3 + F2F3 + F1F2M}{F3} \quad (15)$$

$$D3 = \frac{F2F3 + F1F2M + F1F3M}{F1M} \quad (16)$$

$$D4 = \frac{-F1F2F3^2 - F1^2F3^2M - F2^2F3^2M - 2F1^2F2F3M^2 - 2F1F2^2F3M^2 - F1F2F3^2M^2 + F1F2F3LM^2 - F1^2F2^2M^3}{F1F2F3(-1+M^2)} \quad (17)$$

Once the positions of the lenses were related to the focal lengths, magnification, and length of the optical system, specific focal lengths and the desired length of the system could be entered, therefore leaving lens position as a function of magnification. We then graphed lens positions versus the magnification [Figure 3].

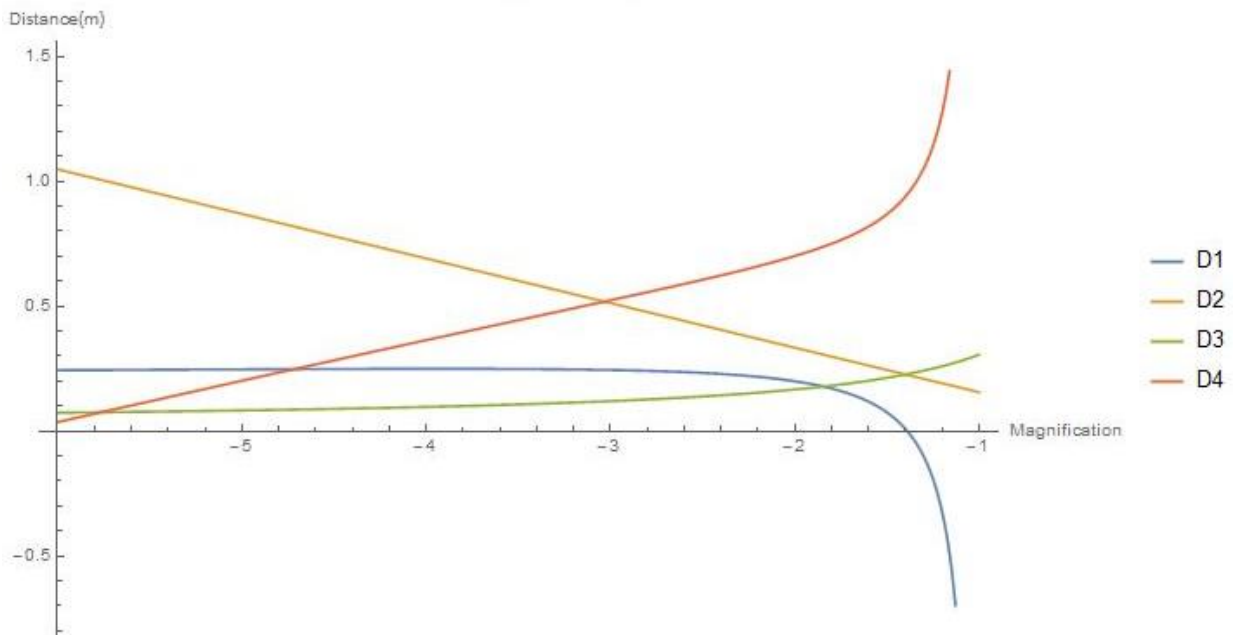


**Figure 3:** Graph of lens position (D1, D2, D3, D4) versus magnification.  $F1 = 200$  mm,  $F2 = -223$  mm,  $F3 = 250$  mm,  $L = 1.4$  m. Note that the graph of D1 is relatively flat across a wide range of magnifications while the graphs of D2, D3, and D4 are more variable.

Because the graph of D1 is relatively flat, we determined that D1 can be set at a constant position, as shown in the three-lens design of Fig 2. In the case of Figure 3, for  $F1 = 200$  mm,  $F2 = -223$  mm,  $F3 = 250$  mm, and  $L = 1.4$  m, the first lens (F1) can be set at a constant position of

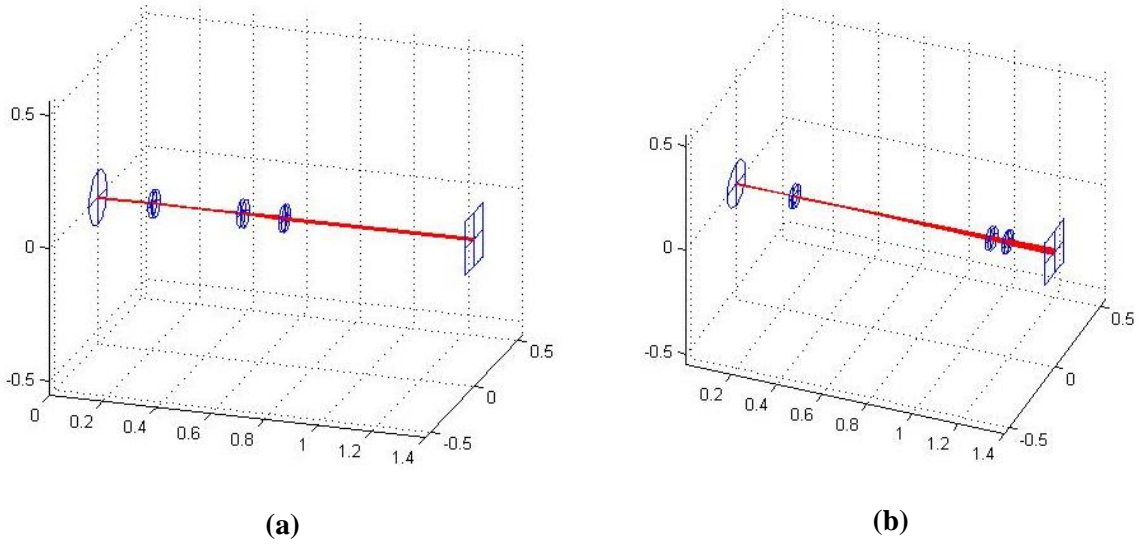
approximately 0.25 m. For different sets of focal lengths and total lengths of the system, the graph of  $D_1$  remains relatively flat over a wide range of magnifications. The three-lens design therefore functions for a range of lens focal lengths and desired total lengths.

#### **IV. Ray-Tracing Simulations**

After solving for the distances between the lenses as a function of magnification and showing that  $D_1$  can be set at a constant value, a more complex program was written based on a MATLAB ray tracing code package.<sup>3</sup> This package allows modeling of the realistic aspects of the experiment such as the center thickness of the lenses (the thin lens approximation was used in the initial calculations), the material of the lenses – primarily fused silica and BK7 – and the aperture size and the radii of curvature of the lenses.

The equations obtained by Mathematica for the lens positions [Eqs. (14) – (17)] were transferred into the MATLAB ray tracing program, which further analyzed the beam's behavior through the three-lens system. This MATLAB ray tracing program performs three dimensional ray tracing including lens material and thickness. The distances found in Mathematica were transferred as the distances between the first surfaces of each optical element in the system.

A detector plane placed at the end of the optical system in the program enables further analysis of the wavefront and beam distribution at the end of the system. Our program gives three primary outputs: three-dimensional traces of the optical rays through the system, wavefront at the detector plane, and distribution of the beam rays on the detector plane.<sup>3</sup> Figures 4(a) and 4(b) show the propagation of the rays through the three-lens system for two magnifications.




---

**Figure 4(a):** Propagation of a ray through a three-lens system with magnification  $-2$ . F1 is located at a distance  $D1$ ,  $0.247$  m from the initial reference plane on the left.  $F1 = 200$  mm,  $F2 = -223$  mm, and  $F3 = 250$  mm. The total length of the system ( $L$ ) is  $1.4$  meters.

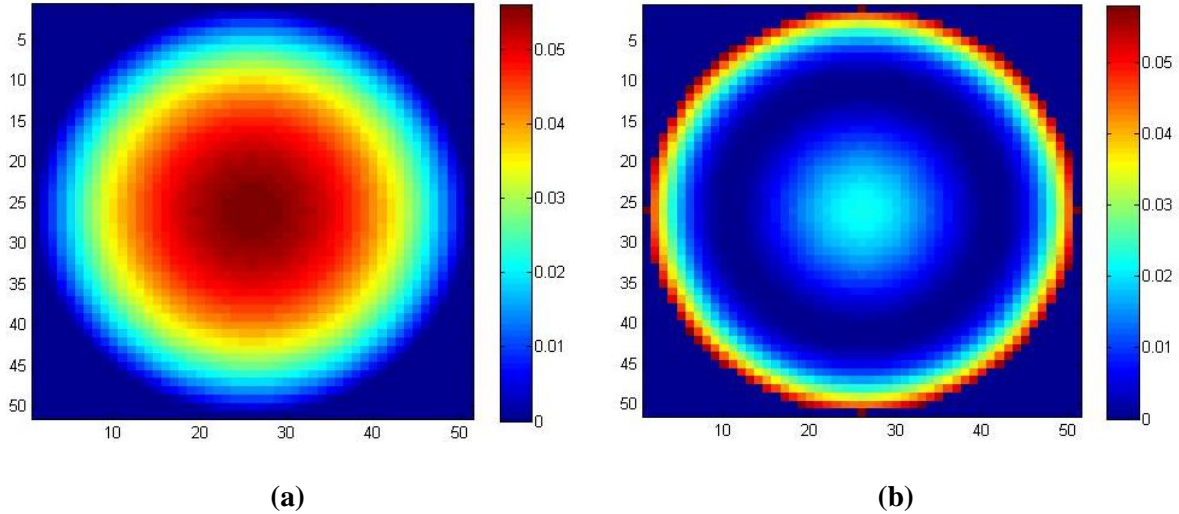
---

**Figure 4(b):** Same as Figure 4(a) except with a magnification of  $-5$ . Note that the position of F1 remains the same, with  $D1 = 0.247$  m, and the total length of the system remains at  $1.4$  m. The change in magnification is enabled by the shifting in position of F2 and F3.

---

The MATLAB model of the propagation of a beam through the three-lens system confirms that F1 can be held in a relatively constant position. As seen in Figs. 4(a) and 4(b), over a wide range of magnifications, the distance of F1 from the reference plane remains the same. Therefore, for a given total length of the system and preset focal lengths of the lenses, the positions of the second and third lenses, F2 and F3, can change the magnification achieved by the system.

The MATLAB program, however, was used primarily to verify small wavefront error as the rays exit the system. Figs. 5(a) and 5(b) show the wavefront of the beam at the detector plane located at the end of the three-lens system for the two cases shown in Fig. 4.




---

**Figure 5(a):** Wavefront of the beam at the detector plate through a three-lens system with magnification -2. Shown on the scale to the right, the maximum wavefront error is 0.05 waves.

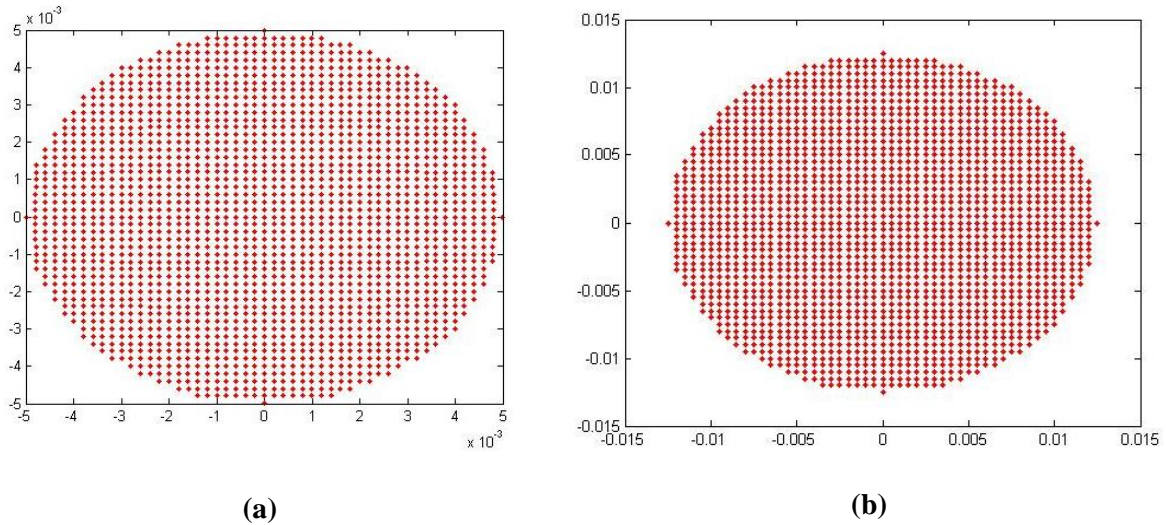
---

**Figure 5(b):** Same as Figure 5(a) except with a magnification of -5.

---

The peak-to-valley (p-v) wavefront error, the maximum displacement, measured in waves, of the actual wavefront from the desired flat wavefront, in both positive and negative directions, is 0.05 in both cases shown in Fig. 5(a) and 5(b). A perfect lens or lens system is one that produces a wavefront with no aberrations, and therefore a zero p-v wavefront error. We use the Maréchal criterion<sup>4</sup> to set the upper limit on the acceptable wavefront error. This criterion sets the level of degradation of peak intensity of the imaged focal spot caused by the wavefront error to be within 20%. The corresponding allowable p-v wavefront error for a circularly symmetric system, in this case the spherical aberration, is less than 0.11 waves p-v. The typical wavefront error for the calculations performed in MATLAB is between 0.02 and 0.05 waves, confirming the acceptability of our three-lens design.

Figures 6(a) and 6(b) indicate the distribution of the beam rays across the detector plane.




---

**Figure 6(a):** Distribution of the beam on the detector plane through a three-lens system with magnification -2 and initial beam size 5 mm. The vertical and horizontal axes are shown in meters.

---

**Figure 6(b):** Same as Figure 6(a) except with a magnification of -5. Note that the scale changes.

---

Distributions of the beams on the detector planes were used to confirm the magnification by comparing the beam sizes before and after passing through the three-lens system.

## V. Experimental Verification

While the MATLAB ray tracing program is confirmed to give theoretically accurate lens positions, it is important to confirm that it parallels the behavior of a beam through our three-lens system accurately. The three-lens system modeled in the ray tracing program is easily transferrable into an experimental setup. Figure 7 shows the lab setup used to verify the accuracy of the MATLAB ray tracing program.

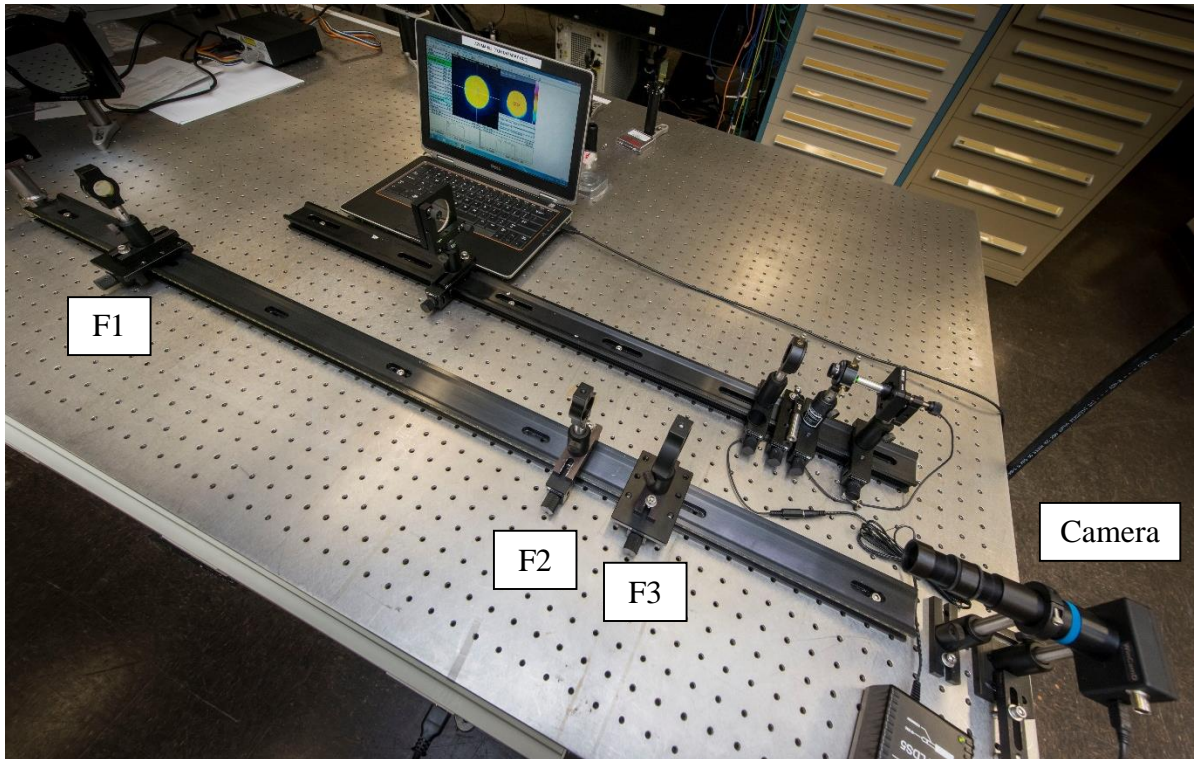
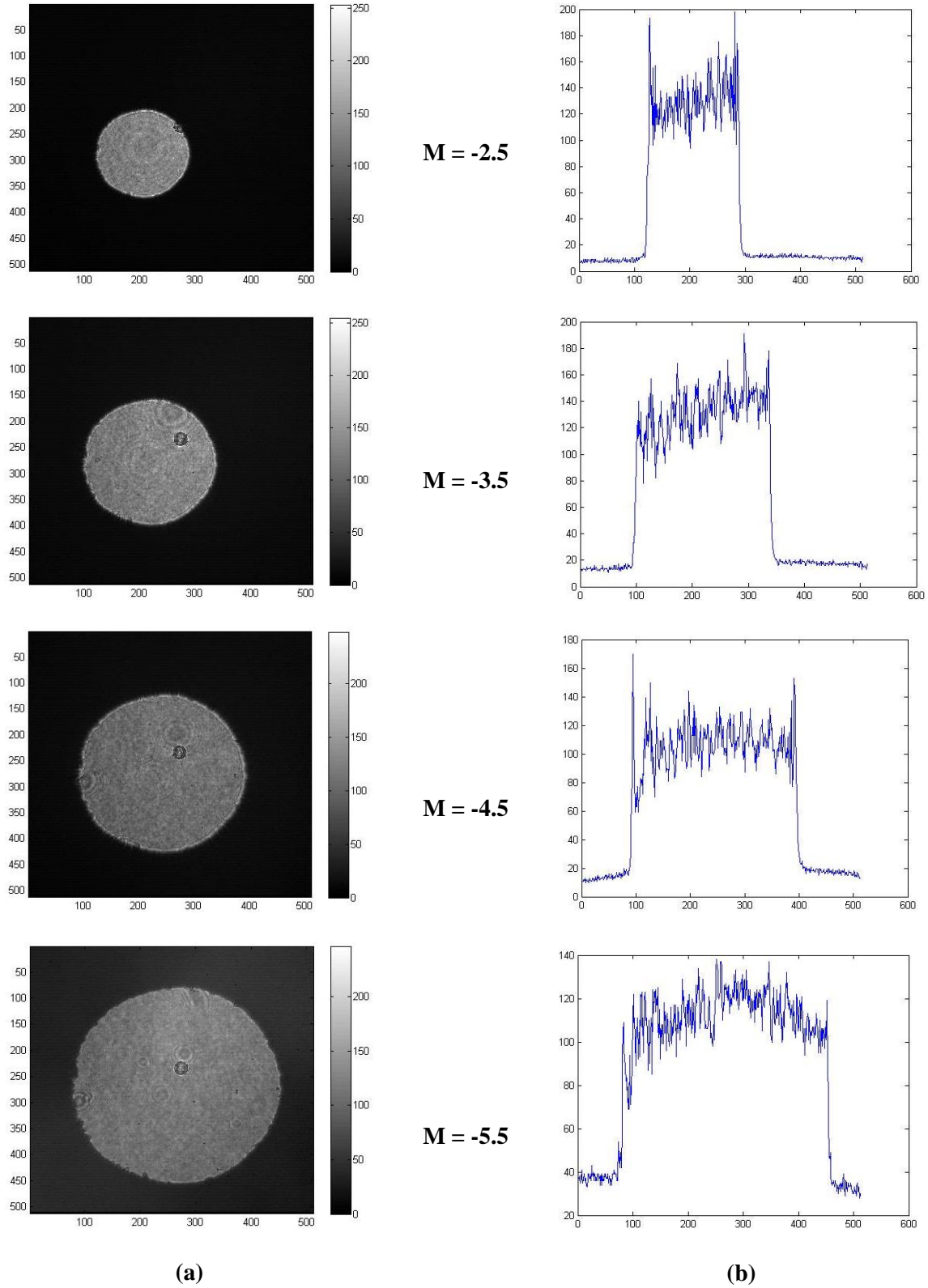


**Figure 7:** Lab setup of the three-lens system. The second and third lenses are on adjustable sliders. The system totals 1.4 m in length; however, note that due to table room constraints, the beam is bent in order to fit the system. The photo is taken by Eugene Kowaluk.

Limits exist in lens availability. Theoretically, based on the results of the MATLAB ray tracing program, the three-lens system will work with a wide range of focal lengths, providing that F1 and F3 are plano convex lenses, thus having positive focal lengths, and F2 is a plano concave lens with negative focal length. In this experiment,  $F1 = 200$  mm,  $F2 = -223$  mm, and  $F3 = 250$  mm, as in Fig. 4. A nominal 2-mm aperture marks the beginning of the system, and controls the initial beam size entering the three-lens system. The beam size in our experiment, as set by the aperture, was measured to be 1.986 mm. The first lens was placed in a stationary position of 0.247 m from the aperture. This value was obtained from the graph of  $D1$  in Mathematica, shown in Figure 3. Because the graph of  $D1$  is relatively flat with respect to  $M$  at a value of approximately 0.247 m, we concluded that if F1 is held stationary,  $M$  can be controlled by adjusting only the

positions of F2 and F3. Experimentally, we tested this by placing a camera at the end of the three-lens system set up in the lab. This camera parallels the detector plane programmed into the MATLAB ray tracing program. Lenses F2 and F3 were shifted into their appropriate positions for specific magnifications, as determined by the MATLAB ray tracing program. Photographs of the beam's distribution on the camera lens were taken for each desired magnification. Figure 8(a) shows the images taken across a wide range of magnifications. Figure 8(b) shows corresponding lineouts of intensity versus pixels for each magnification.




---

**Figure 8(a):** Distribution of the beam on the optical camera through a three-lens system over a range of magnifications. The initial beam size is 1.986 mm. The scale shows the beam intensity.

---

**Figure 8(b):** Corresponding lineouts of intensity versus pixels.

---

The images given in Figure 8(a) were used to confirm that the beam remains imaged as it exits the three-lens system and reaches the detection plane. If one looks closely at the images taken by the camera, the diffraction rings around the edge of the beam are minimal. A perfectly imaged beam will show no diffraction rings. However, because the rings in each of the images in Figure 8(a) can barely be seen, we can conclude that the beam was imaged adequately as it exited the system. The fact that the total image distance is maintained while varying the magnification is an important improvement over other variable magnification imaging systems. The state of output beam collimation and the residual spherical aberration in the system were not measured. This requires separate measurements of the input and output wavefronts using a wavefront sensor.

The lineouts of intensity versus pixels were used to further confirm the accuracy of the calculations made in the MATLAB ray tracing program. As shown in Figure 9, the full width at half max was taken on the graph for each magnification in order to determine the final experimental beam sizes. The experimental magnifications were calculated by relating the initial known beam size of 1.986 mm to the final

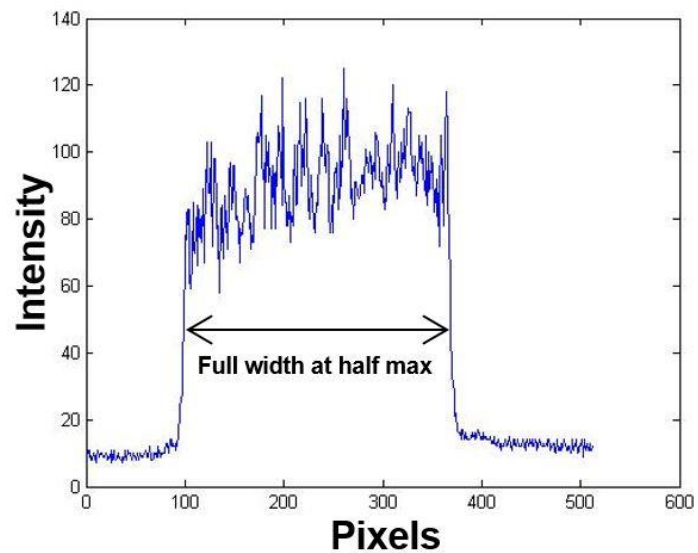


**Figure 9:** Lineout of intensity versus pixels at a magnification of -4. The full width at half max, the difference between the values of the independent variable at which the dependent variable is equal to half of its maximum value, is shown on the graph.

beam sizes determined by the full width at half max of the corresponding intensity lineout. The experimental and calculated magnifications, as well as percent deviations, are shown in Table 1.

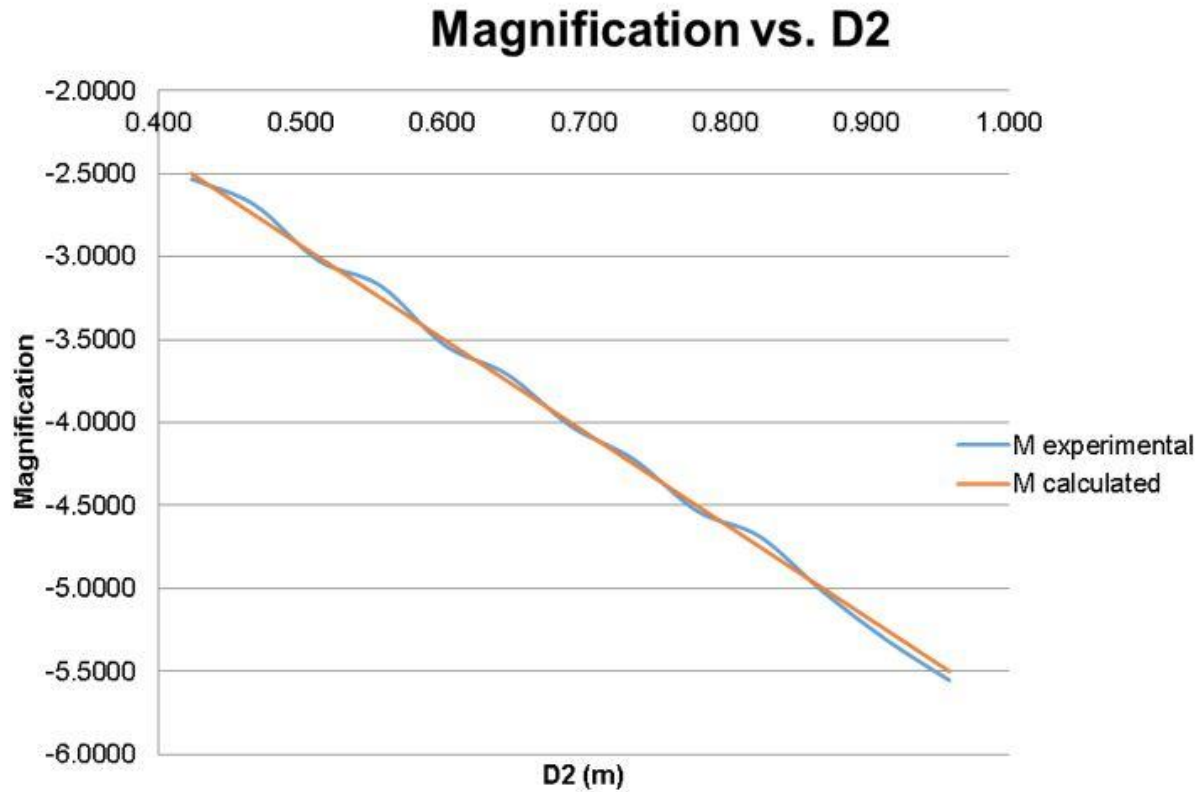
<b>M calculated</b>	<b>final beam size (mm)</b>	<b>M experimental</b>	<b>percent deviation</b>
-2.5	5.03	-2.53	1.3%
-2.75	5.34	-2.69	-2.3%
-3	6.00	-3.02	0.7%
-3.25	6.31	-3.18	-2.3%
-3.5	7.01	-3.53	0.9%
-3.75	7.37	-3.71	-1.1%
-4	7.99	-4.02	0.5%
-4.25	8.38	-4.22	-0.7%
-4.5	9.00	-4.53	0.7%
-4.75	9.31	-4.69	-1.3%
-5	9.97	-5.02	0.4%
-5.25	10.54	-5.31	1.1%
-5.5	11.03	-5.55	1.0%

---

**Table 1:** Calculated magnifications, final beam sizes, experimental magnifications, and percent deviation from the calculated magnifications. Note that the maximum percent deviation was 2.3% in magnitude.

---

Figure 10 shows the magnification as a function of D2. This variable had the widest range of values; although all of D2, D3, and D4 were adjusted to achieve varied magnifications throughout the experiment, the second lens was the most shifted lens.




---

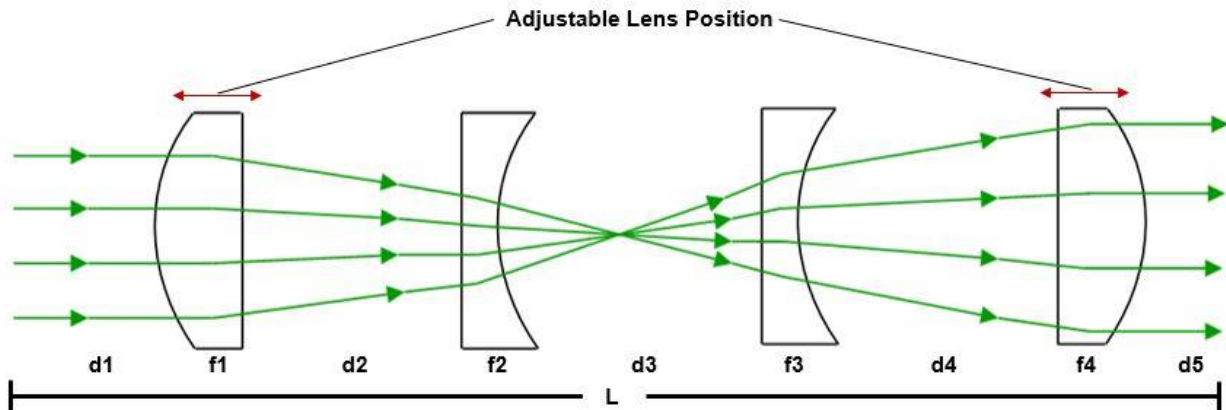
**Figure 10:** Graph of the experimental and calculated magnifications versus D2. There is little deviation of the experimental magnifications from the calculated magnifications. The maximum percent deviation is 2.3% in magnitude.

---

The comparison between the experimental and calculated magnifications was used to evaluate the accuracy of the MATLAB program in predicting the behavior of a beam through the three-lens system in a physical lab setting. With a maximum absolute error of 2.3%, we can confirm that the MATLAB ray tracing program and the equations derived in Mathematica can accurately give optimized positions for lenses in the three-lens system over a wide range of magnifications.

## VI. Four-Lens System

A four-lens system was also considered and modeled similarly using the MATLAB ray tracing program. As shown in Figure 11, the two outer lenses are fully adjustable while the inner two lenses are set at fixed positions.




---

**Figure 11:** Propagation of a beam through a four-lens system. The inner lenses,  $F_2$  and  $F_3$ , are fixed, and the outer lenses,  $F_1$  and  $F_4$ , are adjustable. The total length of the system,  $L$ , is also fixed.

---

This four-lens system can be modeled in the same way as the three-lens system. As with the three-lens system, Mathematica was used to derive equations for the positions of the two outer lenses ( $D_1$ ,  $D_2$ ,  $D_4$ , and  $D_5$ ).  $D_3$  remains constant because  $F_2$  and  $F_3$  are in fixed positions. The MATLAB ray tracing program was written to model this four-lens system at varying magnifications. Although we were unable to confirm the accuracy of these calculations experimentally, we can safely assume that, like the three-lens system, an experiment done with the four-lens system will not deviate significantly from the predictions made in MATLAB. This four-lens system enables a vacuum tube to be placed surrounding  $F_2$  and  $F_3$ , although the focal plane might shift depending on other distances. With vacuum spatial filters being commonly used in

many of the labs at LLE, this new four-lens system enables variable magnification and imaging distance by changing only the positions of two outer lenses rather than altering lens focal lengths.

## **VII. Conclusion**

Three- and four-lens image relay telescopes were designed whose magnification and total imaging distance are adjustable by changing inter-lens distances only. Each optical system includes two adjustable-position lenses and at least one fixed lens to maximize utility. The positioning of the adjustable-position lenses in each system for specific desired magnifications and imaging distances can be analytically predicted through ray matrix calculations and can be further analyzed using a more complex MATLAB ray tracing program. In the case of the three-lens system, experiments using the lens positions given by the outputs of the ray tracing program confirmed the program's accuracy in determining lens positions for specific focal lengths, lens materials, and magnifications. Experimentally tested three-lens systems presented magnifications with a maximum deviation of 2.3% from the calculated values. Further experimentation with the four-lens system is expected to similarly confirm the accuracy of the MATLAB ray tracing program. Thus far, it appears that a three-lens system enabling adjustable magnification and total imaging distance merits serious consideration.

## **VIII. Acknowledgements**

Working at the Laboratory for Laser Energetics was an extremely fulfilling experience. First, I would like to thank my supervisor Dr. Seung-Whan Bahk for his endless guidance throughout this research, and for making this project available to the High School Program. I would also like to thank Dr. R. Stephen Craxton for both organizing the High School Program and for

giving me the opportunity to work at the lab. Finally, I would like to thank my family, friends, and fellow interns for their constant help and support throughout the program.

## **IX. References**

<sup>1</sup> “OMEGA EP System Operations Manual Volume VII–System Description Chapter 5: Optomechanical System,” S-AD-M-009 (August 2007).

<sup>2</sup> A. Gerard and J.M. Burch. *Introduction to Matrix Methods in Optics*. New York: Dover Publications, 1975.

<sup>3</sup> Bahk, Seung-Whan. “Matlab Ray Tracing User Manual.”

<sup>4</sup> M. Born and E. Wolf. “Principles of Optics.” 6th edition (1980). Chapter 9.

*Isotopic Exchange Over a Platinized Molecular Sieve*

**Alexander Proschel**

Pittsford Sutherland High School

LLE Advisor: Dr. Walter Shmayda

**Laboratory for Laser Energetics**

University of Rochester

Summer High School Research Program 2015

February 2016

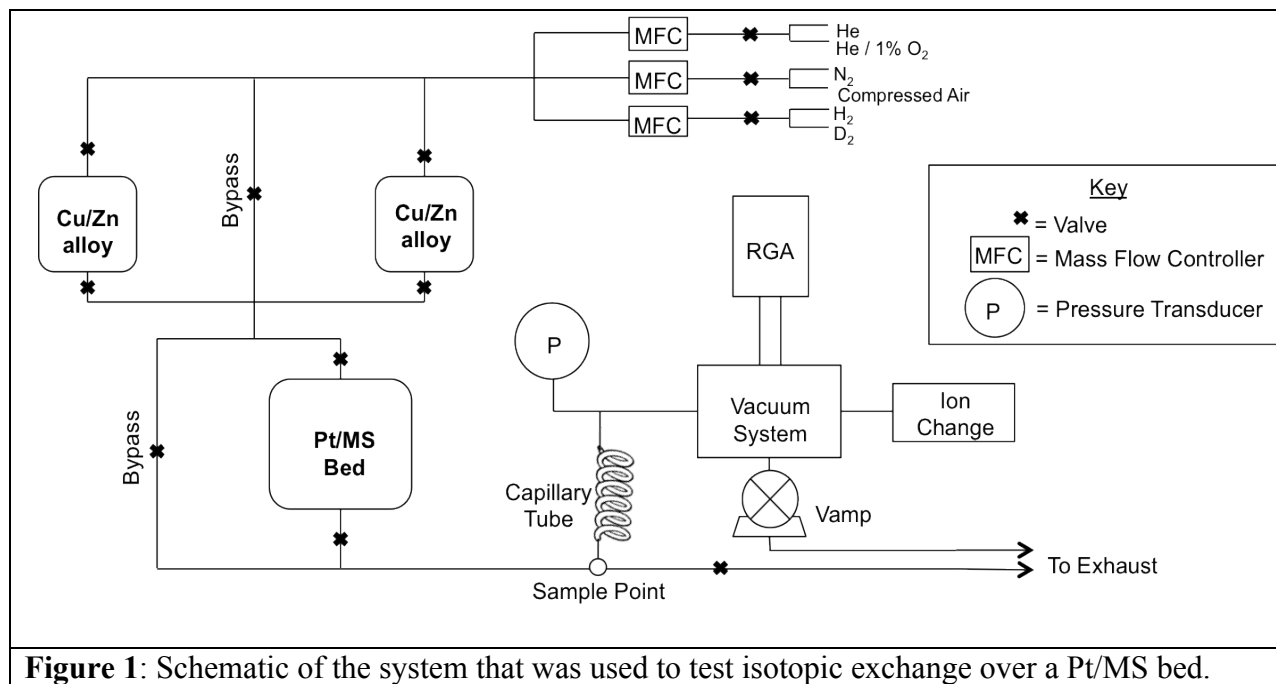
## Abstract

Tritium is a radioactive isotope of hydrogen used at LLE as a fusion fuel. The release of tritium to the workspace and to the environment must be controlled and minimized. The classical method of removing tritium from air relies on oxidizing elemental tritium to form tritiated water (HTO) followed by capture of the HTO on a molecular sieve drier. This work investigated the ability of platinized molecular sieve (Pt/MS) loaded with either light ( $H_2O$ ) or heavy ( $D_2O$ ) water to capture tritium. Deuterium was used as a surrogate for tritium in all the experiments. Hot copper/zinc beds were used to make heavy and light water to preload the Pt/MS bed. Either  $H_2$  or  $D_2$  gas was purged through the water-loaded Pt/MS bed while the composition of the Pt/MS bed effluent was monitored. The results showed that  $D_2$  displaces  $H_2$  from  $H_2O$  that is present in the Pt/MS bed with high efficiency.  $H_2$  can also displace  $D_2$  from the  $D_2O$  present in the Pt/MS bed but this process is less efficient.

### 1. Introduction

Tritium is an isotope of hydrogen that is used in many experiments at the Laboratory for Laser Energetics (LLE). However, since tritium is a low-energy beta emitter, its consumption via inhalation and its absorption through skin or through water can result in radiological doses that approach state-imposed limits for people consistently exposed to it (1). Additionally, low-level releases to the environment can accumulate and contaminate the environs of LLE. The typical process used at LLE to contain tritium is a method known as “burn and dry” (2). This strategy oxidizes elemental tritium turning it into tritiated water, which is then captured on a molecular sieve drier. This method requires the presence of oxygen and leads to the production of large quantities of low-activity water that need to be disposed of.

To enhance the capture of tritium in air without generating large amounts of low-level waste, we pursued an alternative concept. Prior experiments that were focused on testing metals determined that platinum was most effective at exchanging hydrogen out of the hydroxyl group (3). We decided to use the specific platinum molecular sieve Pt/4A MS because Heung and Staack found that Pt/4A MS had the best capacity and kinetics (4). The goal of this research was to further optimize the efficiency of Pt/4A MS. Parameters that affect the isotopic exchange efficiency are temperature, flow rate and the mass of isotope used to displace the isotope absorbed on the Pt/MS. In the experiments we conducted, the Pt/MS bed was preloaded with H<sub>2</sub>O or D<sub>2</sub>O and the isotopic exchange capabilities were measured by flowing D<sub>2</sub> or H<sub>2</sub> over the bed at conditions using various temperatures and flow rates.



## 2. Experimental Layout

A system was designed to test the ability of a Pt/MS bed to conduct isotopic exchange between isotopes of hydrogen. As displayed in Fig. 1, the system comprises multiple gas tanks or

lines (He, He/1% O<sub>2</sub>, N<sub>2</sub>, compressed air, D<sub>2</sub> and H<sub>2</sub>), two Cu/Zn alloy beds, the Pt/MS bed and a residual gas analyzer (RGA) to measure effluent from the beds. Gas is purged into the system from the tanks at specific flow rates controlled by mass flow controllers (MFC). The gases can then be directed using valves into the Cu/Zn alloy beds in order to make H<sub>2</sub>O or D<sub>2</sub>O or go through the bypass. The H<sub>2</sub>O or D<sub>2</sub>O can then be loaded onto the Pt/MS bed, preparing it for the test. Various combinations of gases at differing flow rates can then be purged into the Pt/MS bed allowing for isotopic exchange to occur. The effluent from the Pt/MS bed can then be measured by extracting the mixture of gases at the sampling point and sending them to the RGA. The RGA system includes capillary tubing, a pressure transducer, a vacuum system, an ion cage and an amplifier. The RGA is connected to a computer that allows the partial pressures of the gases in the effluent during experimentation to be tracked and recorded. The Cu/Zn alloy beds and Pt/MS bed are kept at elevated temperatures using band heaters that are monitored with thermocouples. Sections of the system are wrapped in electric heating tape to stop the volatile gases such as water from condensing inside the tubing.

### **3. Experimental Procedure**

The process to test whether isotopic exchange over a Pt/MS bed is viable starts with preloading the Pt/MS bed with either H<sub>2</sub>O or D<sub>2</sub>O. Once the bed is filled with light or heavy water, combinations of gases are flowed into the bed. For example, to test the ability of D<sub>2</sub> to displace H<sub>2</sub>O, D<sub>2</sub> was flowed into the preloaded Pt/MS bed at different flow rates with another gas such as N<sub>2</sub> acting as a carrier gas. The influence of temperature on the isotopic exchange rate was investigated by varying the temperature of the Pt/MS bed. The experiments were repeated with H<sub>2</sub> gas flowed into a D<sub>2</sub>O-preloaded Pt/MS bed. The RGA was used to measure partial pressures of the effluent of the bed in order to measure what gas was being pushed out of the bed

and what gas remained inside the bed. Since partial pressure data depend on several parameters, the flow rate was calculated using Eqn. (1),

$$\text{Flow Rate} = \frac{\text{Partial Pressure}}{\text{Calibration Partial Pressure}} \times \text{Calibration Flow Rate From MFC} \quad (1)$$

where the calibration quantities were obtained prior to each run as described in Sec. 4. The isotopic exchange occurring inside the Pt/MS bed is presented as flow rate data [mL/min] versus time or quantity of gas flowed into the Pt/MS bed.

#### 4. Calibration

Before the main experimentation could be conducted, preliminary calibration data was recorded. Gathering calibration data simply means recording the partial pressure readings the RGA produces at specific flow rates for individual gases. Valves leading into the Cu/Zn alloy beds and the Pt/MS bed were shut and the gas was sent through the bypasses directly to the sampling point. Gas was released into the system at a specific flow rate (measured by the MFC) until the partial pressure reading from the RGA leveled out. This partial pressure and the flow rate were then recorded. This enabled partial pressures collected by the RGA during experimentation to be converted into flow rate data using Eqn. (1), even when gases were being trapped inside the Pt/MS bed.

#### 5. Results

The experimentation was based around three variables: flow rate, temperature of the Pt/MS bed and the difference of the abilities of H<sub>2</sub> and D<sub>2</sub> in isotopic exchange. Fig. 2 shows a side-by-side comparison of the gases leaving the Pt/MS bed filled with light water as a function of time as D<sub>2</sub> flows over the Pt/MS bed at two different flow rates. In this figure the temperature of the Pt/MS is fixed at 20°C and the nitrogen carrier is set to 200 ml/min. The deuterium flow

rate through the bypass is set to 50 ml/min and 100 ml/min in the upper and lower panels, respectively. At time approximately 15 min, when the D<sub>2</sub> flow is diverted from the bypass to the bed, the composition of the downstream hydrogen changes from pure D<sub>2</sub> to ~ 82% H<sub>2</sub> and ~10% HD. Evidently at least 92% of the incoming D<sub>2</sub> displaces H<sub>2</sub> from the water bound to the MS to form an H<sub>2</sub> effluent. This exchange process continues for about 60 min with a D<sub>2</sub> flow rate of 50 ml/min before D<sub>2</sub> appears downstream. Increasing the flow rate from 50 to 100 ml/min improves the isotopic exchange to 92% H<sub>2</sub> and decreases the production of the mixed isotope, HD, to 6%. The D<sub>2</sub> purge gas appears in the effluent about 30 min after the purge is diverted into the bed.

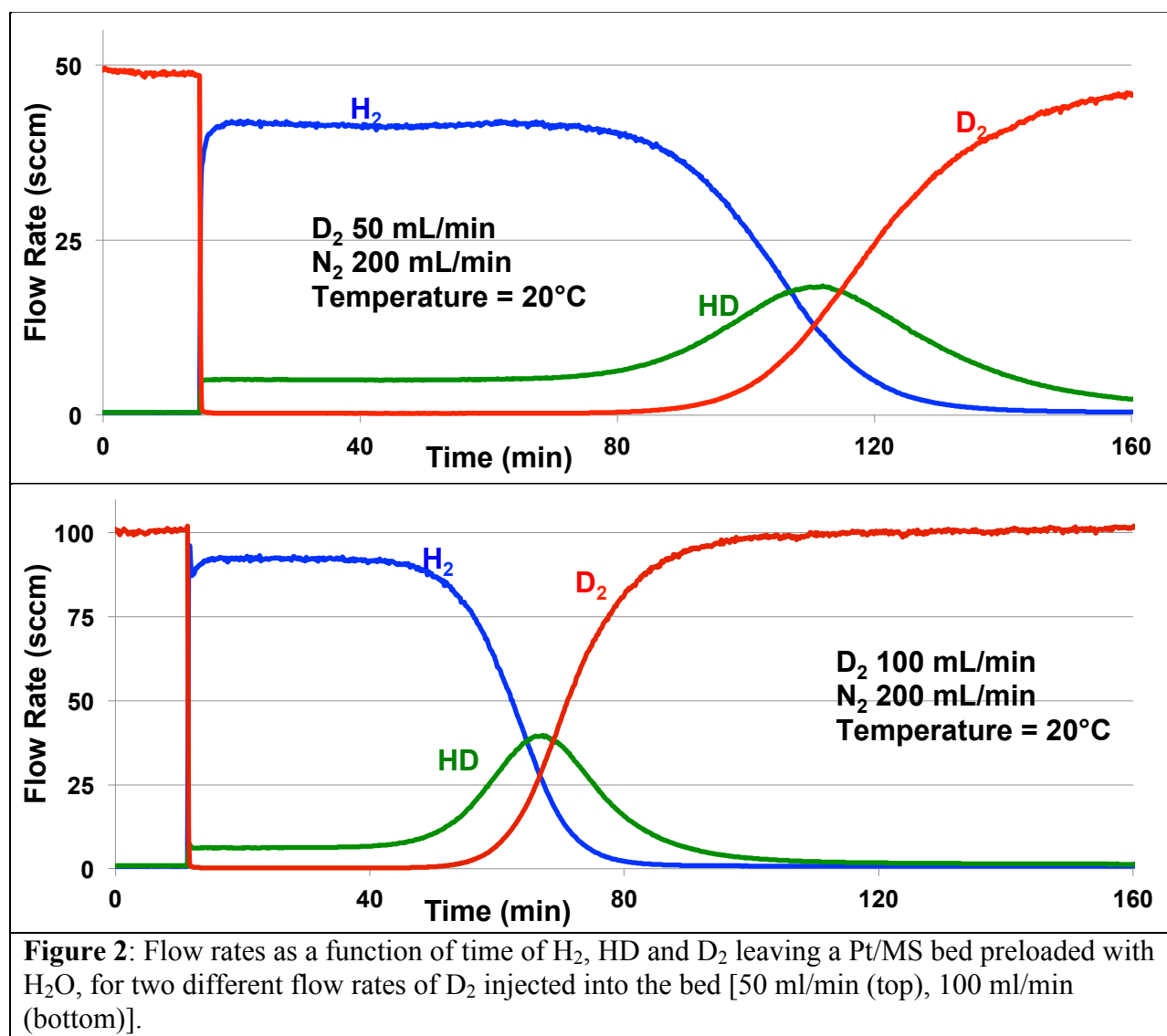
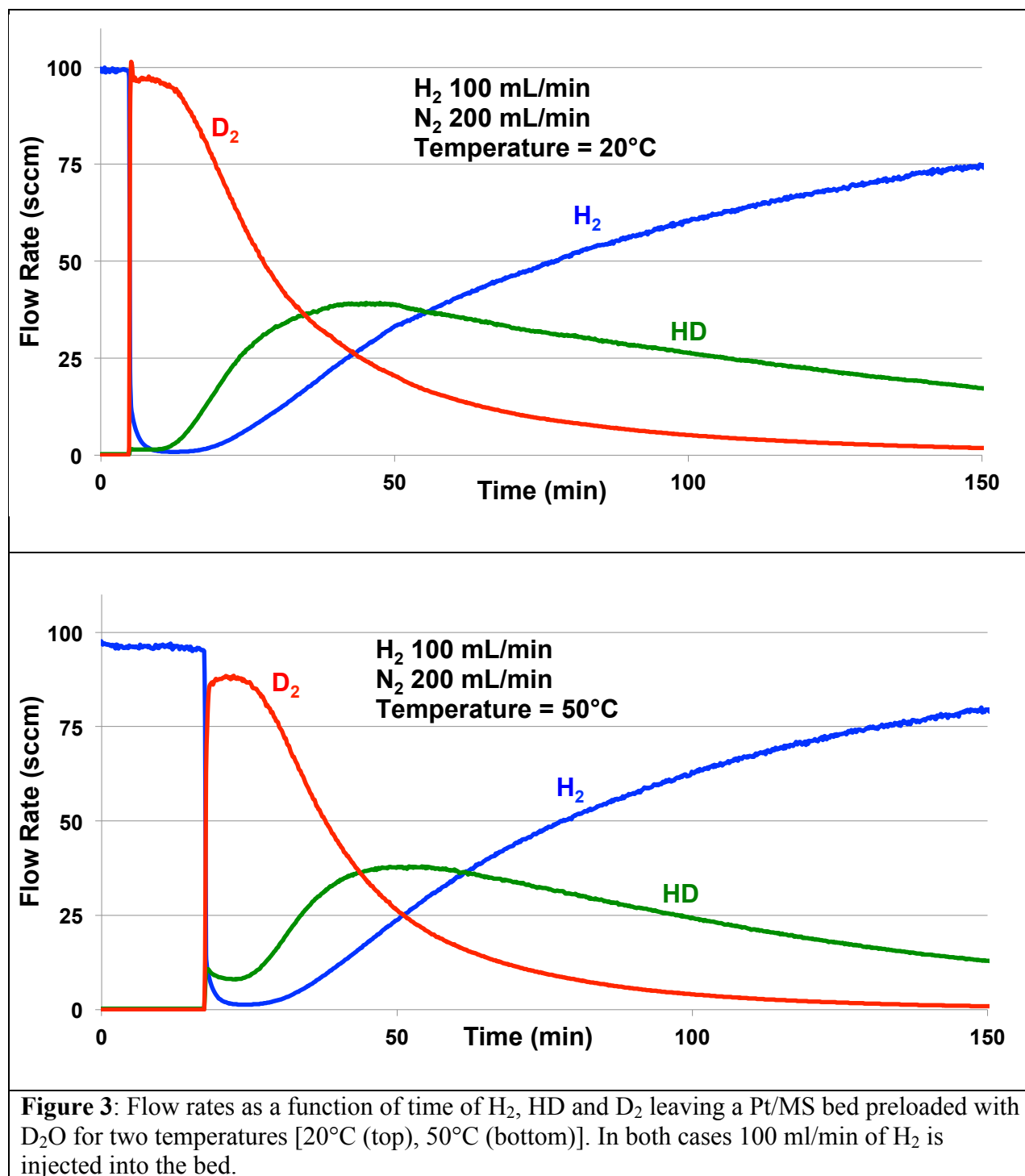


Fig. 3 shows the effect of displacing  $D_2$  bound to a Pt/MS bed preloaded with  $D_2O$  when  $H_2$  is flowed through the bed. In this case the  $H_2$  flow rate is fixed at 100 ml/min, the  $N_2$  carrier flow rate remains fixed at 200 ml/min and the temperature of the Pt/MS bed is set to  $20^\circ C$  in the upper panel and to  $50^\circ C$  in the lower panel. As in the previous case Fig. 3 shows the evolution of the hydrogen composition with time. When the hydrogen stream is directed into the bed around the 20-minute mark  $H_2$  is observed to disappear from the bed effluent with a concomitant increase in  $D_2$  and HD. This figure shows that while it is possible to displace the heavier isotope with the lighter one, the high displacement effectiveness lasts about 10 minutes. Increasing the bed temperature from  $20^\circ C$  to  $50^\circ C$  degrades the isotopic exchange effectiveness by encouraging the formation of HD. A comparison of Figs. 2 and 3 shows that the heavier isotope is more efficient at displacing the lighter isotope for a significantly longer time.

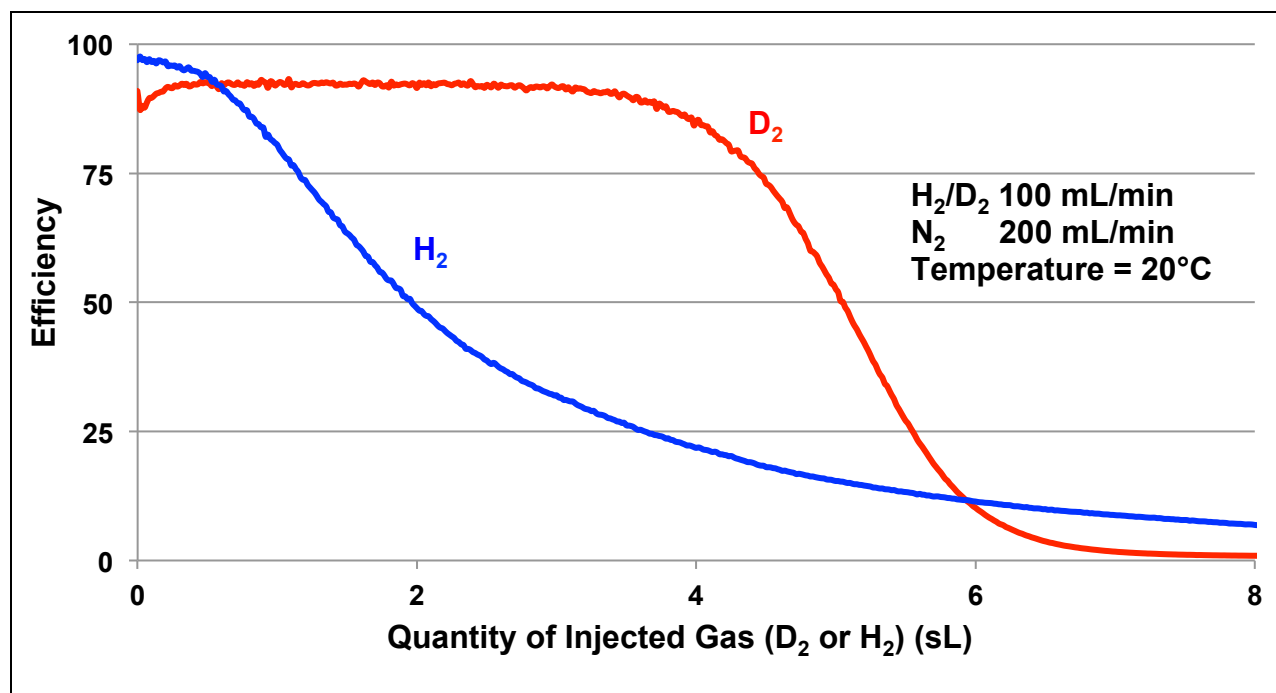


The displacement efficiency, defined as the percentage of the injected gas that is captured in the Pt/MS bed, is quantified in Fig. 4, which is obtained by integrating data shown in Figs. 2 and 3 with respect to time. Fig. 4 compares the displacement efficiency using either D<sub>2</sub> or H<sub>2</sub> as

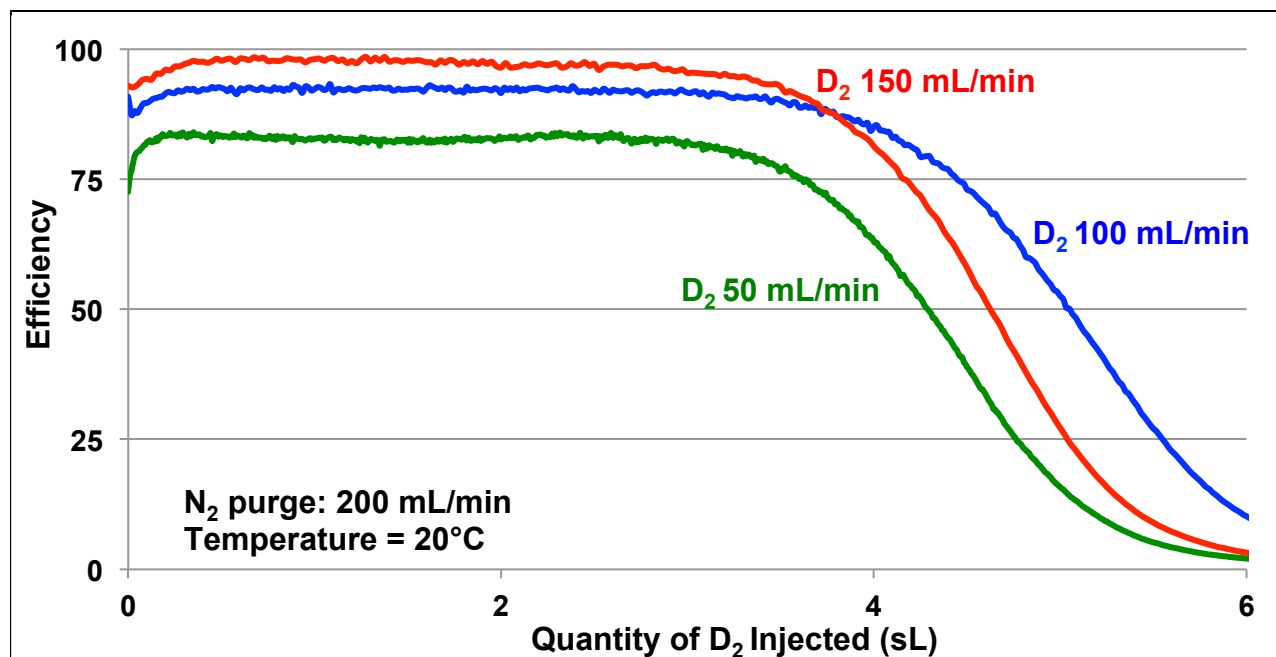
the injected gas, as a function of the amount of injected gas passed through the bed, for the same flow rate and bed temperature. The figure shows that 92% of the  $D_2$  entering the bed is used to displace bound hydrogen. This displacement efficiency continues until approximately 4 liters of gas have been injected into the bed. In contrast, the effectiveness of hydrogen at displacing deuterium drops to 50% after just 2 liters of hydrogen have been injected into the bed. Clearly, the heavier isotope can displace the lighter isotope more efficiently.

Fig. 5 provides the dependence of displacement efficiency of isotopic exchange on injected volume at various deuterium flow rates. It is evident that increasing the flow rate through the bed improves the exchange rate. However, a point will be reached where higher flow rates will cause laminar flow to deteriorate into a turbulent flow. This could counteract the increase in efficiency and may cause the system to become less efficient. This point of conversion can be predicted by the Reynolds number, which is directly related to areal velocity or flow rate and is  $<10$  in our system. Mixing may be important, so it might be that a higher Reynolds number and therefore a certain degree of turbulence could be desirable since this would allow for more surface area for the exchange to occur. The impact of increasing the Reynolds number on the efficiency of the system may warrant more experimentation.

Fig. 6 plots the displacement efficiency with which  $H_2$  is captured in a Pt/MS bed preloaded with  $D_2O$  as a function of injected volume for two temperatures. A higher temperature results in a lower efficiency. Similar behavior has been observed when using deuterium as the injected gas.



**Figure 4:** Red curve: displacement efficiency with which injected  $D_2$  is captured in a Pt/MS bed preloaded with  $H_2O$ , as a function of the quantity of injected  $D_2$ . Blue curve: same for injected  $H_2$  and a bed preloaded with  $D_2O$ .



**Figure 5:** Displacement efficiency of  $D_2$  in a Pt/MS bed preloaded with  $H_2O$  as a function of the quantity of injected  $D_2$ , for three  $D_2$  flow rates. The curve for 100 ml/min matches the red curve of Fig. 4 (note the different horizontal scale).

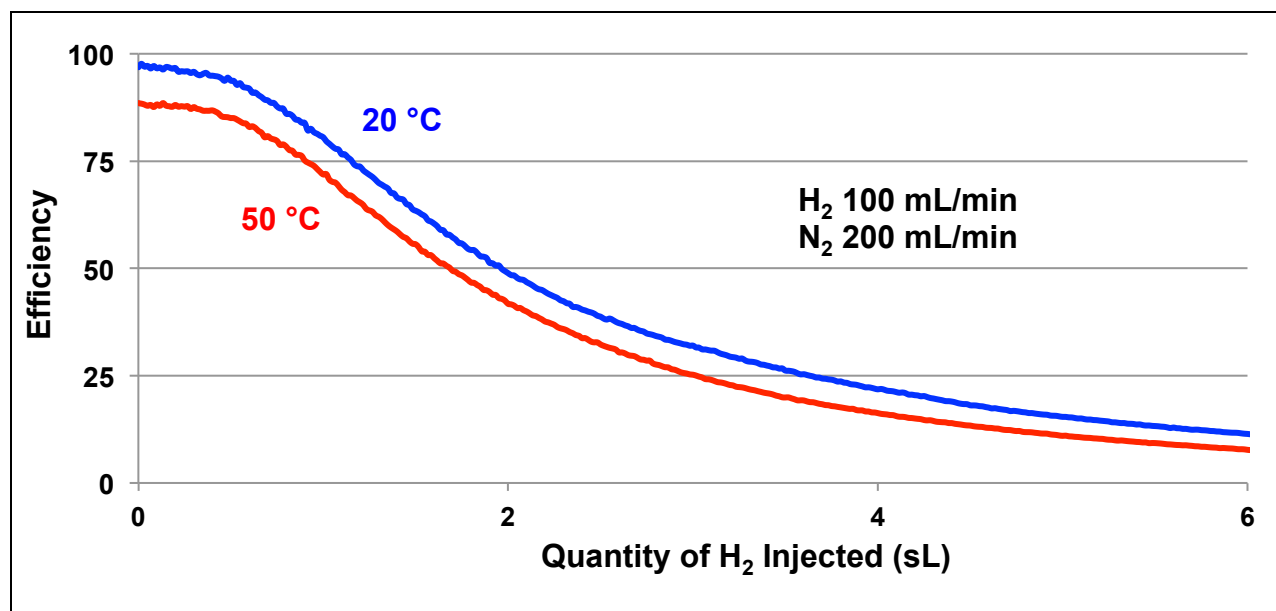


**Figure 6:** Efficiency as a function of quantity of H<sub>2</sub> injected into a Pt/MS bed preloaded with D<sub>2</sub>O, for two different temperatures. The 20°C curve is the as the blue curve of Fig. 4.

## 7. Conclusions

Our experiments afford several conclusions:

1) The heavier isotope of hydrogen is more efficient at displacing bound hydrogen with respect to isotopic exchange inside the Pt/MS bed. Noting that we used deuterium as a surrogate for tritium, it seems likely that tritium would perform in a similar manner.

2) Injecting the gas into the Pt/MS bed at higher flow rates increases the displacement efficiency. Because of this, a system that would implement this technology for tritium mitigation should be designed to withstand high flow rates to optimize efficiency.

3) Isotopic exchange is more efficient at lower temperatures.

A limitation of our study is the relatively small scale on which these pilot experiments were conducted. Large full-scale tritium mitigation systems, which will require Pt/MS beds with far larger capacity, would potentially react differently to the parameter variations tested here. For example, the Reynolds number must be kept low to ensure that the flow through a scaled-up

Pt/MS bed remains laminar. This can be accomplished by decreasing the mean velocity of the gas through the bed as the diameter increases or by simply keeping the diameter constant and increasing the length of the bed. An alternative solution could be to maintain single small beds but assemble them into a parallel mitigation system. The translation of this work to large-scale systems could provide an effective and feasible solution to the problem of tritium containment.

## **8. Acknowledgements**

I would like to thank Dr. Craxton and Dr. Shmayda for giving me the opportunity to come to the Laboratory for Laser Energetics and be a part of such a wonderful internship program. It has been an amazing experience. I would also like to thank Dr. Shmayda and Ian Gabalski for their invaluable guidance and assistance in my research project.

## **9. References**

1. Idaho State University, Radiation Information Network, Tritium Information Section  
<http://www.physics.isu.edu/radinf/tritium.htm>
2. W. T. Shmayda, "Technologies for Mitigating Tritium Release to the Environment," LLE Review **103**, pp. 142-154 (2005).
3. G. Bond and P.B. Wells, "Enantioselective Hydrogenation," Journal of Catalysis **150**, issue 2, pp. 329 (1994)
4. L.K. Heung and G. C. Staack, "Hydrogen Isotope Exchange Properties of Porous Solids Containing Hydrogen," Fusion Science and Technology **48**, pp. 585-588 (2005).

*Analysis of CVD diamonds for neutron detection on the OMEGA laser*

**Ishir Seth**

Brighton High School

Advisor: **Dr. J. Knauer**

Laboratory for Laser Energetics

University of Rochester

Rochester, New York

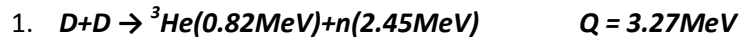
July 2016

## I. Abstract

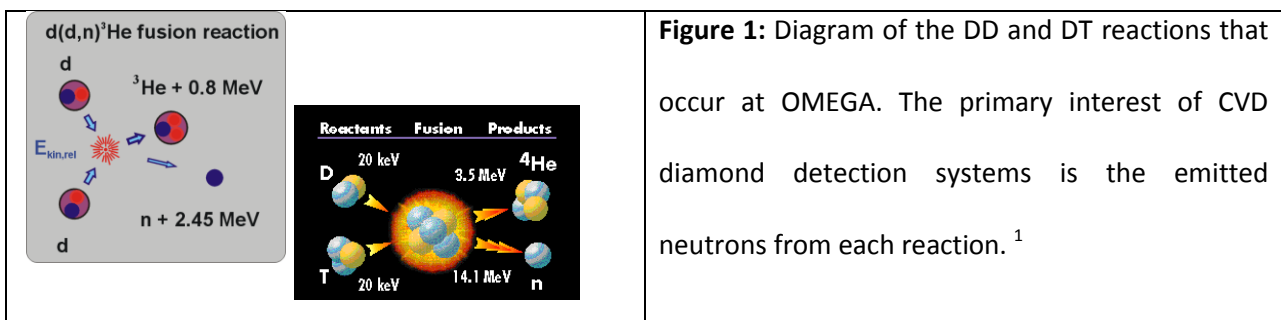
Neutron energy deposition in chemical vapor deposition (CVD) diamond detectors was quantified. Diamond detectors have significant advantages over scintillator systems for neutron detection since they express faster response times, have enhanced energy resolution, and can be operated at room temperature. Data were obtained for four detectors used on the OMEGA laser. A neutron detection model was developed to quantify the energy deposited per neutron interaction using measured detector sensitivities. The average energy deposited per neutron interaction was 27 to 44 keV for 14-MeV neutrons and 4.8 keV for 2.5-MeV neutrons. Using the known electron mobility in diamond and signal rise times, the effective thicknesses of the detectors were calculated. This work establishes an energy deposition model that will aid in the development of future CVD diamond detectors for use in fusion reaction diagnostics.

## II. Introduction

Harnessing the energy from fusion reactions remains a tantalizing opportunity for creating a source of clean renewable energy. The field of fusion research has advanced through a greater understanding of high-energy laser-matter interactions. At the OMEGA facility, 60 laser beams provide a total of 30 kJ to a small, spherical target containing deuterium (D) and tritium (T) isotopes in order to create fusion reactions during an implosion. While the ultimate goal of a sustainable fusion reaction has not yet been reached, increased efforts are currently underway to improve the quality, stability and uniformity of implosions. The OMEGA laser beams deliver enough energy to overcome the electromagnetic force of repulsion that occurs between positively charged deuterium and tritium. As a result, two major reactions occur during an implosion at OMEGA:



These reactions, the fundamental process of energy generation at OMEGA, are illustrated in **Fig 1**.



In both cases, most of the reaction energy ( $Q$ ) is stored in an emitted neutron. Thus, in the hopes of improving the energy output and gain of fusion reactions it is critically important to understand the nature of these emitted neutrons. Furthermore, a thorough analysis of the resulting neutron spectra lends insight into critical aspects of the implosion itself such as the fuel ion temperature, density, and the time of maximum compression. A thorough neutron diagnostics suite is essential for the advancement of fusion energy research.

A wide variety of neutron diagnostics systems are used at OMEGA to analyze and detect the emitted neutron spectra emitted from an implosion. Most detection schemes involve the use of plastic or liquid scintillators, which measure the light output created when neutrons interact with the detector. Although traditional scintillators provide critical information about the emitted neutrons, they are hindered by some problematic flaws inherent to their detection mechanism and overall design. First, scintillators have a tendency to age over time, leading a change in their detection properties over time and forcing researchers to adjust and recalibrate. Furthermore, scintillators have a long time response, which prevents them from being utilized effectively at short distances from the target chamber center (TCC). In high-radiation magnetic fusion environments, highly energetic neutrons and other forms of radiation can cause damage to scintillators and reduce their overall effectiveness. While scintillators will always be a staple of neutron diagnostics, other neutron detection mechanisms must also be considered. A novel detection system that utilizes synthetic diamonds is currently in use in the OMEGA facility.

Chemical vapor deposition (CVD) diamond detectors<sup>2-5</sup> utilize semiconductor properties to detect neutrons. Incident neutrons interact with stationary carbon atoms through collisions to create charged electron-hole pairs. As seen in **Fig 2**, under an applied E-field, the pairs migrate towards the electrodes and create an electrical signal.

Diamond possesses significant and promising advantages over scintillators due to its inherently wide bandgap of 5.5 eV, which reduces the amount of noise generated in the output signal. Additionally, the high density and radiation hardness of diamond provides great tolerance to the radiation-intensive environments that can be found in some fusion environments. The short lifetime of charge carriers in diamonds allows these detectors to have a fast time response, leading to accurate signal outputs at very short distances from TCC. Chemical vapor deposition (CVD) is an emerging technique used to emulate the attractive qualities that can be found in naturally occurring diamond. Since natural diamond is rare and expensive, CVD techniques allow for the artificial growth of diamond crystals in a high-pressure, high-temperature environment. The growth and deposition process is both precise and highly controlled to allow for the optimization of crystal structure and to minimize defects such as bubbles and irregularities that might impede charge flow through the diamond.

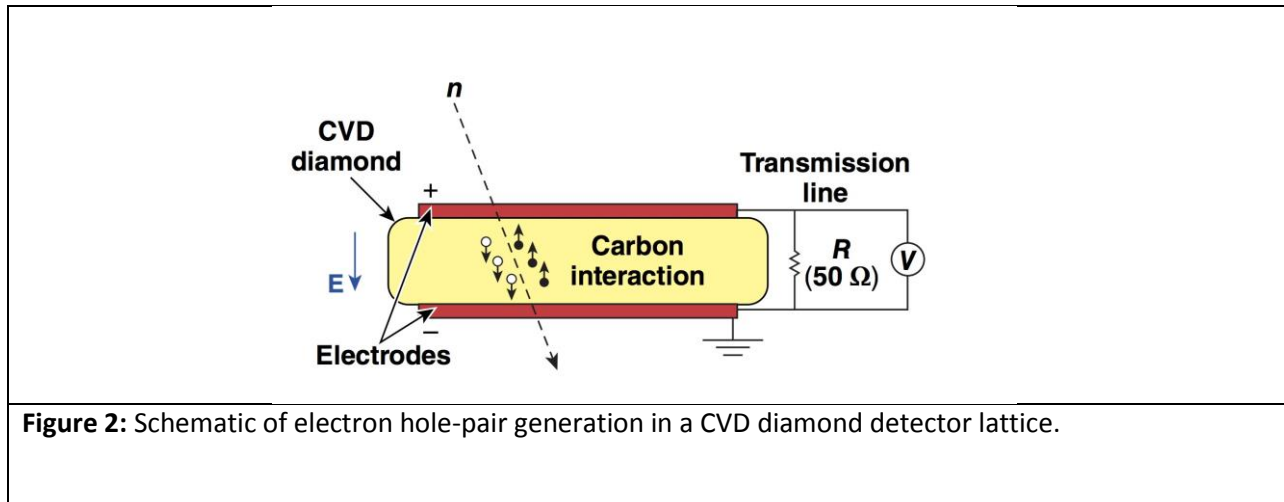


**Figure 2:** Schematic of electron hole-pair generation in a CVD diamond detector lattice.

Extensive research has been conducted over the last three decades regarding the use of CVD diamonds for particle detection in fusion environments. While significant progress has been made into improving the overall quality and design of these detectors, the sensitivity difference between 2.45 MeV neutrons and 14 MeV neutrons has not been fully solved. Through the analysis of signal outputs as well as the physical properties of these detectors, this study quantifies the energy deposition that occurs in these diamonds from neutron interactions. In the hopes of creating the next generation of highly sensitive and highly dynamic detectors, a thorough understanding of energy deposition and signal generation from various neutron sources is essential.

This study creates and tests a model that quantifies the energy deposition that occurs in diamond detectors from neutron interactions. Using measured detector sensitivities, calculated neutron interactions, and the solid angle of the detector the energy deposition per neutron interaction was calculated using this model. Additionally, using signal rise times, the effective thickness of the detectors was calculated. This analysis represents a unique investigation into the energy deposition interaction that occurs when emitted neutrons enter the detection lattice.

### **III. Signal generation in CVD diamond detectors**

Diamond detectors rely on a neutron energy conversion process in order to generate a signal. Emitted neutrons during an implosion travel through the OMEGA bay and impact the diamond surface of the detector. Through particle collisions, highly energetic neutrons interact with stationary carbon nuclei through multiple reaction channels to generate charged particles. The reaction channels of primary interest are shown in **Table 1**, taken from Ref.6:

**Table 1: Reaction channels between incident neutrons and carbon lattice from Ref. 6.**

<b>Reaction</b>	<b>Threshold (MeV)</b>
$^{12}\text{C}(n,\gamma)^{13}\text{C}$	<b>0</b>
$^{12}\text{C}(n,\alpha)^9\text{Be}$	<b>6.18</b>
$^{12}\text{C}(n,n'\alpha)^4\text{He}$	<b>7.88</b>
$^{12}\text{C}(n,n'\alpha)^8\text{Be}$	<b>7.98</b>
$^{12}\text{C}(n,2\alpha)^5\text{He}$	<b>8.85</b>
$^{12}\text{C}(n,p)^{12}\text{Be}$	<b>13.64</b>

Of these reactions, the  $^{12}\text{C}(n,\alpha)^9\text{Be}$  reaction is critical as it contributes the greatest towards signal generation. The high threshold of 6.18 MeV allows for the reduction of signal noise from other particle emissions that occur during a target implosion. In the diamond lattice, the resulting charged particles—namely alpha and beryllium—generate electron-hole pairs through the excitation of electrons from the valence band to the conductance band. This continuous charge migration of electrons traveling to the positive electrode and their corresponding “holes” traveling to the negative electrode creates a current, which can be measured by a voltmeter following appropriate amplification and noise reduction. The duration of charge carrier generation is directly linked to the duration of incident neutron collisions; a peak in the voltage signal is directly correlated to a pulse of neutrons.

Signal generation is highly dependent on the intrinsic properties of the diamond lattice itself since defects or irregularities can impede the natural flow of electrons towards the positive electrode. Thus,

the manufacturing process of each synthetic diamond must be considered in order to improve detection accuracy and detector sensitivity.

Currently, there are three active CVD diamond detectors installed on OMEGA. The first is installed 5.8 m from TCC, the second is 15.9 m from TCC and the third is 5.0m from TCC. This work focuses on the two CVD diamond detectors that are part of a new 3-axis detector system on OMEGA. These are the 5.8 m and 15.9 m detectors which are located along the same line-of-sight. The voltage signals from the detectors undergo processing through connected electronics, which typically consist of an amplifier and a voltmeter. Using MATLAB routines, the data from the voltmeter can be used to combine the signal outputs from the different detectors as a function of time, as shown in **Fig.3**. The fixed CVD detector positions as well as the predictability of neutron production and flight leads to relatively consistent signal shapes over multiple shots and various experiments.

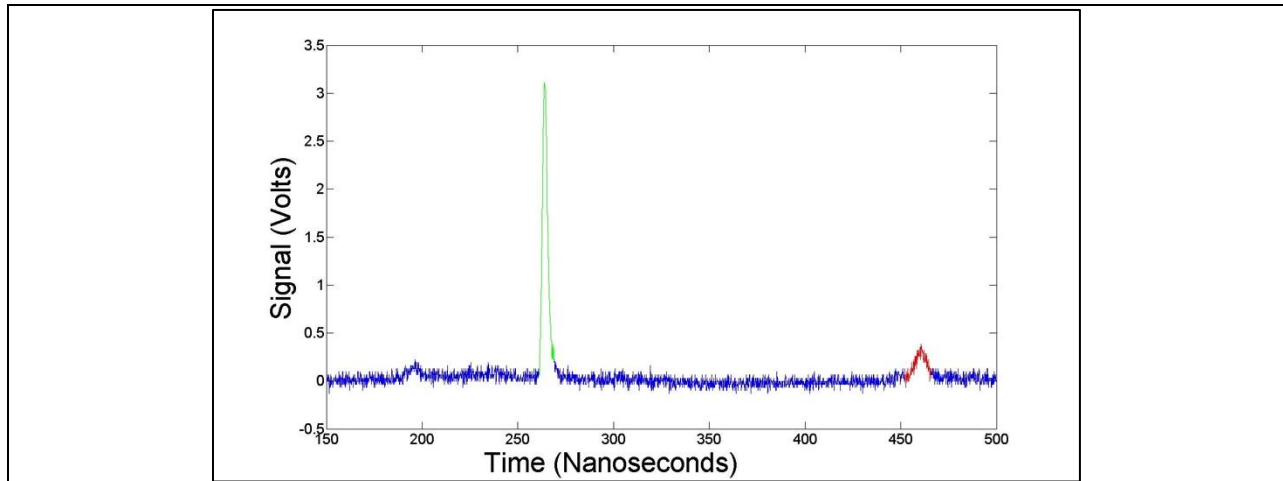


**Figure 3:** Signal output of a DT reaction as viewed in MATLAB programming software. The green peak indicates the signal generated at the 5.8 m CVD and the red peak indicates the signal generated at the 15.9-m CVD. The rise time, amplitude and full width at half maximum of this signal contain information regarding the neutrons emitted from the implosion.

The two distinctive peaks in **Fig 3** indicate the arrival of neutrons at each of the detectors. The first peak is the signal output from the closer detector at 5.845 m from TCC. It is important to note that the peak from the first detector is several times greater than the peak from the second detector (red). Furthermore, significant noise can be visualized in the peak signal output from the far detector, which can be attributed to various factors including neutron scattering background from the surrounding structures and a significantly smaller amount of incident neutrons at that distance. The small blue peak seen at around 170 ns is generated from gamma radiation that was created when the neutrons collided with the inner surface of the target chamber. The integral of the peak signal is used to calculate the sensitivity and energy deposition in these detectors, as shown in the following sections. Multiple voltage signals from two different campaigns on OMEGA were used to characterize the performance of four CVD diamond detectors.

#### IV. Energy deposition model

A phenomenological model was created to estimate the energy deposited per neutron interaction in a CVD detector. Estimating this energy is important as it provides insight into the capacity of CVD diamond detectors to withstand high energy fluxes and is relevant to understanding energy saturation in these detectors. This model incorporates detector location, reaction cross-section, and measured signal data to generate a value.

First, the number of neutron interactions ( $N_{int}$ ) within the diamond detector lattice is calculated.

$$N_{int} = N_{inc} \sigma t n_c \quad (1)$$

where  $N_{inc}$  indicates the number of incident neutrons,  $\sigma$  is the total cross section for neutron-carbon interactions,  $t$  is the thickness of the detector and  $n_c$  is the number density of carbon atoms. The

likelihood of interaction is thus directly dependent on the cross section for the reaction, which varies based on the incident neutron energy.

The number of incident neutrons is calculated as follows:

$$N_{inc} = N_y * \frac{\Omega_{det}}{4\pi} \quad (2)$$

where  $N_y$  is the total neutron yield for the implosion, and  $\Omega_{det}$  is the detector solid angle. The number of incident neutrons differs from the number of neutron interactions because only a fraction of the incident neutrons will interact with carbon nuclei. Next, the number of electron-hole pairs ( $N_{eh}$ ) generated based on signal data is calculated:

$$N_{eh} = \frac{\int V dt}{2eR} \quad (3)$$

where  $e$  is the electron charge,  $R$  is the resistance of the detection system, and  $\int V dt$  is the integral of the voltage signal over the peak measured by the CVD diamond detector.

Using the number of electron hole pairs generated and the number of interactions within the detector, the average energy deposited per neutron interaction is calculated:

$$E_{dep} = E_0 * \frac{N_{eh}}{N_{int}} \quad (4)$$

where  $E_0$  is the energy needed to create an electron-hole pair in diamond which is 13.2 eV. This model was then applied to four CVD diamond detectors that have been employed in different OMEGA experiments.

## V. Setup of CVD diamond detectors

This study analyzes data sets obtained from four CVD diamond detectors in OMEGA, shown in **Fig 4**. A 2005 campaign utilized a CVD diamond detector setup that was situated 0.5 m from TCC and used to measure the bang-time for reactions. This setup consisted of high-yield neutron bang time detectors (HYNBT) that were used for detection of both DD and DT neutron reaction emissions. The two data sets from that campaign used in this study are referred to as HYNBT DT and HYNBT DD data.

As previously discussed, two CVD detectors are currently installed in OMEGA, at 5.845 m and 15.851 m from TCC. These detectors consist of two individual polycrystalline wafers and are located along the P2-P11 axis. Amongst the wide range of neutron diagnostic systems installed on OMEGA, these two CVD diamonds provide the unique ability to calculate the transit time between the two detectors. This transit time over the 10 m between the first detector (5.8-m CVD) and the second detector (15.9-m CVD) can provide information on the motion of the center of the mass of the neutron emitting region.

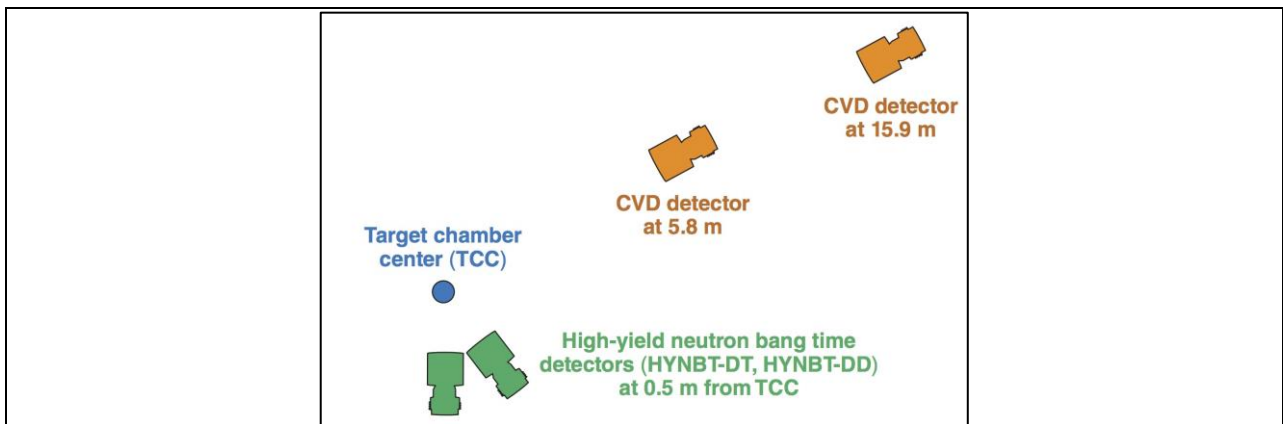
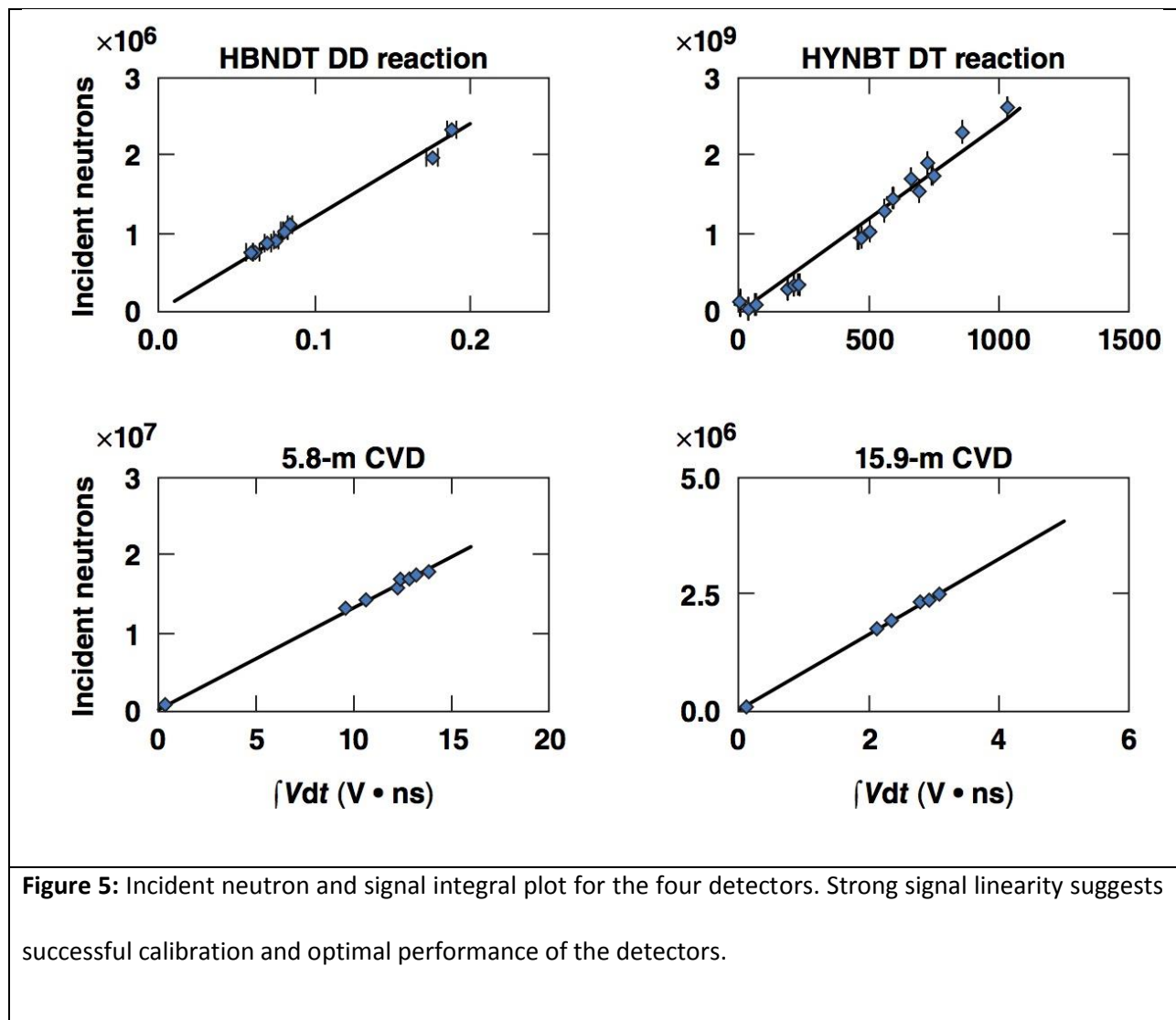


**Figure 4:** Locations of HYNBT DT, HYNBT DD, 5.8-m CVD and 15.9-m CVD detectors in the OMEGA facility with respect to the target chamber center.

## VI. Analyzing detector sensitivity and signal linearity

The first step in understanding the performance of these CVD diamond detector setups was analyzing the relationship between the incident neutrons calculated using **Equation 2** and the signal amplitude obtained as the integral of the voltage signal over the peak. This is shown in **Fig 5** for the four detectors. Linearity of signal output is indicative of detector performance and shows that the detectors have been successfully calibrated to the OMEGA environment.



Further information can be derived from these plots by determining a quantity known as sensitivity. The sensitivity of the detectors ( $\alpha$ ) in V\*ns/neutron is calculated as the signal in volt\*ns generated by one incident neutron:

$$\alpha = \frac{\int V dt}{N_{inc}} \quad (5)$$

The sensitivities of the four data sets are shown in **Fig 6**.

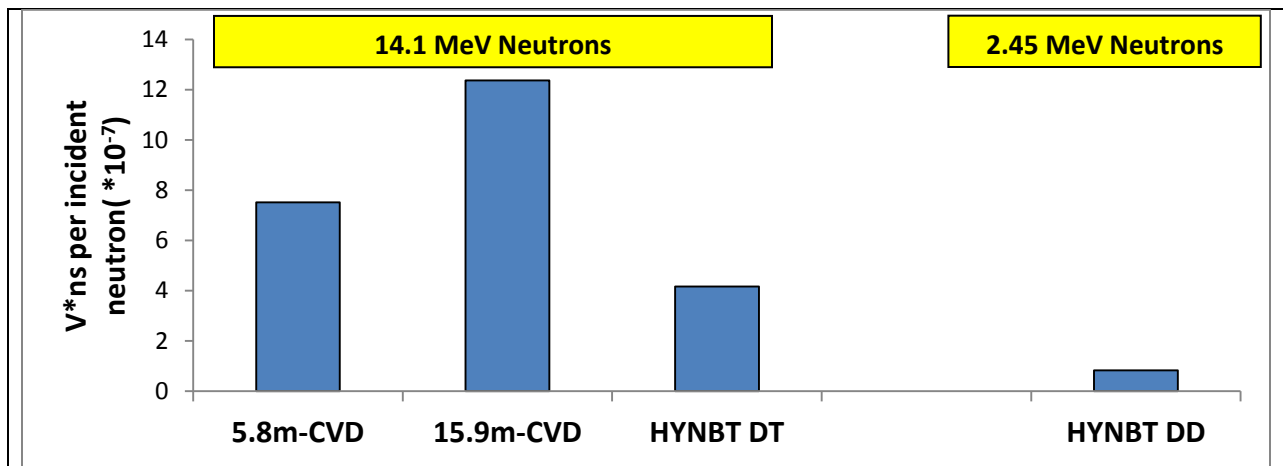


**Figure 6:** Sensitivity of the four data sets. Sensitivity represents the signal generated in the detector per incident neutron. The data indicates great variability in sensitivity.

Detectors that generate a greater signal per single incident neutron exhibit greater sensitivity. Consequently, **Fig. 6** indicates that the 15.9-m CVD diamond detector exhibits the greatest sensitivity while the HYNBT detector has the lowest sensitivity. When comparing the HYNBT DT data to the HYNBT DD data, the results indicate that the detector has higher sensitivity for 14 MeV neutrons. In addition, as evidenced by **Fig. 6** there is great variation in sensitivity between the four detectors. The variability in

sensitivity could stem from a variety of factors. The fabrication of the detector can affect sensitivity by altering physical properties that affect charge flow such as mosaic structure, unintended dopants, dopant concentration, and crystalline size. These features impact the electron flow within the lattice in different ways, creating differences in signal amplitude and detection capabilities. Additionally, sensitivity scales with thickness in that thicker detectors will exhibit greater sensitivity. Other causes for variation in sensitivity are currently undetermined and merit further exploration. The great variation in sensitivity found in the OMEGA detectors indicates that a more uniform synthesis process will be required in future CVD diamond neutron detection setups. Furthermore, this data indicates that it is critical to consider the specific synthesis process of each CVD diamond wafer when analyzing signal data from these detectors.

## **VII. Energy deposition in detectors**

The central component of this study is the creation and application of a model that utilizes detector data to quantify neutron energy deposition. Quantifying deposited energy for each neutron interaction is important for providing insight into the conditions in which CVD diamond detectors must operate. Furthermore, this study represents a novel analysis, as there are few response models for CVD diamond detectors that explore energy deposition for neutron interactions. The general model developed in **Section IV** was applied to data obtained from the four datasets that were analyzed in previous sections. The resulting values for energy deposition determined by **Equation 4** are given in **Fig. 7**.

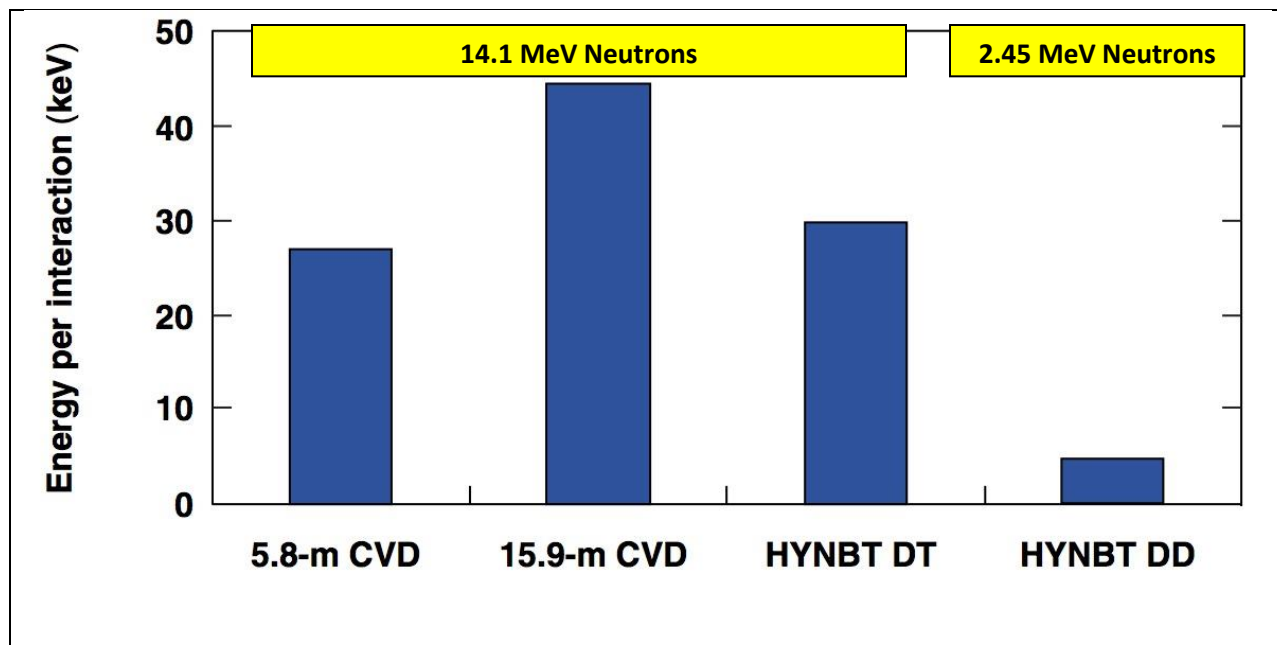


**Figure 7:** Energy deposited per neutron interaction in CVD diamond detectors. These values are the result of the application of a model that incorporates a variety of factors including detector location and thickness, neutron-carbon cross sections, and signal data analyzed in MATLAB.

Based on this data, the greatest deposited energy per neutron interaction occurs in the 15.9-m CVD detector. Directly comparing the data from the HYNBT campaign, the energy deposited from the DT reaction was 29.9 keV and the energy deposited from the DD reaction was 4.84 keV. This finding is supported by the fact that DD neutrons are emitted with lower energy and have a lower reaction cross-section in diamond.

### VIII. Effective thickness of detectors

A final measure of detector performance is effective thickness, a value that acts as a measure of charge collection efficiency. Essentially, the effective thickness represents a fraction of the total thickness of the CVD diamond wafer and is indicative of the fabrication quality and detection capabilities of the detector. The effective thickness was calculated using a modified equation from a study by Coropceanu et al. as follows<sup>7</sup>:

$$L_{eff} = \tau * \mu * \frac{V}{L} \quad (6)$$

where  $\tau$  represents the signal rise time calculated by determining the time from 10% of the signal maximum to 90% of the signal maximum,  $\mu$  represents the electron mobility in diamond,  $L$  represents the actual thickness of the wafer, and  $V$  represents the bias voltage. The effective thickness is illustrated in **Fig. 8**.

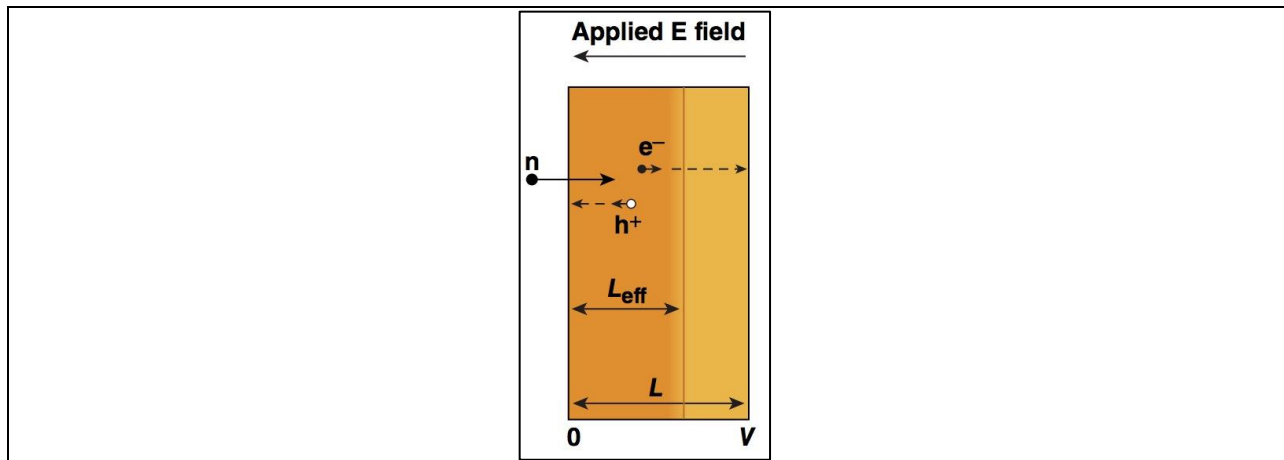
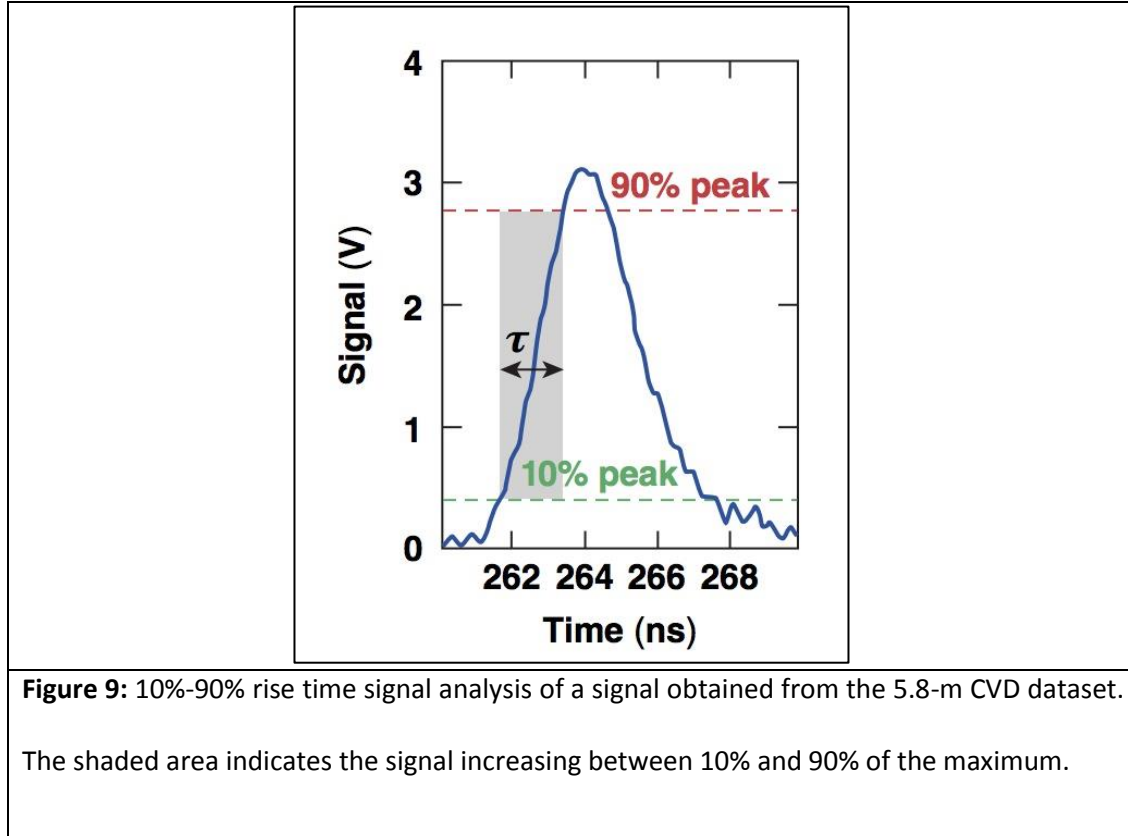


**Figure 8:** Rough visualization of effective thickness and the parameters  $L$  and  $V$  used in its calculation.

Effective thickness is typically a fraction of the total thickness of the detector.

A MATLAB program was used to calculate the signal rise time. The signal for the 5.8-m CVD diamond detector is shown in **Fig. 9** together with an illustration of how the signal rise time is obtained.



**Equation 6** was applied to the four data sets previously analyzed to determine the effective thickness of each of the four CVD diamond detectors. These data are shown in **Fig 10**.

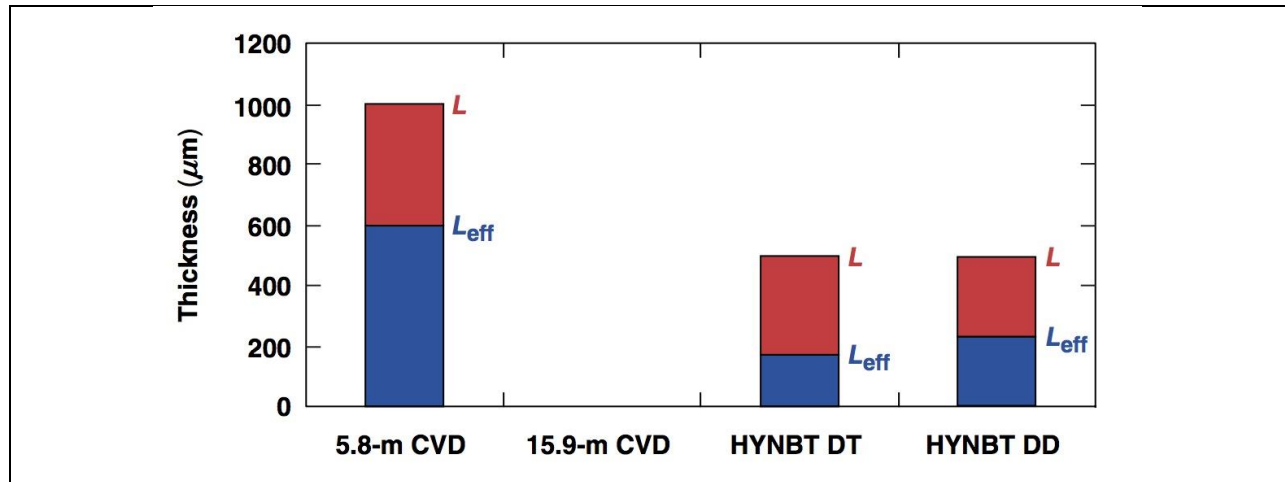


**Figure 10:** Effective thicknesses of three CVD detector configurations. The 5.8 m CVD detector exhibits the greatest charge collection efficiency since the ratio of effective thickness to total thickness is greatest (0.6).

It was not possible to calculate rise-time values of the 15.9-m CVD detector due to low signal amplitude and high noise. As a result, it was not possible to calculate the effective thickness of this detector.

The fact that the effective thickness is a fraction of the total thickness in each case provides an argument for creating thinner layers of diamonds for future detectors. Reducing the distance between electrodes by making thinner CVD layers reduces the probability that charge carriers will recombine within the lattice as they travel towards the electrodes. Recombination is problematic since it reduces the signal and distorts the data. The results shown in **Fig. 10** provide justification for creating a detection system that consists of several thin CVD wafers stacked together with electrodes interspersed between the layers.

## **IX. Conclusion**

This study represents the creation and application of a simple mathematical model to quantify the energy deposition per neutron interaction in CVD diamond detectors. The model is phenomenological and can be applied to datasets obtained from CVD diamond detectors at other facilities as well as OMEGA. The model was applied to four datasets obtained from CVD diamond detectors installed on OMEGA in 2005 and 2015. The results indicate that DD neutrons deposit significantly less energy into these detectors as compared with DT neutrons. Furthermore, the second part of study focused on effective thickness reveals the possibility to use thinner detectors to increase charge collection efficiency.

The next area of interest in the field of neutron detection is the creation of a multi-capacity CVD diamond detector that is capable of detecting lower-energy thermal neutrons. Currently, these neutrons have very low cross sections for reactions with carbon nuclei and thus do not contribute significantly to electron-hole pair generation in CVD diamond alone. Future studies will consider the use of a lithium-fluoride layer stacked above the CVD diamond since the LiF layer is capable of detecting lower-energy neutrons. Stacked CVD diamond detectors are a potentially viable means to further increase signal resolution.

## **X. Acknowledgements**

I would like to thank Dr. Knauer for dedicating countless hours throughout the past year to guide me in exploring this research opportunity. I would also like to thank Dr. Craxton for organizing the high school internship program and providing critical advice in preparing this project and report. Lastly, I would like to thank Dr. Glebov for providing data for the HYNBT campaigns from 2005.

## References

1. Cortesi, Paolo. *Introductory Review of Diamond Detectors*. Institute of Nuclear Physics (2013).
2. V. Glebov. *High-Yield Bang Time Detector for the OMEGA Laser*. *Review of Scientific Instruments* 77, 10E712(2006).
3. S. Almazov, et al. *Thermal and fast neutron detection in chemical vapor deposition single-crystal diamond detectors*. *Journal of Applied Physics* 103, 054501 (2008).
4. G.J. Schmid. *CVD diamond as a high bandwidth neutron detector for inertial confinement fusion diagnostics*. *Review of Scientific Instruments* 74, 1828-1831 (2003).
5. F. Foulon. *Characterization of CVD Diamond Detectors used for Fast Neutron Flux Monitoring*. *Nuclear Instruments and Methods in Physics Research A* 476, 495-499(2002).
6. M. Angleone. *Thermal and fast neutron dosimetry using artificial crystal diamond detectors*. *Radiation Measurements*, 46, 1686-1689(2011).
7. V. Coropceanu, et al. *Charge transport in organic semiconductors*. *Chemical Review*, 107, 926-952 (2007).

***Radiation reaction of electrons at laser intensities up to  $10^{25}$  W/cm<sup>2</sup>***

*Xilin Zhou*

Webster Schroeder High School

Advisor: *Dr. S. X. Hu*

Laboratory for Laser Energetics

University of Rochester

Rochester, New York

November 2015

## Abstract

Recent developments in high-power laser technology allowing for laser intensities from  $10^{22}$  W/cm<sup>2</sup> up to  $10^{24}$  W/cm<sup>2</sup> have opened up the study of the super-intense laser acceleration of electrons to tens of GeV energies. These intensities may be attainable in the next generation of super-powerful lasers such as EP-OPAL, a proposed extension of the Laboratory for Laser Energetics OMEGA EP Laser System which can potentially reach laser intensities as high as  $10^{24}$  W/cm<sup>2</sup>. Previous work on this subject did not account for the radiation reaction force, which is the recoil force caused by the electromagnetic radiation emitted by an accelerating charged particle. In this work, two possible scenarios (an electron originally bound in a highly charged ion, and a counter-propagating 1-GeV electron pulse) were tested. The first scenario, involving the highly charged ion, showed little difference between simulations with and without the radiation reaction force. However, the second scenario, involving the counter-propagating 1-GeV electron pulse, showed the electrons losing significant amounts of energy when the radiation reaction force was accounted for. If harnessed, this radiated energy could be applied in medical and other research fields. Future studies will look into the spectrum and power of the radiated energy.

## I. Introduction

Technological advances over the past two decades have made laser intensities of  $10^{22}$  W/cm<sup>2</sup> obtainable [1]. It may be possible to have laser intensities as high as  $10^{24}$  W/cm<sup>2</sup> in the near future [2]. The laser field strengths at these laser intensities are about three to four orders of magnitude greater than the Coulomb field that binds the ground-state electron in atomic hydrogen. These high laser intensities have opened up the study of the super-intense laser acceleration of electrons. At these super-high intensity levels, electrons accelerated to ultrarelativistic velocities may strongly radiate while their velocity changes. Due to momentum conservation, these electrons experience the radiation reaction (RR) force, which is the force caused by the radiation emitted from the accelerating electron. The radiation released from the electron is directed predominantly along the direction of the particle's motion, within a small range of angles. As a result, the electron trajectory when travelling at relativistic velocities can be significantly changed, leading to changes in the final electron energies as well.

When a free electron is accelerated directly by the laser field, it is expelled from the laser focus region before the laser pulse has reached its maximum intensity. Once expelled, the electron no longer experiences any laser fields. Therefore, even with super-intense lasers, the electrons only acquire a few hundred MeV of energy [3]. The same difficulties are inherent to the alternative method of laser acceleration of electrons initially bound in neutral targets. The electrons are “born” prematurely due to the lower intensities of the increasing laser field, and do not experience the peak intensity of the laser field. This results in final electron energies well below the GeV energies expected from currently available laser intensities [4].

A scenario wherein electrons ionized from highly charged ions interacting with an intense laser field has been proposed as a method for the super-intense laser acceleration of electrons [5,

6]. The ion species are chosen depending on the laser intensity to ensure that the highly charged ions are only ionized when the laser field approaches its peak intensity. The results showed that the ionized electrons are then accelerated by the intense laser field to nearly the speed of light and gain significant amounts of energy while surfing on the laser pulse. However, these previous calculations did not consider how the radiation reaction affects the electron acceleration in such a scenario.

In order to further understand the effects of the radiation reaction force at relativistic velocities, we also consider another scenario in which a 1-GeV electron pulse counter-propagates with respect to the laser pulse. The point of contact between the laser pulse and the electron pulse is at the center of the laser focus. Since the electron pulse and the laser pulse are initially moving towards each other, the electron pulse's deceleration due to the tightly focused laser field is great. Therefore, the radiation reaction force could be significant, which may result in highly modified electron trajectories in such a head-on collision.

In this paper, we analyze the effects of the radiation reaction force on the electron trajectories and final energies for the two scenarios involving the electron originally bound in a highly charged ion, and the counter-propagating electron pulse. We assume the laser pulse is linearly polarized and propagating along the  $z$  axis. Our simulations use lasers expected to become available in the near future. The fields of these lasers can be focused to a small area, thus achieving intensities of up to the order of  $10^{24}$  W/cm<sup>2</sup> in the laser focus region. The relativistic Monte Carlo method is applied to simulate the laser acceleration of electrons in hydrogen-like highly charged ions (HCI), and the interactions between the laser pulse and the counter-propagating electron pulse. For each laser intensity studied, the pulse waist (radius at laser focus) is 10  $\mu$ m. Our principal result is the demonstration that the final energies and ejection angles of

the ionized electron are not greatly affected by the radiation reaction force for the HCI case, whereas the final energies and electron angles for the head-on collision between the electron pulse and the super-intense laser pulse case are significantly altered by the radiation reaction force.

The paper is organized as follows. In **Sec. II**, we outline the classical relativistic Monte Carlo approach used in our simulations as well as the preparation of the ensemble of initial conditions. In **Sec. III**, we present the results of our numerical simulations and explain the major features of our simulation results. Finally, in **Sec. IV**, we summarize our results and present our conclusions.

## **II. Simulation Methods**

### **A. Relativistic classical trajectory Monte Carlo method**

The classical relativistic approach for solving the relativistic Newton's equation of motion is capable of treating the Coulomb potential and the laser-focusing effects three-dimensionally. Although the method cannot simulate the quantum ionization process in the highly charged ion scenario, it can describe the interaction of both an ionized electron and an electron pulse with the laser field with quantitative accuracy.

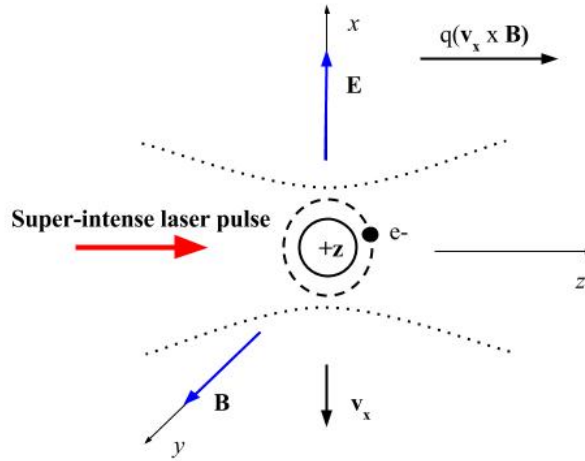


*Figure 1:* Schematic diagram of the interaction of an intense laser pulse with a hydrogen-like, highly charged ion that results in ionization of its electron. The laser pulse propagates along the  $z$  axis while the major electric field  $E$  and the magnetic field  $B$  of the laser pulse are linearly polarized along the  $x$  and  $y$  axes respectively. The vector  $\mathbf{v}_x$  indicates the component of the electron velocity along the  $x$  axis, and  $e^-$  indicates the electron charge. The Lorentz force is represented in the upper right of the figure by  $q(\mathbf{v}_x \times \mathbf{B})$ .

We first consider the interaction of an ultra-intense laser pulse with a hydrogen-like, highly charged ion. *Fig. 1* shows the interaction scheme. The laser pulse is assumed to be linearly polarized along the  $x$  axis and to propagate along the  $z$  axis; it is focused to a small spot having a radius (or beam waist  $w_0$ ) on the order of  $10 \mu\text{m}$ . For such a tightly focused laser beam, the fifth-order expansion of the Maxwell equation has been used to describe the complicated laser field components. As was shown in reference [6], such a description of laser fields is necessary for tight focusing.

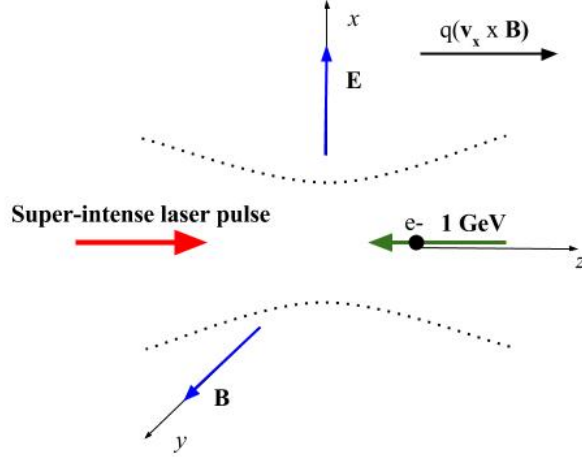


*Figure 2:* Schematic diagram of the interaction of an intense laser pulse with a 1-GeV counter-propagating electron pulse. The directions and indicators of the various vectors are equivalent to those described in *Fig. 1*.

The second scenario we consider is the interaction of an ultra-intense laser pulse with a 1-GeV counter-propagating electron pulse, which is schematically illustrated in *Fig. 2*. The laser pulse is assumed to have the same properties described in *Fig. 1*.

When taking into consideration the RR force, the motion of the ionized electron and the electron pulse in both an electromagnetic field and a Coulomb field is described by

$$\frac{d\mathbf{p}}{dt} = -e \left( \mathbf{E}_L + \mathbf{E}_C + \frac{\mathbf{p} \times \mathbf{B}_L}{m_e \gamma c} \right) + \mathbf{F}_{RR}, \quad (1)$$

where the RR force takes the Landau-Lifshitz [7] format, i.e.,

$$\mathbf{F}_{RR} \approx -\left(\frac{2e^4}{3m_e c^5}\right) \gamma^2 \mathbf{v} \left[ \left( \mathbf{E} + \mathbf{v} \times \frac{\mathbf{B}}{c} \right)^2 - \frac{(\mathbf{E} \cdot \mathbf{v})^2}{c^2} \right], \quad (2)$$

and  $\gamma = \sqrt{1 + \left(\frac{p}{m_e c}\right)^2}$  is the Lorentz relativistic factor;  $c$  is the speed of light in vacuum;  $\mathbf{r}$  and  $\mathbf{p}$  are the coordinate and mechanical momentum vectors of the electron, respectively;  $\mathbf{E}_L$  is the laser electric field; and  $\mathbf{E}_C$  is the Coulomb field of the ion in the HCI case, which is absent in the

electron pulse scenario. The above vector equation can also be written in terms of its three components,

$$\begin{aligned}
dp_x/dt &= -e \left[ E_{L_x} + E_{C_x} + (p_y B_{L_z} - p_z B_{L_y})/(\gamma c) \right] + F_{RR_x}, \\
dp_y/dt &= -e \left[ E_{L_y} + E_{C_y} + (p_z B_{L_x} - p_x B_{L_z})/(\gamma c) \right] + F_{RR_y}, \\
dp_z/dt &= -e \left[ E_{L_z} + E_{C_z} + (p_x B_{L_y} - p_y B_{L_x})/(\gamma c) \right] + F_{RR_z},
\end{aligned} \tag{3}$$

where the three components of the radiation reaction force can be written as,

$$\begin{aligned}
F_{RR_x} &= G(D - M)v_x, \\
F_{RR_y} &= G(D - M)v_y, \\
F_{RR_z} &= G(D - M)v_z,
\end{aligned} \tag{4}$$

where the quantities are  $G = -\left(\frac{2e^4}{3m_e c^7}\right)\gamma^2$ ;  $D = (cE_x + v_y B_z - v_z B_y)^2 + (cE_y + v_x B_z + v_z B_x)^2 + (cE_z + v_x B_y - v_y B_x)^2$ ; and  $M = (E_x v_x + E_y v_y + E_z v_z)$ . The three components of the velocity vector  $\mathbf{v}$  are equal to  $v_x = p_x/m_e \gamma$ ,  $v_y = p_y/m_e \gamma$ ,  $v_z = p_z/m_e \gamma$ .

Using the Runge-Kutta method with variable step size, we numerically integrate *Eqs. (1)* for each classical electron trajectory. For the highly charged ion scenario, the electron trajectories are randomly chosen from a prepared relativistic microcanonical ensemble, which mimics the electronic ground state of the target. The electron ionization time is calculated by the over-the-barrier model [6], in which the electron gets free at the time when the laser field suppresses the Coulomb barrier below the ground-state energy level. For the counter-propagating electron pulse scenario, the initial momentum of the pulse along the  $z$  axis is randomly chosen from a normally distributed set of initial momenta. Our results are presented in **Sec. III** as plots of the normalized count of electrons as a function of the emission angle, and plots of the normalized count of electrons as a function of the electron's final-state energy.

## B. Preparation of electron pulse scenario

In the electron pulse scenario, an initial set of parameters is needed for each trajectory. Therefore, we prepared a normally distributed ensemble of size 200,000 of initial momenta along the  $z$  axis of the electron pulse, and calculated the initial position of the electron pulse along the  $z$  axis. To prepare the previously described ensemble, we first calculate the mean  $p_z$  that the normally distributed ensemble will be centered around. The momentum of a relativistic particle can be described as,

$$p_{z_0} = m_e c \sqrt{\gamma^2 - 1}, \quad (5)$$

where  $\gamma = (E/m_e c^2) + 1$  with  $E = m_e \gamma c^2 - m_e c^2$ . The momentum  $p_{z_0}$  is negative, indicating that the electron is moving towards the negative  $z$  axis (head-on collision with the laser pulse in *Fig. 2*). We then consider the function of the normal distribution to be written as,

$$f(p_z) = \frac{1}{\sigma\sqrt{2\pi}} \exp\left(-\frac{(p_z - p_{z_0})^2}{2\sigma^2}\right), \quad (6)$$

where  $\sigma$  is the standard deviation. We assume a 2% momentum spread [i.e., the full width at half maximum  $FWHM = 2\sqrt{2\ln 2}\sigma$  is 2% of  $p_{z_0}$ ]. With this distribution function, we assign the value of  $p_z$  to each of the total 200,000 electrons. The initial momenta of the electron pulse along the  $x$  and  $y$  axes are assumed to be 0. The electron pulse is initially positioned so that it reaches the center of the laser focus at time  $t = 0$  (at the peak of laser intensity). Since the scenario is modeled with a start time of  $t_0 = -20$  fs, the initial position of the electron pulse along the  $z$  axis can be written as,  $z = p_z \cdot t_0 / m_e \gamma$ . The initial position of the electron pulse along the  $x$  and  $y$  axes is assumed to be 0 in single-trajectory simulations, while for ensemble simulations the electron pulse has the same cross-section as the laser pulse in the  $x$ - $y$  plane.

### III. Results and Discussion

Using the three-dimensional Monte Carlo simulations described in the previous section, we investigated the RR effects of electrons exposed to laser pulses of different intensities. In our simulations, the laser wavelength is equal to  $\lambda=910$  nm, which can be generated by the optical parametric chirp-pulse-amplification (OPCPA) technique [8]. The laser pulse has a Gaussian temporal shape with a full-width at half-maximum (FWHM) of 20 fs and is focused to a beam waist  $w_0=10$   $\mu\text{m}$ .

#### A. Highly charged ions as targets

In this section, we show the simulation results with and without radiation reaction for electrons from highly charged ions interacting with an intense laser beam having various intensities. We find that the final energies and electron angles are only slightly affected by the RR force even at intensities above  $10^{24}$  W/cm<sup>2</sup>. We also present qualitative explanations for the physics behind our results.

The idea of the highly charged ion for laser acceleration of electrons is to allow the electron to remain at the laser focus until the laser pulse reaches the maximum intensity. At that point, the electron is ionized and continues to experience the maximum laser intensity, therefore being accelerated to GeV energies. This requires that the ion target is matched to the maximum laser intensity so that little ionization occurs during the rise time of the laser pulse, but significant ionization through “over-the-barrier” mechanisms occurs at the peak laser intensity. Therefore, in our calculations, we selected charges of the ion target that corresponded with the intensity of the laser pulse. The charges of the ion target at laser intensities  $10^{24}$  and  $10^{25}$  W/cm<sup>2</sup> are  $z = +43.0$  and  $z = +64.0$ , respectively for  $\text{Tc}^{42+}$  ions and  $\text{Gd}^{63+}$  ions.

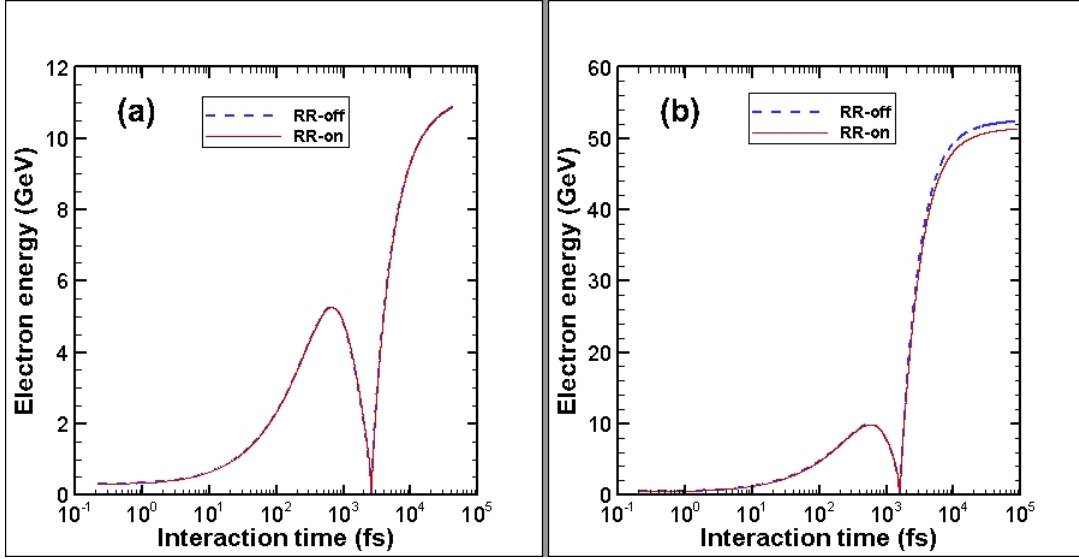


Figure 3: Monte Carlo simulation results for single highly charged ion of (a)  $\text{Tc}^{42+}$  and (b)  $\text{Gd}^{63+}$  interacting with a  $10^{24} \text{ W/cm}^2$  and  $10^{25} \text{ W/cm}^2$  laser, respectively.

We conducted single trajectory simulations with and without the RR effects. The HCI of  $\text{Tc}^{42+}$  and  $\text{Gd}^{63+}$  were initially placed at the center of the laser focus. The kinetic energy of the electron during the trajectory was calculated by  $E = (\gamma - 1)m_e c^2$ . We plot the electron energy as a function of interaction time in Figure 3. The plot shows that there is very little difference in the final electron energies between radiation reaction on and off. Since the electron is highly relativistic and is “surfing” on (co-moving with) the laser wave, the interaction time in the laboratory frame is much longer than the laser pulse duration (20 fs). In the interactions of the  $10^{24} \text{ W/cm}^2$  intensity laser with  $\text{Tc}^{42+}$  ions, the final difference between trajectories with radiation reaction on and off is less than 0.01 GeV. This value is insignificant in comparison with the final electron energies of  $\sim 11$  GeV. At a laser intensity of  $10^{25} \text{ W/cm}^2$ , the final difference between trajectories is approximately 1.3 GeV, which is only  $\sim 2\%$  of the final electron energy of  $\sim 51$  GeV. The final energy for the RR-on case is only slightly lower than that for the RR-off case [see Fig. 3(b)].

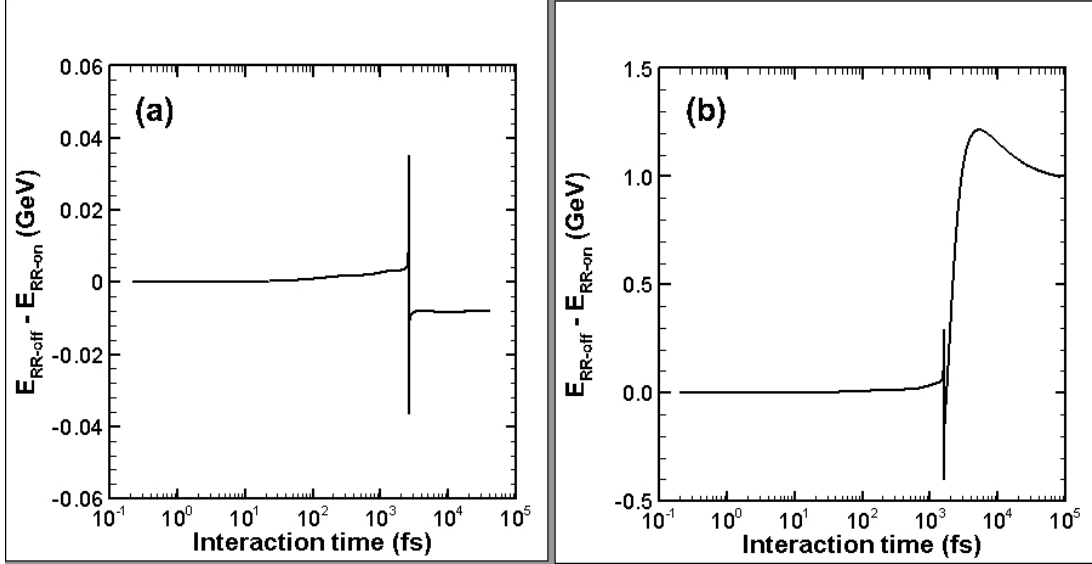
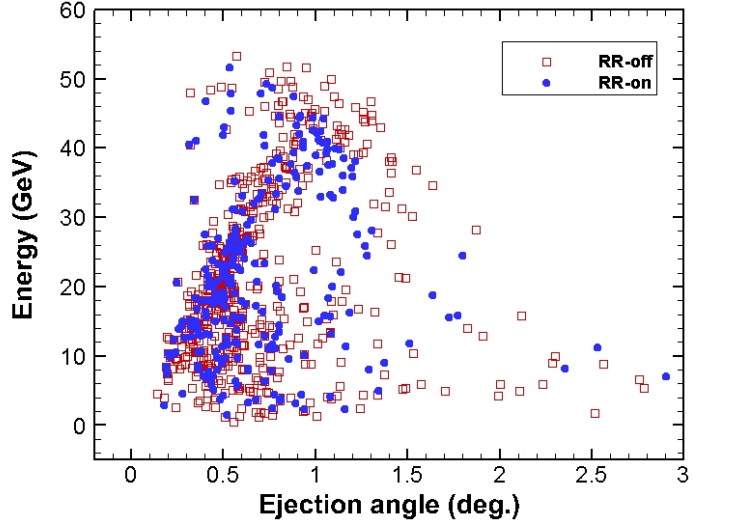


Figure 4: The energy difference in GeV between simulations with and without RR for the cases shown in Fig. 3 plotted as a function of time in fs. (a) The ionized electron is interacting with a  $10^{24}$  W/cm<sup>2</sup> laser pulse. (b) The ionized electron is interacting with a  $10^{25}$  W/cm<sup>2</sup> laser pulse.

To further understand the RR effects of the laser-electron acceleration from HCI, we plot the energy difference in Fig. 4 for the two cases discussed in Fig. 3. We see that the energy difference between RR-on and RR-off remains near zero for the first 1000 fs. Although the initial acceleration after ionization due to the peak-intensity laser field is large, the magnitude of the acceleration is not great enough for any noticeable energy differences due to radiation reaction. However, we see that the radiation reaction effects suddenly show up at  $t \approx 2500$  fs in Fig. 4(a) and  $t \approx 1800$  fs in Fig. 4(b). This is due to the electron being rapidly decelerated and re-accelerated when it is moving from the accelerating phase to the decelerating phase, then back to the accelerating phase. Since the electron's velocity  $v_z$  remains slightly less than the speed of light,  $c$ , phase slippage occurs. This causes a sudden deceleration of the electron when it starts to experience the opposite  $\mathbf{v} \times \mathbf{B}$  and  $E_z$  forces. The abrupt deceleration of the electron will cause it to emit photons so strongly that the RR force can modify the electron dynamics. After the

electron slips back to the acceleration phase again, it is rapidly accelerated to tens of GeV energy in a very short amount of time. Thus, the RR effect shows up during such rapid deceleration and acceleration as seen in *Fig. 4(b)*.



*Figure 5:* Monte Carlo simulation results for highly charged ions interacting with a  $10^{25}$  W/cm<sup>2</sup> intensity laser pulse. The final energies of the ionized electrons are plotted as a function of the ejection angle. The laser parameters are the same as those in *Fig. 3(b)*. The highly charged ions are assumed to be at rest initially and to be distributed randomly within a cylindrical volume (having a radius of 10  $\mu\text{m}$  and a length of 4  $\mu\text{m}$ ) that is oriented along the  $z$  axis and centered about the laser focusing point.

To see the RR effect on macroscopic samples, we conducted simulations for ensembles of electron trajectories at the laser intensity of  $10^{25}$  W/cm<sup>2</sup>. The highly charged ions were randomly given positions on the  $x$ - $y$  plane with a radius of 10  $\mu\text{m}$ , and positions on the  $z$  axis in the range of  $[-2 \mu\text{m}, 2 \mu\text{m}]$  around the focus center at  $z = 0$ . The ensemble simulation results are presented in *Fig. 5*. We define the angle  $\theta = \cos^{-1} \left( \frac{p_z}{|\mathbf{p}|} \right)$  as the electron ejection angle between the electron ejection direction and the laser propagation direction where  $p_z$  and  $\mathbf{p}$  are the  $z$  component and total momentum at the end of the electron trajectory, respectively. The final kinetic energies of the ionized electrons are  $E = (\gamma - 1)m_e c^2$ . *Fig. 5* shows that in order for the

electrons to reach high energies, their ejection angles must be small, since a smaller ejection angle indicates a longer path in the laser focusing area. The electrons are not heavily scattered as a result of the small RR force and therefore the electrons remain highly energized even when RR is turned on. Our results show that despite the large amounts of electron acceleration in the highly charged ion scenario, the RR force (which is dependent on the magnitude of the particle acceleration) is insignificant even at a laser intensity of  $10^{25}$  W/cm<sup>2</sup>. *Figs. 3 and 4* show that the force has little effect on the electron trajectory and consequently allows the electron to remain in the laser focusing area for an extended period of time similar to when RR is off.

### **B. Electron pulse**

The electron pulse scenario shows very different results from the highly charged ion scenario. In this section, we consider the interaction between a laser pulse with the previously provided parameters and a 1-GeV electron pulse counter-propagating with respect to the laser pulse. Our simulations with and without radiation reaction show that the RR force causes the electrons to scatter and lose significant amounts of energy at laser intensities at and below  $10^{23}$  W/cm<sup>2</sup>. At a laser intensity of  $10^{24}$  W/cm<sup>2</sup>, however, large numbers of electrons actually reverse their momentum and are then occasionally re-accelerated by the laser pulse.

We first conducted single-trajectory simulations with and without the radiation reaction force. For single trajectory simulations, the electron was assumed to move along the negative  $z$  axis. The initial position and momentum of the electron were as previously calculated in **Sec. II**. The parameter of  $z_0$  was chosen so that the electron meets the laser peak at the center of focus.

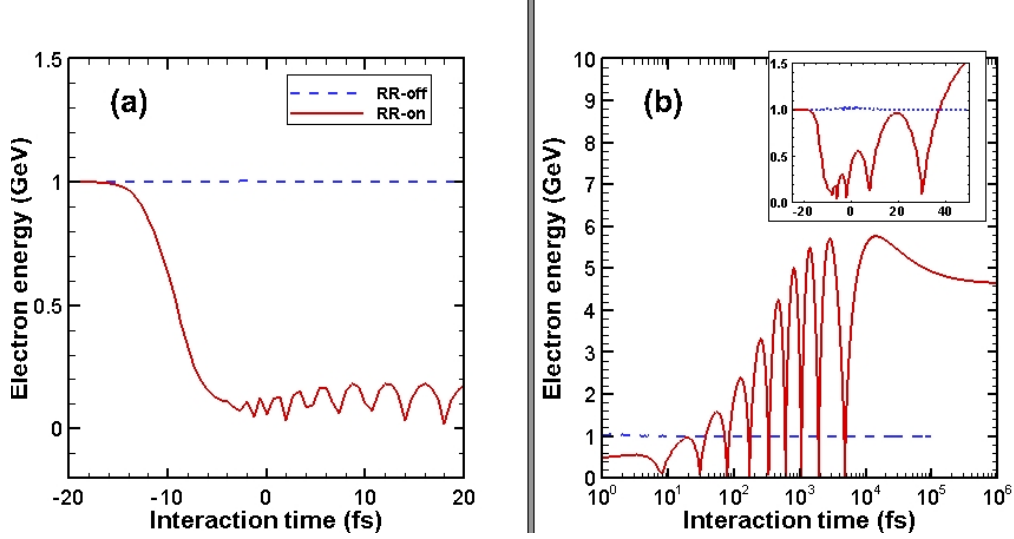


*Figure 6:* Monte Carlo simulation results for a single 1-GeV counter-propagating electron pulse interacting with a super-intense laser. (a) The energy in GeV of the electron pulse interacting with a  $10^{23}$  W/cm<sup>2</sup> laser is plotted as a function of time in fs. (b) The same plot is shown except that the electron pulse is interacting with a  $10^{24}$  W/cm<sup>2</sup> laser pulse. The inset graph shows the electron's energy before and immediately after the peak of the laser pulse. The laser parameters are the same as those in *Fig. 3*.

In *Fig. 6(a)*, the graph shows that when RR is turned off at a laser intensity of  $10^{23}$  W/cm<sup>2</sup>, the electron pulse simply passes through the laser pulse gaining and then losing insignificant amounts of energy, resulting in a final electron energy of 1 GeV. When RR is turned on, the electron experiences severe energy loss as it nears the peak of the laser pulse at time = 0 fs. The laser force acting against the electron results in great deceleration. This deceleration generates large amounts of emitted radiation, causing the electron to lose almost all of its initial energy. Therefore, this scenario effectively converts the electron pulse's kinetic energy into radiation. The oscillation after the energy loss is due to the particle continuing to experience the counter-propagating laser field.

A different result is found when the electron pulse interacts with a laser pulse of intensity  $10^{24}$  W/cm<sup>2</sup>. We see in *Fig. 6(b)* that when RR is off, the electron behaves in the same way as when interacting with a laser pulse of intensity  $10^{23}$  W/cm<sup>2</sup>. When RR is on, the electron first

loses its energy; later on, the electron is accelerated by the laser pulse to GeV energies. As the electron pulse counter-propagates with respect to the laser pulse, two forces act on it: the laser force and the RR force. At a laser intensity of  $10^{24}$  W/cm<sup>2</sup>, the laser force is greater than at  $10^{23}$  W/cm<sup>2</sup>. This greater laser force also causes a greater RR force as seen in Eq. 2. With both forces acting against the momentum of the electron pulse, the electron pulse is turned around by these forces and co-propagates with respect to the original laser pulse. The electron pulse is thus re-accelerated by the laser pulse and gains significant amounts of energy before exiting the laser focus region.

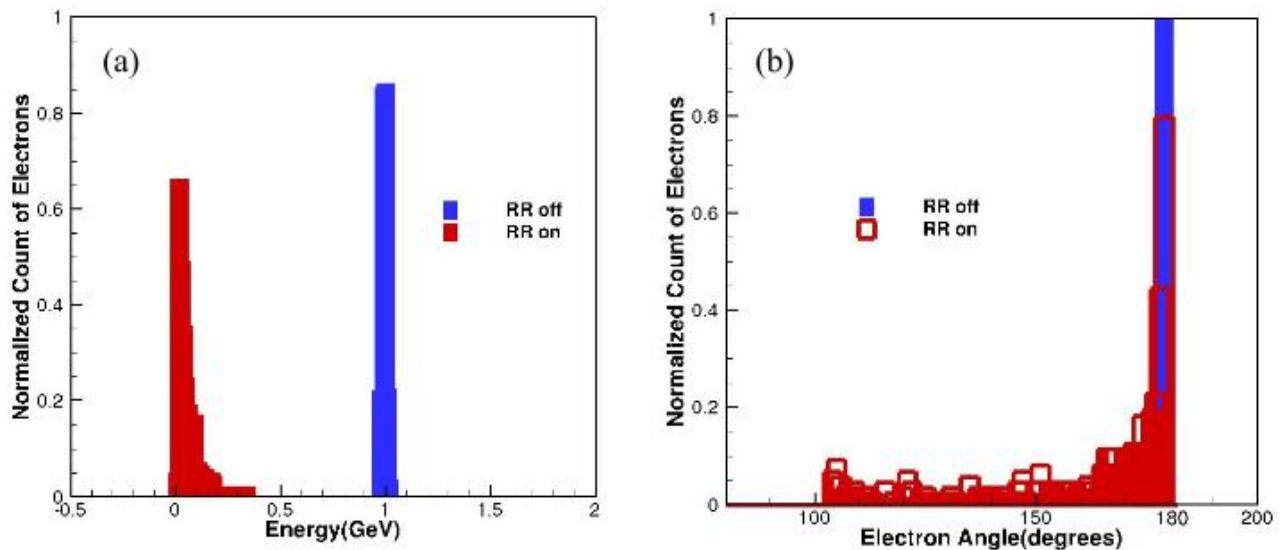


Figure 7: Monte Carlo simulation results for 1-GeV counter-propagating electron pulses interacting with a  $10^{23}$  W/cm<sup>2</sup> intensity laser pulse. (a) The normalized distribution of final electron energies, which shows that with RR, all electrons exit the focusing area with less than 0.5 GeV of energy. (b) The normalized distribution of final electron angles (relative to the  $z$  axis), which shows that with RR, most electrons are scattered by the laser pulse. The laser parameters are the same as those in Fig. 3. The electrons are distributed randomly within a cylindrical volume (having a radius of  $10 \mu\text{m}$  and a length of  $4 \mu\text{m}$ ) that is oriented along the  $z$  axis.

Finally, we conducted simulations for ensembles of electron trajectories at the laser intensities  $10^{23}$  and  $10^{24}$  W/cm<sup>2</sup>. The electron pulses were randomly given positions on the  $x$  and  $y$  axes within a radius of 10  $\mu\text{m}$ , and positions on the  $z$  axis in the range of  $[z_0 - 2 \mu\text{m}, z_0 + 2 \mu\text{m}]$  from the originally calculated position  $z_0$ . The momentum of each electron in the electron pulse was randomly chosen from a normally distributed sample previously explained in **Sec. II**. We present the sample simulation results as bar graphs in *Fig. 7* for the case of  $10^{23}$  W/cm<sup>2</sup>. The plot supports our results from the single trajectory simulations at  $10^{23}$  W/cm<sup>2</sup>. Without RR, the blue bars in *Fig. 7* show that the final electron energy equals the initial 1 GeV energy, and the electrons still propagate towards the negative  $z$  axis ( $\theta=180^\circ$  relative to the laser propagation direction). These results show that the electron pulses leave the laser focus region virtually unaffected by the laser pulse. When RR is turned on, the red bars in *Fig. 7* show that the electrons lose more than half of their initial energy and that they are scattered. The wide range of electron angles in *Fig. 7(b)* is caused by the RR force which, when strong enough, pushes the electrons out of the laser focusing region. A significant number of electron trajectories with RR result in a final electron angle of  $180^\circ$ , which means that the electrons were not scattered in that situation. This is likely due to the variation in the initial momentum and the transverse placement of electrons.

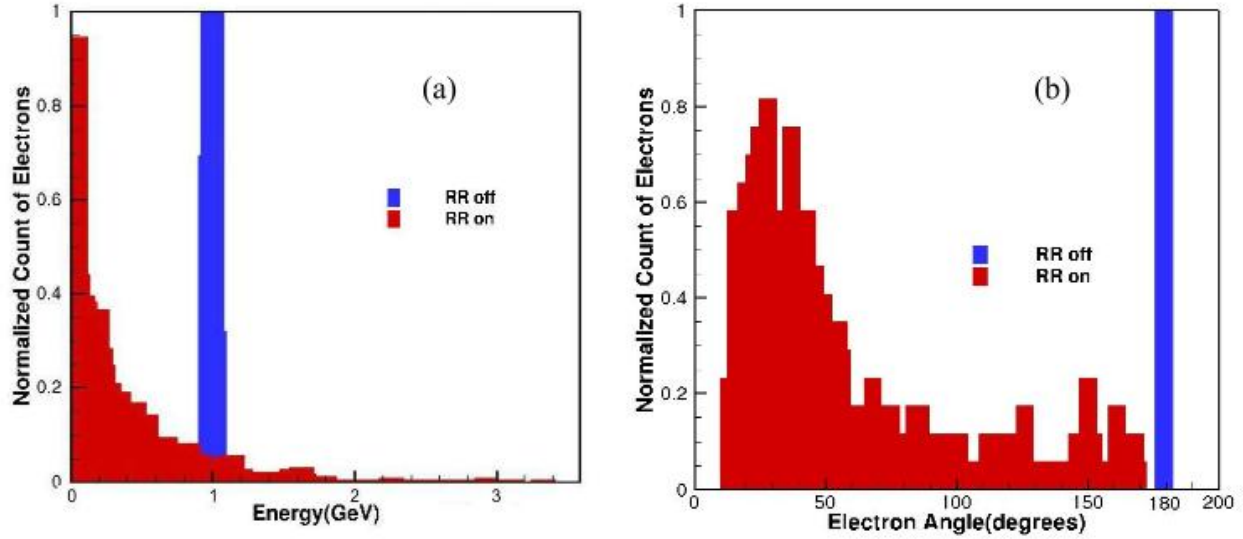


Figure 8: Monte Carlo simulation results for 1-GeV counter-propagating electron pulses interacting with a  $10^{24}$  W/cm<sup>2</sup> intensity laser pulse. (a) The normalized distribution of final electron energies. (b) The normalized distribution of final electron angles, which shows that most electrons are scattered by the laser pulse. The laser parameters are the same as those in Fig. 3. The electron pulses are distributed in the same way as described in Fig. 7.

In contrast to the electron pulse interactions shown in Fig. 7, Fig. 8 depicts that at a laser intensity of  $10^{24}$  W/cm<sup>2</sup>, the majority of electrons have final electron angles less than  $90^\circ$  [see Fig. 8(b)]. This shows that the electrons are being turned around by the laser field and radiation reaction force. The electrons now either lose most of their energy after being scattered in the positive or negative  $z$  direction, or gain back energy from the laser field while being re-accelerated, similar to the results graphed in Fig. 6(b). This energy gain can be quite significant with final energies occasionally over 3 GeV. Most of the electrons turned around for acceleration never reach high energies, however, and leave the focus region at around  $\sim 50$  degrees in the positive  $z$  direction.

Our results show that the RR effect causes the electron pulse to release large amounts of radiation. Without RR on, the electron pulse simply passes through the laser pulse with little effects. When RR is on, however, the electron trajectories are significantly altered. At a laser

intensity of  $10^{23}$  W/cm<sup>2</sup>, the electrons scatter due to the laser pulse and lose more than half of their initial energy to emitted radiation. When we increase the laser intensity to  $10^{24}$  W/cm<sup>2</sup>, some of the electrons continue to behave as seen when interacting with  $10^{23}$  W/cm<sup>2</sup> lasers. However, most of the electrons are turned around by the combination of the laser force and the RR force to co-propagate with the laser pulse. While most electrons are scattered out of the focus region before getting accelerated to high energies, some of the co-propagating electron pulses go on to be re-accelerated by the laser pulse to GeV energies. The electron pulse scenario would be an effective method for generating radiation and if harnessed, this radiation could potentially be applied in other fields of research.

#### **IV. Summary and Conclusions**

In this paper, the relativistic classical trajectory Monte Carlo method has been used to simulate the interactions of electrons ionized from highly charged ions and electron pulses with ultra-intense laser pulses. In the highly charged ion scenario, we simulated the acceleration of electrons ionized from hydrogen-like highly charged ions interacting with an intense, tightly focused laser field. We also considered the interaction of a 1-GeV electron pulse counter-propagating with respect to the super-intense laser pulse. In the highly charged ion scenario, it is found that the radiation reaction force does not have a great effect on the electron trajectories after ionization even at a laser intensity of  $10^{25}$  W/cm<sup>2</sup>. For the case of laser pulse “collisions” with electron pulses, the radiation reaction force significantly alters the electron trajectories. At a laser intensity of  $10^{23}$  W/cm<sup>2</sup>, the electrons lose significant amounts of energy and are scattered as a result of the radiation reaction force. When the intensity is increased to  $10^{24}$  W/cm<sup>2</sup>, the electrons are either scattered or turned around to co-propagate with the laser pulse. Most

electrons that are turned around are scattered out of the focus region before reaching high energies, while a few electrons are re-accelerated by the laser pulse to GeV energies.

## Acknowledgements

This project owes much thanks to Dr. Hu who was always ready to give feedback and support no matter how small or large the difficulty. I would also like to thank Dr. Craxton for his suggestions and for the opportunity to be a part of this program, and Dr. Enck for his unwavering encouragement the past few years. Finally, I thank the Laboratory for Laser Energetics for providing resources and granting an invaluable research experience.

## References

- [1] V. Yanovsky, V. Chvykov, G. Kalinchenko, P. Rousseau, T. Planchon, T. Matsuoka, A. Maksimchuk, J. Nees, G. Cheriaux, G. Mourou, and K. Krushelnick, *Opt. Express* **16**, 2109 (2008)
- [2] T. Tajima and G. Mourou, *Phys. Rev. ST Accel. Beams* **5**, 031301 (2002)
- [3] F. V. Hartemann, S. N. Fochs, G. P. Le Sage, N. C. Luhmann, Jr., J. G. Woodworth, M. D. Perry, and Y. J. Chen, and A. K. Kerman, *Phys. Rev. E* **60**, 7473 (1999)
- [4] C. H. Keitel, *J. Phys. B* **29**, L873 (1996)
- [5] S. X. Hu, and A. F. Starace, *Phys. Rev. Lett.* **88**, 245003 (2002)
- [6] S. X. Hu, and A. F. Starace, *Phys. Rev. E* **73**, 066502 (2006)
- [7] L. D. Landau and E. M. Lifshitz, in *The Classical Theory of Fields*, 3rd Ed. (Pergamon Press, Oxford, 1971), Vol. 2, Chap. 7, p. 208.
- [8] I. N. Ross, J. L. Collier, P. Matousek, C. N. Danson, D. Neely, R. M. Allott, D. A. Pepler, C. Hernandez-Gomez, and K. Osvay, *Appl. Opt.* **39**, 2422-2427 (2000)